Università degli Studi di Ferrara

DOTTORATO DI RICERCA IN
SCIENZA DELL'INGEGNERIA

CICLO XXX

COORDINATORE Prof. Stefano Trillo

de Saint Venant-Exner morphological models: computational methods for long-term numerical modelling

Settore Scientifico Disciplinare ICAR/01

Dottorando:
Dott. Francesco Carraro

Tutori:
Prof. Alessandro Valiani

Dr. Valerio Caleffi

Anni 2014/2017

A Chiara
e alla sua mamma, Jessica.

ABSTRACT

Morphodynamic models are used to predict river and nearshore evolution describing the interactions between sediments and water flow. Due to the importance of many engineering applications requiring morphodynamic predictions, great attention has been devoted to the development of more efficient numerical techniques.

Morphodynamics combines two processes: the faster hydrodynamic evolution and the slower sediment-dynamics. When the sediment transport is much slower than the hydrodynamic evolution (i.e. the Froude number of the water flow is far from the unity), the interaction between water flow and bed response is very weak. From an analytical study of the one-dimensional, non-conservative, de Saint Venant-Exner (dSVE) system of equations result that, under this condition, the morphodynamic evolution depends almost on the central wave of the associated Riemann problem. According to this theoretical study, this doctoral dissertation is focused on the increasing of the numerical efficiency of morphological models.

First a new efficient implementation of the Dumbser-Osher-Toro (DOT) scheme for non-conservative problems is presented. The DOT path-conservative scheme is a robust upwind method based on a complete Riemann solver, but with the drawback of requiring expensive numerical computations. Indeed, to compute the non-linear time evolution in each time step, the DOT scheme requires numerical computation of the flux matrix eigenstructure (the totality of eigenvalues and eigenvectors) several times at each cell edge. In this research, an analytical and compact formulation of the eigenstructure for the dSVE model is introduced and tested in terms of numerical efficiency and stability.

Second a general mathematical framework is built to study the acceleration of morphodynamic simulations. Thus, a non-uniform acceleration is applied to the one-dimensional dSVE model by multiplying all the spatial derivatives by an individual constant (≥ 1) acceleration factor. In this framework, one of the most applied morphological acceleration techniques, the MORFAC approach, can be seen as a particular case of the non-uniform acceleration. According to the MORFAC approach only the sediment mass continuity equation is accelerated. The final goal of the non-uniform acceleration is to identify the best combination of the three accelerating factors. Such a combination must respect two points: i) the bed responds linearly to hydrodynamic changes; ii) a consistent decrease of the computational cost is

obtained. An analytical investigation of the non-uniform accelerated problem allows derivation of a new linear morphodynamic acceleration technique, MASSPEED (MASs equations SPEEDup), in which both mass conservation equations (water and sediment) are accelerated by the same factor. Moreover, the new framework allows an *a priori* determination of the highest possible acceleration for both MORFAC and MASSPEED techniques. Finally, MORFAC and MASSPEED are implemented in the A-DOT numerical scheme and numerical simulations of a long-term sediment hump propagation demonstrate the advantages of the new approach.

Acknowledgements

I would like to thank my supervisors, Prof. Alessandro Valiani and Dr. Valerio Caleffi, who gave me the opportunity of attending the PhD school of Engineering Science of the University of Ferrara. Thank you for your interest and encouragement from the beginning, for your interesting discussions and guidance through the road to finish this thesis.

Thanks to Dr. Annunziato Siviglia and Dr. Davide Vanzo who welcomed me in Zurich. I really appreciate your time, the challenging questions and interesting discussions. Last but not least, thanks for your academic and also moral support during the recent RCEM conference and the writing of the paper on the MASSPEED approach.

Thanks to the University of Ferrara that supported me within the "Young Researchers Project" during my visit to the Laboratory of Hydrology, Hydraulics and Glaciology of the Swiss Federal Institute of Technology.

A special acknowledgement goes to all my colleagues in Ferrara and Zurich. You guys made me feel at home during all the last three years.

Finally, I am very much indebted to my family. Thanks to Jessica, who supported me in every possible way to see the completion of this work. Thanks to my parents for their love and encouragement in all my pursuits. And thanks to my brother Thomas, whose advice and support helped me to persevere in the difficult moments.

Contents

List of Figures

List of Tables

Chapter 1

Introduction

Morphodynamic models are used to predict river evolution describing the interactions between sediments and water flow. Due to the importance of many engineering applications requiring morphodynamic predictions, great attention has been devoted to the development of more efficient numerical techniques.

It is worth noting that the physics of sediment transport is very sophisticated, specially in non-equilibrium conditions. In general, in non-equilibrium condition, sediment transport capacity and actual sediment transport are different quantities due to the general unsteadiness of the flow in time and to non-uniformity of the flow field in space. In unsteady flow, the sediment transport has a time/length adaptation in time/space that depends on the characteristics of the flow field and on the characteristics of the sediments. Bedload has typically short adaptation time/length, while suspended sediment transport has a longer adaptation time/length, especially for small grain diameter. Moreover, because a multiplicity of adaptation times/lengths exist, the non-uniformity in grain size of the transported granular material makes the problem even more complicated and more rich by introducing the interaction between different sediment sizes (hiding factors, armoring effects, ...) [2, 36, 50].

However, the greater the considered physical complexities are, the greater becomes the number of empirical coefficients needed for a mathematical description of morphological processes. In the perspective of a general, conceptual study, a great number of coefficients is not very significant. Obviously, if one is interested in describing ripples or dune dynamics or rapidly varying sediment transport transients, the proper mechanical formulation of the sediment movement must be chosen.

With the aim of studying numerical efficiency in long term morphodynamic simulations, in this doctoral dissertation the sediment dynamics is studied according to a very simple, Exner based [27], sediment transport approach. Therefore, to keep as general as possible this theoretical study, the de Saint Venant equations (also called shallow water equations, SWE) coupled with the Exner sediment continuity

equation are considered.

Many mathematical models [e.g. 5, 6, 22, 34, 40, 56, 66] for the study of natural river, estuarine and nearshore morphodynamics are based on the de Saint Venant - Exner (dSVE) system of equations. This set of balance laws has the main disadvantage of containing a non-conservative product due to the variable bottom topography in the momentum balance [48].

From the conceptual point of view, morphodynamics combines two processes: the faster hydrodynamic evolution and the slower sediment-dynamics. When the Froude number is small, these two processes are characterized by very different time scales and the interaction between them becomes very weak. Therefore, most morphodynamic models for practical applications were developed by splitting the computation of the hydrodynamics from the bed topography adaptation [e.g. 5, 22, 34, 40, 66]. These models separately solve the SWE for a fixed topography, later updating such topography by using the Exner equation with the updated hydrodynamic quantities. In this manner the hydrodynamic part of the governing system can be treated as a strictly hyperbolic system of equations, thus avoiding the complexities typical of non-conservative balance laws.

The hypothesis of very weak interactions between water flow and bed response allowed also the introduction of recent morphodynamic upscaling techniques, which becomes essential when long-term evolutions must be predicted [e.g. 17, 53, 55]. Among them, the MORFAC (MORphological acceleration FACtor) approach [34, 52] is now standard in state-of-the-art professional morphological codes [51]. The key idea of the MORFAC approach is to accelerate the morphological evolution increasing the time bottom variations by a given constant (> 1) factor, thus accelerating the morphodynamic processes. This is effectively obtained by multiplying the sediment flux in the Exner equation by a constant acceleration factor updating the bed and flow within the same time step. According to Ranasinghe *et al.* [51] this approach can be adopted only if the morphological response to the hydrodynamic forcing is linear during one morphological time step. In this context, the hypothesis of weakly coupling between hydro- and morpho-dynamic is a necessary (but not sufficient) condition for a linear morphological speedup [14].

In spite of the wide application of the decoupled approach, the importance of integrating the whole system of PDE in a coupled manner has been highlighted in the recent years [6, 18], both to better represent the physical phenomenon in the case of intense sediment transport and to avoid numerical instabilities. It is important to note that rapidly-varying hydraulic conditions, like sudden hydraulic transients and steady or unsteady breaking waves, are the typical conditions requiring a coupled approach. For example, studying the morphodynamics of the nearshore zone, Kelly & Dodd [31] show that the use of a decoupled approach in presence of bore-driven sediment transport leads to the overestimation of the net offshore transport in the swash zone. Postacchini *et al.* [49] show that the erosion of the bed is significantly

larger in the uncoupled models if a swash forced by a dam-break is considered.

Moreover, Cordier *et al.* [18] showed that decoupling hydrodynamics and morphodynamics could generate some non-physical oscillations related to the hyperbolicity of the system of equations. These oscillations occur even when a robust and well-balanced numerical scheme for the de Saint Venant system is used, especially when the bed evolution is very dynamic [18]. In some cases, such oscillations can be avoided by reducing the Courant–Friedrichs–Lewy coefficient [61], but decreasing the numerical efficiency by forcing a smaller time step in time-integration.

However, the fully coupled approach also presents a critical issue. The non-conservative form of the de Saint Venant-Exner (dSVE) system prevents formulation of the classic Rankine-Hugoniot relationship, leading to uncertainties about the mathematical representation of the hydraulic jumps. See [1] for an analysis of this issue.

A theoretical contribution to the solution of this problem comes from the Dal Maso, LeFloch, and Murat (DLM) theory [19] which introduces the generalized Rankine-Hugoniot relationship for a given arbitrary integration path. The DLM theory does not give information about the selection of the path, leaving some degrees of freedom. This freedom was used by Parés [48] to introduce the family of path-conservative (or path-consistent) methods to properly handle non-conservative system of equations.

Formally consistent numerical solutions can be obtained by coupling the path-conservative schemes with appropriate paths. Furthermore, by selecting the path on the basis of physical considerations, a target specific behaviour of the resulting numerical models can be achieved. For example, to develop a well-balanced scheme with respect to the case of still water with a constant free surface elevation, simple segment paths are sufficient [15]. Otherwise, to obtain energy-balanced scheme that exactly reproduce the constancy of the total head in the case of steady flows over short distance[45], more elaborated paths must be introduced [7, 8, 28, 63].

In the last ten years, different methods have been based on the path-conservative schemes [9, 16, 25]. In particular, a very general and robust method is the Dumbser-Osher-Toro (DOT) Riemann solver [25]. It is an upwind scheme based on a complete Osher-type Riemann solver that performs well with various non-conservative problems (e.g. [8, 23, 43]). Nevertheless, DOT has the drawback of requiring several numerical computations of the full eigenstructure (the totality of eigenvalues and eigenvectors) of the flux matrix per time step. Thus the method has remained unattractive to parts of the computational community due to its high computational cost, which makes the method more suited for basic numerical tests than for practical engineering applications.

The high computational cost of coupled methods and large uncertainties in real world monitoring allowed in the past a wide empirical approach in calibration of morphological models. Empirical approach can be useful for the reproduction of

very complicated and bounded problems, but it is not a suitable approach for long term prediction. When the total duration of the simulation is longer than 5-10 times the monitoring time, a physical approach and a well-posed numerical model must be chosen. Thus, once a mechanical-mathematical model is assumed to be valid (possibly minimizing parameters tuning), it must be accurately integrated with strictly-dedicated numerical methods. Furthermore, the relative computational error should be order of magnitude smaller than the expected errors intrinsic in the hypothesis of the chosen mathematical model. Due to the peculiarity of the weakly coupled morphodynamic evolution, a deep understanding of which mathematical components contribute to the riverbed evolution is crucial to choose the most appropriate approach to each particular hydrodynamic condition.

This doctoral dissertation is structured as follow. In Chapter 2 the 1D de Saint Venant-Exner mathematical model is briefly summarized. Then a compact and easy to implement analytical formulation of dSVE eigenstructure is introduced and a theoretical characteristic approach is used to study quantitatively the weak coupling between water flow and bed adaptation. The theoretical framework introduced in Chapter 2 is applied to improve the computational efficiency of morphodynamic models with two different strategies, in Chapters 3 and 4 respectively. In Chapter 3 the analytical formulation of the dSVE eigenstructure is implemented into the DOT solver to avoid complex numerical tools to compute eigenvalues, eigenvectors and inverse matrices, improving both the numerical efficiency and the model coding. Thus, a study of the numerical efficiency and a strong validation of the analytical implementation (A-DOT) is presented, using as references original DOT and PRICE-C [9, 56] schemes and two different experimental data sets. The results presented in Chapter 3 originate in [12] which was a preliminary work of [13] (at the moment submitted to Advances in Water Resources). In Chapter 4 the theoretical analysis performed in Chapter 2 is generalized to build a mathematical framework to study general morphological acceleration techniques. Thus, the MORFAC, which is a particular case of the new general framework, is compared to MASSPEED (MASs equations SPEEDup), a new morphological acceleration technique. MASSPEED have been recently presented to RCEM2017, while the original paper [14] is still under review. Finally, in Chapter 5 conclusions are drown.

Chapter 2

Mathematical Model

2.1 Governing equations

In the present research, the morphodynamic problem of a wide rectangular cross-section is described by the classical unit-width de Saint Venant equations coupled with the Exner equation. When the total sediment transport is supposed to match the sediment transport capacity of the flow, the resulting dSVE model can be written as

$$\begin{cases} \dfrac{\partial h}{\partial t} + \dfrac{\partial q}{\partial x} = 0 & \text{(2.1a)} \\ \dfrac{\partial q}{\partial t} + \dfrac{\partial}{\partial x}\left(\dfrac{1}{2}gh^2 + \dfrac{q^2}{h}\right) + gh\,\dfrac{\partial z}{\partial x} = -gh\,s_f & \text{(2.1b)} \\ \dfrac{\partial z}{\partial t} + \xi\dfrac{\partial q_s}{\partial x} = 0 & \text{(2.1c)} \end{cases}$$

with $h(x,t)$ the water depth; $q(x,t)$ the specific water discharge; $z(x,t)$ the bed elevation; g the gravitational acceleration; s_f is the friction slope; q_s the sediment transport specific discharge (in volume); $\xi = 1/(1-p)$ where p is the porosity of the riverbed. In this work p is assumed constant, and thus also ξ is constant.

It is well known that the de Saint Venant-Exner model contains a non-conservative product, that is the bed topography term in the momentum equation (2.1b). Therefore, to properly include the non-conservative product [19], system (2.1) must be written in a quasi-linear form as

$$\frac{\partial \boldsymbol{W}}{\partial t} + \boldsymbol{\mathcal{A}}(\boldsymbol{W})\frac{\partial \boldsymbol{W}}{\partial x} = \boldsymbol{S}(\boldsymbol{W})\,, \tag{2.2}$$

in which $\boldsymbol{W}$ is the vector of the conservative variables, $\boldsymbol{\mathcal{A}}(\boldsymbol{W})$ is the flux matrix and

$\boldsymbol{S}(\boldsymbol{W})$ is the vector of the source terms

$$\boldsymbol{W} = \begin{bmatrix} h \\ q \\ z \end{bmatrix}, \quad \boldsymbol{\mathcal{A}}(\boldsymbol{W}) = \begin{bmatrix} 0 & 1 & 0 \\ c^2 - u^2 & 2u & c^2 \\ \xi \frac{\partial q_s}{\partial h} & \xi \frac{\partial q_s}{\partial q} & 0 \end{bmatrix}, \quad \boldsymbol{S}(\boldsymbol{W}) = \begin{bmatrix} 0 \\ -c^2 s_f \\ 0 \end{bmatrix}, \tag{2.3}$$

with $u = q/h$ the depth averaged velocity and $c = \sqrt{gh}$ the propagation celerity of gravitational waves.

System (2.1) is composed by three partial differential equations in five unknowns: $h(x,t)$, $q(x,t)$, $z(x,t)$, $s_f(x,t)$ and $q_s(x,t)$. Therefore, other two relations are required to close the system. The friction term is provided by a classical closure, namely

$$s_f = \frac{q^2}{{K_s}^2 \, h^{10/3}}, \tag{2.4}$$

where K_s is the Strickler coefficient. For the sake of simplicity, the Grass closure formula [29] could be chosen for the computation of bed load discharge:

$$q_s = A_g \, u^3, \tag{2.5}$$

where A_g is a constant that depends on the grain properties of the bed.

However, all the discussion in this doctoral dissertation is not related to a specific closure for the evaluation of q_s. As soon as the hyperbolicity of system (2.1) is verified (see [18] for the conditions that must be respected), the results described in this work remain valid for any expressions of the sediment discharge, which allows the evaluation of q_s derivatives. In particular, in §3.4.2 three other formulation of q_s are considered to compare numerical solution and experimental data:

1. a simple power-law similar to the Grass formula, but with threshold on the incipient transport velocity:

$$q_s = A_g \, (u - u_{cr})^3; \tag{2.6}$$

2. the Meyer-Peter & Müller (MPM) formula [41],

$$q_s = \Phi(\theta) \times \sqrt{g \, (S_g - 1) \, {d_{50}}^3} \tag{2.7}$$

with

$$\Phi(\theta) = \begin{cases} 8(\theta - 0.047)^{3/2} & \text{if } \theta > 0.047 \\ 0 & \text{otherwise} \end{cases}, \tag{2.8}$$

where $S_g = 2.6$ is the relative density of the sediment grain, d_{50} is the median sediment diameter and θ is the Shields stress given by

$$\theta = \frac{s_f \, h}{(S_g - 1) \, d_{50}}; \tag{2.9}$$

3. the Van Rijn formula [65],

$$q_s = 0.053 \frac{\mathtt{T}^{2.1}}{\mathtt{D}_*^{0.3}} \times \sqrt{g\ (S_g - 1)\ {d_{50}}^3}, \tag{2.10}$$

with

$$\mathtt{T} = \frac{{u_*}^2 - {u_{*cr}}^2}{u_{*cr}^2} \quad \text{and} \quad \mathtt{D}_* = d_{50} \left[\frac{g(S_g - 1)}{\nu} \right]^{1/3}, \tag{2.11}$$

where $\nu = 10^{-6}$ m^2/s is the kinematic viscosity, $u_* = \sqrt{g\, h\, s_f}$ is the shear stress velocity and u_{*cr} is the critical shear stress velocity given by:

$$u_{*cr} = \theta_{cr} \sqrt{g(S_g - 1) d_{50}} \qquad \text{with} \qquad \theta_{cr} = 0.03\ . \tag{2.12}$$

2.2 Eigenvalues and characteristic curves

The characteristic polynomial of the system matrix, defined in (2.3), is obtained as usual, with the imposition that $|\boldsymbol{\mathcal{A}}(\boldsymbol{W}) - \lambda \boldsymbol{I}| = 0$. When this polynomial is divided by c^3 to obtain a non-dimensional formulation, it becomes

$$\frac{\lambda^3}{c^3} - 2\,\mathtt{Fr}\,\frac{\lambda^2}{c^2} - \left(1 - \mathtt{Fr}^2 + \xi \frac{\partial q_s}{\partial q}\right) \frac{\lambda}{c} - \xi \frac{\partial q_s}{\partial h} \frac{1}{c} = 0. \tag{2.13}$$

According to the method proposed by Cardano [11], in the form applied in [64], the three solutions of Eq. (2.13), i.e. the three non-dimensional eigenvalues, can be analytically expressed as:

$$\frac{\lambda_1}{c} = \frac{2}{3}\,\mathtt{Fr} - \frac{2}{3}\sqrt{k_1}\,\cos\left(\frac{\phi}{3} - \frac{\pi}{3}\right), \tag{2.14a}$$

$$\frac{\lambda_2}{c} = \frac{2}{3}\,\mathtt{Fr} + \frac{2}{3}\sqrt{k_1}\,\cos\left(\frac{\phi}{3}\right); \tag{2.14b}$$

$$\frac{\lambda_3}{c} = \frac{2}{3}\,\mathtt{Fr} - \frac{2}{3}\sqrt{k_1}\,\cos\left(\frac{\phi}{3} + \frac{\pi}{3}\right), \tag{2.14c}$$

where the parameters ϕ and k_1 are:

$$\phi = \arccos\left(\frac{k_2}{\sqrt{4{k_1}^3}}\right); \tag{2.15}$$

$$k_1 = 3 + \mathtt{Fr}^2 + 3\,\xi \frac{\partial q_s}{\partial q}; \tag{2.16}$$

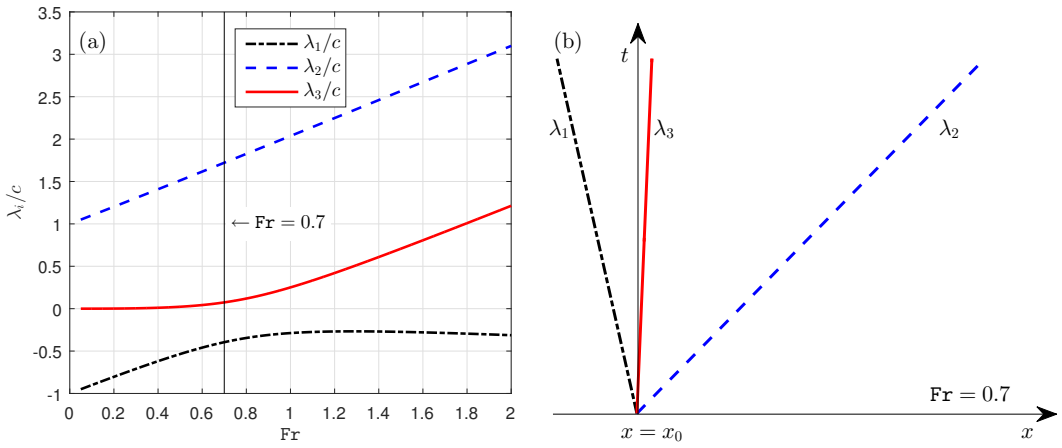

Figure 2.1: Analytical eigenvalues of the dSVE mathematical model (2.1). In panel a) non dimensional analytical eigenvalues (2.14) are drown with the derivatives of q_s computed according to Eq. (2.5) by setting $A_g = 0.005$ s^2/m. Panel b) shows a sketch of (linearized) characteristic curves in the phase space for the typical situation for subcritical conditions ($u > 0$, $\mathtt{Fr} = 0.7$).

with k_2 given by:

$$k_2 = -2\mathtt{Fr}^3 + 18\mathtt{Fr}\left(1 + \xi\frac{\partial q_s}{\partial q}\right) + 27\,\xi\frac{\partial q_s}{\partial h}\frac{1}{c}\,. \tag{2.17}$$

In Figure 2.1, the analytical eigenvalues of Eqs. (2.14) are shown for $0 < \mathtt{Fr} < 2$, the derivatives of q_s being computed according to Eq. (2.5) with $A_g = 0.005$ s^2/m. If a power law formula for the solid transport is used, as that adopted in Eq. (2.5), the three eigenvalues $\lambda_1, \lambda_2, \lambda_3$, the solutions of the cubic polynomial (2.13), are always real, therefore the governing system is always hyperbolic [18]. For more general sediment transport formulas, where the non dimensional solid discharge is expressed as a function of the dimensionless Shields parameter (e.g. Eq. (2.7) by Meyer-Peter & Müller [41]), if the friction term is closed using a Manning approach, the governing system is hyperbolic provided that $\mathtt{Fr} < 6$ [18]. This latter condition is usually satisfied under *natural* conditions.

On the $(x - t)$ plane (phase space) the eigenvalues are celerities associated to characteristic curves along which small disturbances propagate. Herein, the term celerity is applied broadly to mean the velocity of propagation of a disturbance, either on the water surface or on the bed. For very small disturbances the characteristic curves can be approximated by straight lines. The situation for a small disturbance generated at time $t = 0$ in x_0, in case of subcritical flow ($\mathtt{Fr} < 1$) is given in Figure 2.1b.

Once the eigenvalues are determined, the associated right eigenvectors $\mathbf{r}_i$ (as columns) can be obtained directly from their definition (up to a constant), i.e.,

$$\boldsymbol{\mathcal{A}}\,\mathbf{r}_i = \lambda_i\,\mathbf{r}_i. \tag{2.18}$$

By imposing the first component $\mathbf{r}_i^{(1)} = 1$, there is a degree of freedom in solution of the linear system (2.18). Therefore, $\mathbf{r}_i^{(2,3)}$ can be computed by solving a linear system of two equations, arbitrarily choosing two of the three equations of (2.18). E.g., if the first and the third equations are considered, the resulting matrix of the right eigenvectors is

$$\mathbf{R} = [\mathbf{r}_1, \mathbf{r}_2, \mathbf{r}_3]\,, \quad \mathbf{r}_i = \left[1,\ \lambda_i,\ \xi\left(\frac{\partial q_s}{\partial h}\,\frac{1}{\lambda_i} + \frac{\partial q_s}{\partial q}\right)\right]^{\mathtt{T}}. \tag{2.19}$$

then, with some simple algebraic manipulations, the inverse of matrix $\mathbf{R}$ can be written in compact form as

$$\mathbf{R}^{-1} = [\mathbf{l}_1, \mathbf{l}_2, \mathbf{l}_3]^{\mathtt{T}}\,, \tag{2.20}$$

with:

$$\mathbf{l}_i = \left[-\lambda_i\,\frac{\lambda_j\,\lambda_k\frac{\partial q_s}{\partial q} + (\lambda_j + \lambda_k)\,\frac{\partial q_s}{\partial h}}{(\lambda_i - \lambda_j)\,(\lambda_i - \lambda_k)\,\frac{\partial q_s}{\partial h}},\ \frac{\lambda_i}{(\lambda_i - \lambda_j)\,(\lambda_i - \lambda_k)},\ \frac{\lambda_i\,\lambda_j\,\lambda_k}{(\lambda_i - \lambda_j)\,(\lambda_i - \lambda_k)\,\xi\frac{\partial q_s}{\partial h}}\right] \tag{2.21}$$

where $\mathbf{l}_i$ are the left eigenvectors, while i, j and k are the index of a circular permutation of 1, 2, and 3:

$$j = \begin{cases} i+1 & \text{if } i < 3 \\ i-2 & \text{otherwise} \end{cases} \qquad k = \begin{cases} i+2 & \text{if } i < 2 \\ i-1 & \text{otherwise} \end{cases} \qquad \text{with } \ i = 1, 2, 3\,. \tag{2.22}$$

In Eq. (2.20) the three row vectors $\mathbf{l}_i$ are composed column-wise to obtain the square matrix $\mathbf{R}^{-1}$.

The degree of freedom in solving (2.18) allows different combination of equations to compute $\mathbf{r}_i$ and $\mathbf{l}_i$. Thus, by choosing the first and the second equations of system (2.18), $\mathbf{r}_i$ and $\mathbf{l}_i$ becomes

$$\mathbf{r}_i = \left[1,\ \lambda_i,\ \frac{(u - \lambda_i)^2}{c^2} - 1\right]^{\mathtt{T}}. \tag{2.23}$$

and

$$\mathbf{l}_i = \left[\frac{c^2 - u^2 + \lambda_j\,\lambda_k}{(\lambda_i - \lambda_j)\,(\lambda_i - \lambda_k)},\ \frac{2u - \lambda_j - \lambda_k}{(\lambda_i - \lambda_j)\,(\lambda_i - \lambda_k)},\ \frac{c^2}{(\lambda_i - \lambda_j)\,(\lambda_i - \lambda_k)}\right] \tag{2.24}$$

According to Fig. 2.1, for the dSVE system with movable bed the three eigenvalues are always distinct and real, and thus the corresponding eigenvectors are also always distinct and real. These properties of the eigenvalues assure the well-posedness of Eqs. (2.21) and (2.24). In particular, the denominators of Eqs. (2.21) and (2.24) are always different from zero.

2.3 Analytical study of the decoupled system

Though the three roots of the characteristic polynomial can be determined exactly, the derivation of an approximate solution, obtained by a perturbative analysis, is useful for interpretation.

In system (2.2), by using Eq. (2.5) for simplicity, the two terms on the last row of matrix $\boldsymbol{\mathcal{A}}(\boldsymbol{W})$ can be written as

$$\psi = \xi \frac{\partial q_s}{\partial q} \quad \text{and} \quad \xi \frac{\partial q_s}{\partial h} = -u\psi \quad \text{with} \quad \psi = 3\,\xi \left(\frac{q_s}{q}\right) = 3\,\xi \left(A_g\, g\, \mathtt{Fr}^2\right) , \tag{2.25}$$

where ψ is the transport parameter, depending on the ratio between the flux of the sediments and the water discharge. The parameter ψ is usually small ($\psi \ll 1$), at least in the common range of river and coastal typical sediment transport rates.

Given these definitions, the flux matrix $\boldsymbol{\mathcal{A}}(\boldsymbol{W})$ can be rewritten as

$$\boldsymbol{\mathcal{A}}(\boldsymbol{W}) = \begin{bmatrix} 0 & 1 & 0 \\ c^2 - u^2 & 2u & c^2 \\ -u\,\psi & \psi & 0 \end{bmatrix} , \tag{2.26}$$

and the characteristic polynomial (2.13) becomes

$$\frac{\lambda^3}{c^3} - 2\,\mathtt{Fr}\,\frac{\lambda^2}{c^2} - \left(1 - \mathtt{Fr}^2 + \psi\right)\frac{\lambda}{c} + \mathtt{Fr}\,\psi = 0 . \tag{2.27}$$

Typically, the transport parameter ψ may be estimated as small as $O(10^{-3}$–$10^{-5})$ [e.g. 32, 35, 38, 39] therefore it seems reasonable to expand λ in powers of ψ as follows:

$$\lambda = \lambda^{(0)} + \psi\,\lambda^{(1)} + \psi^2\,\lambda^{(2)} . \tag{2.28}$$

We then substitute (2.28) into Eq. (2.27), equate likewise powers of ψ and look for the approximate solution of the three eigenvalues λ_i ($i = 1, 2, 3$). At the leading order $O(\psi^0)$, a classical result is found: one of the eigenvalues (λ_3) vanishes and the remaining two reduce to those found in the fixed bed case ($\lambda_{\mathtt{H1,H2}}$), namely

$$\lambda_{1,2} \cong \lambda_{\mathtt{H1,H2}} \equiv \lambda_{1,2}^{(0)} = \left[(\mathtt{Fr} \mp 1) + O(\psi)\right] c . \tag{2.29}$$

At the next order $O(\psi)$ small "morphodynamic" corrections for the two hydrodynamic eigenvalues, $\lambda_{1,2}$, are found and the third eigenvalue, associated with bed level changes, arises. Writing also the second order term, λ_3 reads as

$$\lambda_3 \cong \lambda_b = \left[\left(\frac{\mathtt{Fr}}{1 - \mathtt{Fr}^2}\right)\psi - \left[\frac{\mathtt{Fr}\,(\mathtt{Fr}^2 + 1)}{(1 - \mathtt{Fr}^2)^3}\right]\psi^2 + O(\psi^3)\right] c . \tag{2.30}$$

Eq. (2.30) clearly shows that the present perturbative analysis is valid provided that $\mathtt{Fr}$ is small, in fact when $\mathtt{Fr} \to 1$, λ_3 tends to infinity. Moreover, by comparing Eq. (2.29) with Eq. (2.30) it is seen that the relative order of magnitude of the celerities associated with the characteristic curves of the hyperbolic system is rather different [e.g. 21].

The behavior of such curves is well known: far from the critical state (i.e. $\mathtt{Fr} \ll 1$) the celerity of a small amplitude bed wave is considerably smaller than that of small amplitude hydrodynamic waves [39]. Therefore, the bed interacts only weakly with the water surface, thus justifying an approach in which the equations governing hydrodynamics are solved separately from those governing morphodynamics. It follows that, from a mathematical point of view, the problem can be described separately by the Saint-Venant equations for the hydrodynamics and by a simple nonlinear wave equation for morphodynamics,

$$\frac{\partial z}{\partial t} + \lambda_b \frac{\partial z}{\partial x} = 0 \, . \tag{2.31}$$

Taking into account Eq. (2.29) and Eq. (2.30), neglecting the friction term and writing the mass and momentum balance laws for the fluid phase in terms of characteristic variables u_1 and u_2 [61], the complete system of governing equations, which approximates system (2.1) when $\psi \ll 1$, can be written in *decoupled form* as

$$\frac{\partial}{\partial t} \begin{bmatrix} u_1 \\ u_2 \\ z \end{bmatrix} + \Lambda \frac{\partial}{\partial x} \begin{bmatrix} u_1 \\ u_2 \\ z \end{bmatrix} = 0 \, , \tag{2.32}$$

where

$$\begin{aligned} \Lambda &= \begin{bmatrix} \lambda_{\mathtt{H1}} & 0 & 0 \\ 0 & \lambda_{\mathtt{H2}} & 0 \\ 0 & 0 & \lambda_b \end{bmatrix} = \\ &= \begin{bmatrix} (\mathtt{Fr} - 1) + O(\psi) & 0 & 0 \\ 0 & (\mathtt{Fr} + 1) + O(\psi) & 0 \\ 0 & 0 & \dfrac{\mathtt{Fr}}{1 - \mathtt{Fr}^2}\psi + O(\psi^2) \end{bmatrix} c \, . \end{aligned} \tag{2.33}$$

According to Eqs. (2.32), in the phase space ($x - t$ plane, see Fig. 2.1b), small hydrodynamic perturbations propagate along the characteristic curves $\frac{dx}{dt} = \lambda_{\mathtt{H1,H2}}$ while small bed perturbations travel along the curve $\frac{dx}{dt} = \lambda_b$. From Eqs. (2.32) emerges that, if $\psi \ll 1$, the governing system (2.1) is well approximated by the *decoupled form* (2.32). From a mathematical point of view, Eq. (2.32) implies that the decoupling is possible when the conservative variable z coincides with one of the three characteristic variables of the morphodynamic problem.

2.3.1 Contribution of the characteristic variables to the bed adaptation

A worthy example to better understand each contribution of the characteristics variables to the bed evolution is the linearised problem proposed by Lyn & Altinakar [39]. The evolution of a small (infinitesimal) erodible hump due to a nearly uniform water flow in a straight channel is considered. Under these conditions, the problem can be studied within a linear framework, and an analytical solution can be easily derived [39].

This prototype problem is governed by the *linearized* system:

$$\frac{\partial \boldsymbol{W}}{\partial t} + \boldsymbol{\mathcal{A}}_{\mathtt{L}} \frac{\partial \boldsymbol{W}}{\partial x} = 0 \quad \text{with:} \quad \boldsymbol{\mathcal{A}}_{\mathtt{L}} = \boldsymbol{\mathcal{A}}(\boldsymbol{W}_{\mathtt{L}}) = \begin{bmatrix} 0 & 1 & 0 \\ c_{\mathtt{L}}^2 - u_{\mathtt{L}}^2 & 2u_{\mathtt{L}} & c_{\mathtt{L}}^2 \\ -u_{\mathtt{L}}\,\psi_{\mathtt{L}} & \psi_{\mathtt{L}} & 0 \end{bmatrix}, \tag{2.34}$$

where subscript $\mathtt{L}$ refers to the unperturbed state used to linearise the problem. Therefore, given the vector of unperturbed conservative variables $\boldsymbol{W}_{\mathtt{L}} = [h_{\mathtt{L}},\, q_{\mathtt{L}},\, z_{\mathtt{L}}]^T$, $u_{\mathtt{L}} = q_{\mathtt{L}}/h_{\mathtt{L}}$ is the flow velocity; $c_{\mathtt{L}} = \sqrt{g\,h_{\mathtt{L}}}$ is the unperturbed celerity; while $\psi_{\mathtt{L}}$ is the uniform sediment transport as defined in (2.25).

The initial condition of the problem is given by

$$\boldsymbol{W}_0(x) = \begin{bmatrix} h_{\mathtt{L}} \\ q_{\mathtt{L}} \\ z_0 \end{bmatrix}, \tag{2.35}$$

where: $z_0(x) = z_{\max}\exp(-x^2)$ with $z_{\max} = 1.0 \times 10^{-5}$ m, $h_{\mathtt{L}} = 1$ m, $q_{\mathtt{L}} = \sqrt{h_{\mathtt{L}}^3\, g\, \mathtt{Fr}_{\mathtt{L}}^2}$ and $\psi_{\mathtt{L}} = 0.01$. Finally, a propagation time $t_p = 15$ s is assumed.

To verify the validity of the decoupled formulation, the contribution of each characteristic variable to the bed evolution is analysed for two different values of the Froude number: $\mathtt{Fr} = 0.5$ and $\mathtt{Fr} = 0.9$.

The linearized system (2.34) can be analytically solved by adopting the characteristic method [61] and using the analytical eigenvalues (2.14) and eigenvectors (2.19). Thus, the conservative variables $\boldsymbol{W}(x)$ can be projected on the characteristic space multiplying them by the inverse of the matrix of the right eigenvectors of $\boldsymbol{\mathcal{A}}_{\mathtt{L}}$,

$$\boldsymbol{U}(x) = \boldsymbol{L}_{\mathtt{L}}\, \boldsymbol{W}(x)\,, \tag{2.36}$$

with $\boldsymbol{U}(x)$ the vector of the characteristic variables and $\boldsymbol{L}_{\mathtt{L}} = \mathbf{R}_{\mathtt{L}}^{-1}$ the inverse of the matrix of the right eigenvectors computed for the unperturbed state. Therefore, the initial conditions in terms of characteristic variables are $\boldsymbol{U}_0(x) = \boldsymbol{L}_{\mathtt{L}}\, \boldsymbol{W}_0(x)$.

Each characteristic variable $\boldsymbol{U}^{(j)}$ satisfy a linear advection equation with a celerity given by the corresponding constant eigenvalue, $\lambda_j^{\mathtt{L}}$, of $\boldsymbol{\mathcal{A}}_{\mathtt{L}}$, i.e.,

$$\frac{\partial \boldsymbol{U}^{(j)}}{\partial t} + \lambda_j^{\mathtt{L}} \frac{\partial \boldsymbol{U}^{(j)}}{\partial x} = 0 \quad \text{for} \quad j = 1,\, 2,\, 3\,. \tag{2.37}$$

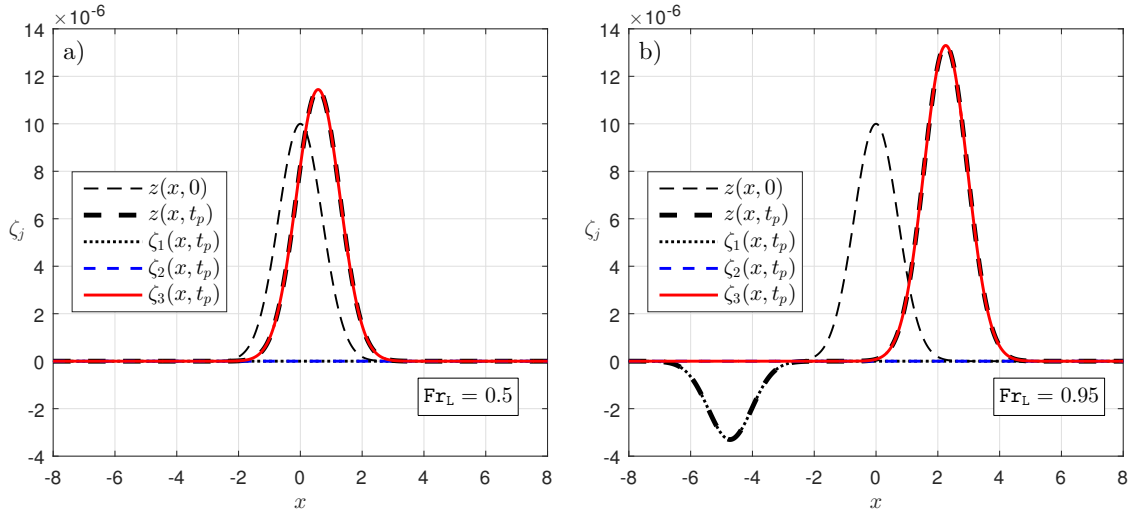

Figure 2.2: Contributions of the three characteristic variables ζ_j to the bottom topography. a) Solution of the linearized system (2.34) at $t_p = 15$ s in a weakly coupled configuration ($\psi = 0.01$, $\mathtt{Fr_L} = 0.5$); b) Solution of the linearized system (2.34) at $t_p = 15$ s in a fully coupled configuration ($\psi = 0.01$, $\mathtt{Fr_L} = 0.95$).

The corresponding solution in terms of $\boldsymbol{U}$, for a given x and t is

$$\boldsymbol{U}^{(j)}(x,t) = \boldsymbol{U}_0^{(j)}(x - \lambda_j^{\mathrm{L}}\, t) \quad \text{for} \quad j = 1,\, 2,\, 3\ . \tag{2.38}$$

The evolved conservative variables $\boldsymbol{W}(x,t)$ can be found by multiplying $\boldsymbol{U}(x,t)$ by the matrix of the right eigenvectors $\mathbf{R}_{\mathrm{L}}$,

$$\boldsymbol{W}(x,t) = \mathbf{R}_{\mathrm{L}}\, \boldsymbol{U}(x,t). \tag{2.39}$$

Focusing the attention on the bottom evolution, and indicating with $\mathbf{r}_j^{(3)}$ the third component of the j-th eigenvector of $\boldsymbol{\mathcal{A}}_{\mathrm{L}}$, the third equation of the system (2.39) can be written as

$$z(x,t) = \sum_{j=1}^{3} \mathbf{r}_j^{(3)}\, \boldsymbol{U}^{(j)}(x,t) = \sum_{j=1}^{3} \zeta_j(x,t)\ , \tag{2.40}$$

where $\zeta_j(x,t) = \mathbf{r}_j^{(3)}\, \boldsymbol{U}^{(j)}(x,t)$ represents the contribution of each component of the characteristic variables to the bottom evolution.

Numbering the eigenvalues as defined in §2.3 and computing the eigenvectors as in Eq. (2.19), Fig. 2.2 shows the comparison between the three terms $\zeta_j(x,t)$ and the bed elevation z at time $t = t_p$.

For $\mathtt{Fr} = 0.5$ (see Fig. 2.2a), the only meaningful contributions to the bed evolution is given by $\zeta_3(x,t) = \mathbf{r}_3^{(3)}\, \boldsymbol{U}^{(3)}(x,t)$ that implies $\zeta_3(x,t) \approx z(x,t)$. Furthermore, the bed form migration celerity is $\lambda_3^{\mathrm{L}} = \lambda_b$ (as stated by Eq. (2.31)), because the time

evolution of $\boldsymbol{U}^{(3)}(x,t)$ is governed by the linear advection equation (2.38). Therefore the decoupled approach can be applied to the dSVE model if $\texttt{Fr} = 0.5$ and $\psi = 0.01$.

Conversely, as shown in Fig. 2.2b, if `Fr` approach unity the bed evolution is influenced by more characteristic variables. Thus the bed form is no more uniquely related to λ_3^{L} and the decoupled approach cannot describe all the complexities of the phenomenon.

2.4 Considerations

In this chapter the one dimensional de Saint Venant - Exner mathematical model is introduced. Then a compact and easy to implement analytical formulation of the full eigenstructure of the dSVE flux matrix in proposed. Thus a theoretical study of the interactions between hydrodynamic and morphodynamic equations is performed through an approximate formulation of the three eigenvalues and the analytical solution of a linearized prototype problem.

The main result of this analysis is that, the weaker the interaction between water flow and bed response is, the more the bed evolution is described by the third characteristic variable, which is the one relates to the smaller (in absolute value) eigenvalue of the flux matrix. Therefore, when the bed responds weakly to the forcing due to the water flow, the dSVE mathematical model can be solved using a decoupled approach.

It is worth noting that the transition from the case of weak interaction to the one of full coupling between equations is usually smooth, while its smoothness depends on the intensity of the solid transport. Moreover, the simple prototype problem studied in this chapter is only one of the case in which the decoupled approach cannot well described the whole phenomenon.

However, one important conclusion of this theoretical investigation is the strict relation between the characteristic variable associate to λ_3 and the bed evolution. To well predict the morphodynamic, a proper representation of the central wave of the associated Riemann problem is mandatory, also when a fully coupled numerical scheme is adopted.

Chapter 3

Analytical implementation of the DOT Riemann solver

3.1 State of the art

The presence of the non-conservative term in the momentum equation of the dSVE system (2.1b) prevents computation of a flux function for implementation of a classic finite volume scheme. Implementation of a path-conservative (or path-consistent) scheme is an established technique to handle such non-conservative term [16, 48]. In particular, Dumbser & Toro [25] took advantage of the theoretical framework developed by Parés [48] to introduce the upwind, Osher-type, DOT Riemann solver. The DOT method is very robust, but also with the drawback of having high computational costs.

The path-conservative approach can also be applied in a centred (or symmetric) numerical framework. In this context, a recent and efficient scheme is the PRICE-C of Canestrelli *et al.* [9], a coupled scheme of the FORCE type. Therefore, among the always monotone methods, it assigns the smallest numerical viscosity within the Riemann fan [59, 61]. An upwinding of the fully coupled PRICE-C method is implemented in GIAMT2D [56], an open source numerical model developed for research aims but also suitable for practical engineering problems.

In [54], the DOT and the PRICE-C schemes are used to solve the Single Pressure Model (SPM) for the isothermal compressible two-phase flows. This non-conservative mathematical model has no simple analytical expressions for its eigenvalues. The comparison between the two schemes is performed in terms of numerical efficiency and accuracy of the corresponding solutions, in particular for the challenging simulation of near single phase flows. In general, for the same level of accuracy, the DOT scheme shows a better numerical efficiency with respect to the PRICE-C scheme. This is due to the excessive spurious dissipation of the PRICE-C central scheme. Conversely,

the DOT scheme gives less accurate results in the simulation of near single phase flows compared to the PRICE-C scheme.

The DOT and the PRICE-C schemes are also compared in [58] where both the approaches are applied to the de Saint-Venant-Exner-Hirano model for mixed-sediment morphodynamics, which is another non-conservative mathematical model without analytical expressions for eigenvalues and eigenvectors. Also in this framework the PRICE-C centred method shows a larger numerical dissipation with respect to the DOT upwind method. For this application, the DOT method results computationally inefficient. In fact, because the sediment mixture is discretized into several fractions, the de Saint-Venant-Exner-Hirano model becomes a large system of equations with an eigenstructure very cumbersome to be computed numerically.

In a preliminary work about the numerical efficiency of the DOT schemes [12] the eigenstructure is computed numerically, analytically and using an approximate solution based on a perturbative analysis. To test these different approaches a suitable set of test cases is considered in [12], without comparing the results with those of different numerical schemes or with experimental data.

In this chapter, the main results discussed in Carraro *et al.* [13] are detailed resume. In [13] an analytical implementation of the DOT solver for the one-dimensional de Saint Venant-Exner model is presented and tested by taking the original DOT and PRICE-C methods as reference. The compact formulation of the dSVE eigenstructure is used to improve the numerical efficiency and to simplify the model coding. This avoids complex numerical tools to compute eigenvalues, eigenvectors and inverse matrices, which must be calculated several times at each time step. For conciseness, hereafter the DOT method with the numerical computation of the eigenstructure replaced by such new analytical solution is denoted A-DOT.

The specific purpose of this optimization is to make more convenient the DOT solver for practical morphodynamic problems; hence it can be considered a step towards the implementation of a fully coupled morphodynamic model for a 1D and 2D river and coastal simulations. From the practical point of view, the A-DOT method can give a significant gain of computational time in long-term morphodynamic simulations. Moreover, this tool does not require the tuning of case-dependent parameters, so that its application becomes straightforward, once analytical preliminaries are established.

3.2 Path-conservative Finite Volume Schemes

A first order of accuracy path-conservative scheme reads as

$$\boldsymbol{W}_i^{n+1} = \boldsymbol{W}_i^n - \frac{\Delta t}{\Delta x}\left(\boldsymbol{\mathcal{D}}^-_{i+\frac{1}{2}} + \boldsymbol{\mathcal{D}}^+_{i-\frac{1}{2}}\right) + \Delta t\, \boldsymbol{S}\left(\boldsymbol{W}_i^n\right) , \tag{3.1}$$

in which: $\boldsymbol{W}_i^{n+1}$ and $\boldsymbol{W}_i^n$ are the cell-averaged values of the vector $\boldsymbol{W}$ at time levels t^{n+1} and t^n, respectively; $\Delta t\, \boldsymbol{S}(\boldsymbol{W}_i^n)$ is the integral of the source term within the *i-th*

cell, between time t^n and t^{n+1}; $\boldsymbol{\mathcal{D}}^{\mp}_{i\pm\frac{1}{2}}$ are the jump functions (also called fluctuations), with the compatibility condition on the cell edges

$$\boldsymbol{\mathcal{D}}^{-}_{i+\frac{1}{2}} + \boldsymbol{\mathcal{D}}^{+}_{i+\frac{1}{2}} = \int_0^1 \boldsymbol{\mathcal{A}}\left(\Psi(\boldsymbol{W}^{-}_{i+\frac{1}{2}}, \boldsymbol{W}^{+}_{i+\frac{1}{2}}, s)\right) \frac{\partial \Psi}{\partial s} \mathrm{d}s \tag{3.2}$$

with $\Psi(\boldsymbol{W}^{-}_{i+\frac{1}{2}}, \boldsymbol{W}^{+}_{i+\frac{1}{2}}, s)$ the path connecting the left state $\boldsymbol{W}^{-}_{i+\frac{1}{2}}$ and the right state $\boldsymbol{W}^{+}_{i+\frac{1}{2}}$ across the $(i+\frac{1}{2})$-*th* edge between two adjacent cells, with $s \in [0,1]$.

For the sake of simplicity, from now on the only path considered is the segment path, given by

$$\Psi(s) = \boldsymbol{W}^{-}_{i+\frac{1}{2}} + s(\boldsymbol{W}^{+}_{i+\frac{1}{2}} - \boldsymbol{W}^{-}_{i+\frac{1}{2}}). \tag{3.3}$$

Working at the first order of accuracy allows a very simple treatment of the source term. Thus, in this section we focus only on the computation of the fluctuation terms $\boldsymbol{\mathcal{D}}$. However, more general approaches should have been considered for higher order of accuracy or stiff hyperbolic balance laws [23, 24, 56].

3.2.1 The Original DOT Riemann Solver

A robust and general method to compute the jump function $\boldsymbol{\mathcal{D}}$ is an Osher type Riemann solver: the DOT (Dumbser-Osher-Toro) Riemann solver [25].

According to this method, the general jump function can be expressed as

$$\boldsymbol{\mathcal{D}}^{\pm}_{i+\frac{1}{2}} = \frac{1}{2}\int_0^1 \left[\boldsymbol{\mathcal{A}}\left(\Psi\left(\boldsymbol{W}^{-}_{i+\frac{1}{2}}, \boldsymbol{W}^{+}_{i+\frac{1}{2}}, s\right)\right) \pm \left|\boldsymbol{\mathcal{A}}\left(\Psi\left(\boldsymbol{W}^{-}_{i+\frac{1}{2}}, \boldsymbol{W}^{+}_{i+\frac{1}{2}}, s\right)\right)\right|\right] \frac{\partial \Psi}{\partial s} \mathrm{d}s\,. \tag{3.4}$$

By adoption of a G-point quadrature rule and introduction of the segment path (3.3), the discrete formulation of Eq. (3.4) becomes

$$\boldsymbol{\mathcal{D}}^{\pm}_{i+\frac{1}{2}} = \frac{1}{2}\sum_{k=1}^{G} w_{Gk}\left(\boldsymbol{\mathcal{A}}(\Psi(s_k)) \pm |\boldsymbol{\mathcal{A}}(\Psi(s_k))|\right)\left(\boldsymbol{W}^{+}_{i+\frac{1}{2}} - \boldsymbol{W}^{-}_{i+\frac{1}{2}}\right), \tag{3.5}$$

where w_{Gk} and s_k are weights and nodes of the Gauss quadrature and the usual convention for the absolute value of a matrix is applied:

$$|\boldsymbol{\mathcal{A}}| = \mathbf{R}\,|\boldsymbol{\Lambda}|\,\mathbf{R}^{-1}, \quad |\boldsymbol{\Lambda}| = \mathbf{diag}(|\lambda_1|, \cdots, |\lambda_n|)\,, \tag{3.6}$$

where $\mathbf{R}$ is the matrix of right eigenvectors of $\boldsymbol{\mathcal{A}}$, $|\boldsymbol{\Lambda}|$ is the diagonal matrix of the eigenvalues in absolute value, and $\mathbf{R}^{-1}$ is the inverse of $\mathbf{R}$ (i.e. the matrix of the left eigenvectors).

The DOT solver preserves several important properties of the Osher Riemann solver. The DOT jump is an entropy-satisfying, non-linear function. Moreover, as

shown by Dumbser & Toro [25], using the full eigenstructure of the hyperbolic system, DOT attributes an individual (and generally different) numerical viscosity to each characteristic field, and particularly to the intermediate fields. In this sense, it is a complete Riemann solver. This feature allows accurate simulation of phenomena strongly influenced by the intermediate waves, such as morhodynamic evolution.

In fact, as described in §2.3, the de Saint Venant-Exner model (2.1) has three characteristic variables: the characteristic variable related to the smallest eigenvalue (in absolute value) can be mainly associated with the bed elevation and the others with the water flow [14, 39]. Moreover, the intermediate Riemann wave in the dSVE model is related to the same smallest eigenvalue. Thus, a sharp treatment of the intermediate wave is mandatory for precise reproduction of the bed elevation.

Nevertheless, as can be deduced by Eq. (3.5), the DOT solver requires computation of the $\boldsymbol{\mathcal{A}}$ matrix eigensystem a large number of times for each time step ($G \times (\mathtt{nc}+1)$, where `nc` is the number of cells) to perform the integration along the path: the numerical computation of this eigensystem makes the DOT solver an expensive procedure from the point of view of computational cost.

3.2.2 The PRICE-C method

PRICE-C [10] is an easy to implement FORCE-type method [61] optimized for the de Saint Venant-Exner model. As an evolution of the original PRICE-T [60], it adopts one of the most efficient formulation of the jump function for centred schemes. Formally, it writes

$$\boldsymbol{\mathcal{D}}^{\pm}_{i+\frac{1}{2}} = \boldsymbol{A}^{\pm}_{i+\frac{1}{2}} \left(\boldsymbol{W}^{+}_{i+\frac{1}{2}} - \boldsymbol{W}^{-}_{i+\frac{1}{2}} \right) , \tag{3.7}$$

with

$$\boldsymbol{A}^{\pm}_{i+\frac{1}{2}} = \frac{1}{4} \left[2\, \boldsymbol{A}^{\boldsymbol{\Psi}}_{i+\frac{1}{2}} \pm \frac{\Delta x}{\Delta t} \boldsymbol{I}_m \pm \frac{\Delta t}{\Delta x} \left(\boldsymbol{A}^{\boldsymbol{\Psi}}_{i+\frac{1}{2}} \right)^2 \right] . \tag{3.8}$$

In (3.8), $\boldsymbol{A}^{\boldsymbol{\Psi}}_{i+\frac{1}{2}}$ is given by a simple integration along the path:

$$\boldsymbol{A}^{\boldsymbol{\Psi}}_{i+\frac{1}{2}} = \int_0^1 \boldsymbol{\mathcal{A}} \left(\Psi \left(\boldsymbol{W}^{-}_{i+\frac{1}{2}}, \boldsymbol{W}^{+}_{i+\frac{1}{2}}, s \right) \right) \mathrm{d}s \, ; \tag{3.9}$$

while $\boldsymbol{I}_m$ is the modified identity matrix

$$\boldsymbol{I}_m = \begin{bmatrix} 1 & 0 & 0 \\ 0 & 1 & 0 \\ 0 & 0 & \epsilon \end{bmatrix} , \tag{3.10}$$

where ϵ is a small parameter that prevents undesirable diffusion of the bed forms [9]. In general the ϵ value depends on the specific problem and can be estimated as the ratio between the slowest and the fastest celerities of the Riemann fans [56]. In this work, for each test the ϵ value has been chosen with a trial and error procedure.

Unlike an upwind approach, a centred scheme does not explicitly use wave propagation information contained in the hyperbolic system of equations [61]. This feature allows use of a jump function that does not require computation of the flux matrix eigenstructure in the development of the PRICE-C method, resulting in easy implementation and computational efficiency. The drawback is the great diffusivity of the method in terms of bed elevation, requiring introduction of the ϵ parameter to control the numerical viscosity associated with the bed evolution, for which a general case-independent value is not available.

3.2.3 Definition of the new A-DOT formulation

The main drawback of the DOT solver is the numerical computation of $|\boldsymbol{\mathcal{A}}|$ as defined in (3.6). As with Eqs. (3.4) and (3.5), its computation is required $G \times (\mathtt{nc}+1)$ times for each time step along the entire time evolution.

To avoid a lot numerical computation, by substitution in (3.6) of (2.14), (2.19) and (2.20), the DOT jump functions for the dSVE model can be computed algebraically. All the elements involved in computation of $|\boldsymbol{\mathcal{A}}|$ are defined and the proposed procedure can be summarised by the following five steps:

1. compute the derivatives of the sediment discharge (e.g. by using Eq. (2.5) to compute q_s)

$$q_s = A_g \left(\frac{q}{h}\right)^3 \quad \Rightarrow \quad \frac{\partial q_s}{\partial h} = -3\,\frac{q_s}{h} \quad \text{and} \quad \frac{\partial q_s}{\partial q} = 3\,\frac{q_s}{q}\,;$$

2. compute parameters k_1, k_2, ϕ according to Eqs. (2.15) and Eq. (2.17);

3. compute the eigenvalues according to Eqs. (2.14) and storing them in the numerical variables λ_1, λ_2, λ_3;

4. compute right and left eigenvectors, by using Eqs. (2.23) and (2.24) and the stored eigenvalues (both to avoid typing errors and for formulation clarity);

5. compute $|\boldsymbol{\mathcal{A}}|$ by the definition (3.6), as the product of three matrices

$$|\boldsymbol{\mathcal{A}}| = \begin{bmatrix} 1 & 1 & 1 \\ \lambda_1 & \lambda_2 & \lambda_3 \\ \frac{(u-\lambda_1)^2}{c^2} - 1 & \frac{(u-\lambda_2)^2}{c^2} - 1 & \frac{(u-\lambda_3)^2}{c^2} - 1 \end{bmatrix} \begin{bmatrix} |\lambda_1| & 0 & 0 \\ 0 & |\lambda_2| & 0 \\ 0 & 0 & |\lambda_3| \end{bmatrix} \cdot \begin{bmatrix} \frac{c^2-u^2+\lambda_2\,\lambda_3}{(\lambda_1-\lambda_2)(\lambda_1-\lambda_3)} & \frac{2u-\lambda_2-\lambda_3}{(\lambda_1-\lambda_2)(\lambda_1-\lambda_3)} & \frac{c^2}{(\lambda_1-\lambda_2)(\lambda_1-\lambda_3)} \\ \frac{c^2-u^2+\lambda_3\,\lambda_1}{(\lambda_2-\lambda_3)(\lambda_2-\lambda_1)} & \frac{2u-\lambda_3-\lambda_1}{(\lambda_2-\lambda_3)(\lambda_2-\lambda_1)} & \frac{c^2}{(\lambda_2-\lambda_3)(\lambda_2-\lambda_1)} \\ \frac{c^2-u^2+\lambda_1\,\lambda_2}{(\lambda_3-\lambda_1)(\lambda_3-\lambda_2)} & \frac{2u-\lambda_1-\lambda_2}{(\lambda_3-\lambda_1)(\lambda_3-\lambda_2)} & \frac{c^2}{(\lambda_3-\lambda_1)(\lambda_3-\lambda_2)} \end{bmatrix}. \tag{3.11}$$

3.3 Efficiency study

In this section, the efficiency of the proposed approaches is studied in terms of CPU time versus normalised root square errors. For each test, at the end of the simulation, we compute the normalised root square errors for the conservative variables h, q and z as

$$\mathtt{E}_{\varphi} = \frac{\sqrt{\sum_{k=1}^{\mathtt{nc}} \left(\varphi(x_k, t_{\mathtt{end}}) - \varphi^{\mathtt{ref}}(x_k, t_{\mathtt{end}})\right)^2}}{\sqrt{\sum_{k=1}^{\mathtt{nc}} \varphi^{\mathtt{ref}}(x_k, t_{\mathtt{end}})^2}} \quad \text{with:} \quad \varphi = h,\, q,\, z. \tag{3.12}$$

The $\mathtt{E}_{\varphi}$ values are plotted against the CPU times measured by performing several simulations and increasing the number of cells, $\mathtt{nc}$, within the computational grids. Then a comparison of the solutions provided by the three approaches (PRICE-C, DOT, A-DOT) is shown. The spatial resolutions are chosen to obtain similar CPU times for all the simulations.

To better perform the efficiency comparison, at this stage we neglect the bed friction in the momentum balance. From a physical point of view, this assumption introduces an inconsistency because the sediment transport is strictly related to the bed shear stress and therefore to the bed friction. Conversely, neglecting the bed friction, a tighter validation of the model is possible by considering exact analytical reference solutions.

3.3.1 Test 1: a movable-bed Riemann problem

The first test is the comparison of the numerical solution of a movable-bed Riemann problem with the corresponding analytical solution [44], commonly used as benchmark [e.g. 12]. Given a 30 m-long straight channel, the initial conditions are imposed as two constant states: one for the left portion ($x \leq 15$ m) and one for the right portion of the domain ($x > 15$ m). The values of the conservative variables for the left and right states (in double precision) are respectively

$$\boldsymbol{W}_L^0 = \begin{cases} h_L = 2.0\,\mathrm{m} \\ q_L = 0.5\,\mathrm{m}^3/(\mathrm{s\,m}) \\ z_L = 0.0\,\mathrm{m} \end{cases} \quad \text{and} \quad \boldsymbol{W}_R^0 = \begin{cases} h_R = 2.0\,\mathrm{m} \\ q_R = 4.40526631244211\,\mathrm{m}^3/(\mathrm{s\,m}) \\ z_R = -0.14000491636663\,\mathrm{m} \end{cases}. \tag{3.13}$$

The test is performed with $\xi = 1$ and $A_g = 0.01$ s^2/m for the Grass formula (2.5); $\epsilon = 1 \times 10^{-4}$ is the selected value for the small parameter in the PRICE-C method. The final time of the simulation is $t_{\mathtt{end}} = 1.5$ s.

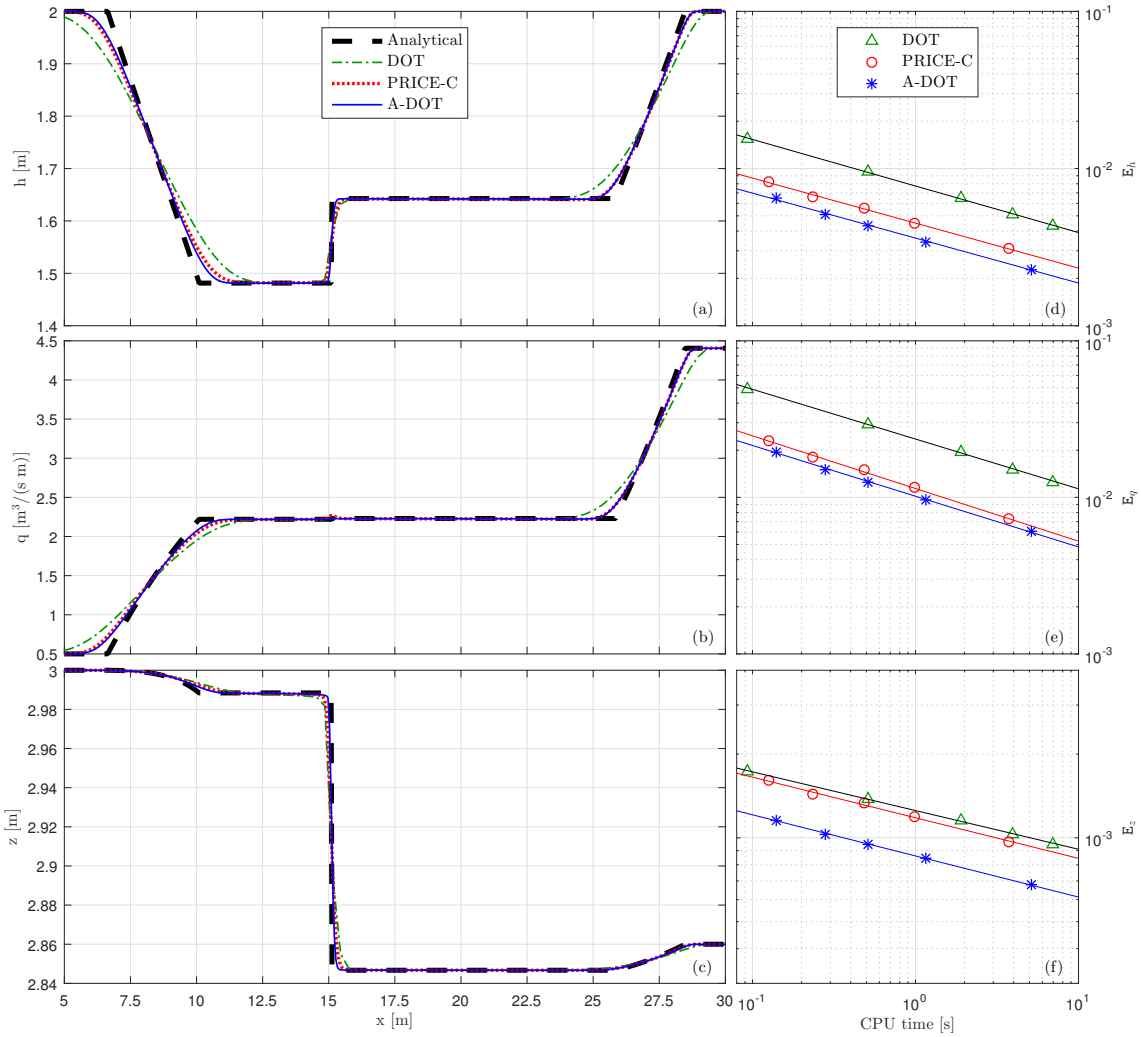

Figure 3.1: Results of Test 1. Panels *a, b* and *c*: comparison between analytical and numerical solutions (for h, q and z, respectively) at the end of the simulation (with grid size $\texttt{nc} = 100$ for the DOT scheme; $\texttt{nc} = 500$ for the PRICE-C and A-DOT schemes). Only the solutions between $x > 5$ m and $x < 30$ [m] are shown. Panels *d, e* and *f*: CPU time versus $\texttt{E}_\varphi$, Eq. (3.12), with $\varphi = h$, q and z, respectively, by using: $\texttt{nc} = [100, 250, 500, 750, 1000]$ for DOT; $\texttt{nc} = [500, 750, 1000, 1500, 3000]$ for PRICE-C and A-DOT.

For the convergence analysis, two different sets of computational grids are considered: applying the original DOT method the channel is discretized with `nc` = 100, 250, 500, 750 and 1000 cells; using the more efficient PRICE-C method and A-DOT formulation, the domain is divided into 500, 750, 1000, 1500 and 3000 cells.

Figure 3.1 shows the results of the efficiency test. Panels *a, b* and *c* show the comparison between analytical and numerical solutions at the end of the simulation in terms of conservative variables, with the coarsest grid of each set chosen to compare solutions with similar computational costs (`nc` = 100 for the DOT scheme and `nc` = 500 for the PRICE-C and A-DOT schemes, which correspond to a CPU time of about 0.1 second for all three solutions). These panels show that all the three numerical schemes well fit the analytical solution, even though the PRICE-C and A-DOT solutions are rather closer to the analytical one.

In terms of numerical efficiency, according to panels *d, e* and *f* of Fig. 3.1, all three methods converge to the exact solution with the same rate. Indeed, for each method, the computed errors lie approximately on straight lines parallel to each other. This behaviour is shown by all three methods and for all the conservative variables, verifying an overall convergence with the expected first order of accuracy.

In support of the better performance of PRICE-C and A-DOT, the right panels of Fig. 3.1 indicate that the original DOT is always the least efficient method, while PRICE-C falls between DOT and A-DOT, the last one being the most efficient. Considering only the CPU time, for a given computational grid, PRICE-C is the fastest method. Otherwise, in terms of numerical efficiency, it behaves differently depending on the considered variable: it reproduces the hydrodynamics very well (with a performance close to A-DOT), whereas the solution for the bed elevation is close to the DOT solution. Thus, for this test case, the A-DOT model is the best choice: given a target error (i.e. a fixed value for $\mathtt{E}_\varphi$), A-DOT is constantly about ten times faster than the original DOT; when the CPU time is fixed, it is always the most accurate method.

3.3.2 Test 2: smooth analytical solution

The smooth analytical solution refers to a steady-state condition for a subcritical water flow coupled with a linear-in-time bed erosion, as proposed by Berthon *et al.* [4].

For a given uniform discharge q_0 and for a sediment transport assumed to be a power function of the velocity (2.5), the analytical solution of (2.2) is given by

$$\begin{cases} u(x) = \left[\dfrac{\alpha\, x + \beta}{A_g}\right]^{1/3} \;\Rightarrow\; h(x) = q_0/u(x) \\ z(x,0) = -\dfrac{u(x)^3 + 2\, g\, q_0}{2\, g\, u(x)} + \mathtt{C} \\ z(x,t) = -\alpha\, t + z(x,0) \end{cases} \tag{3.14}$$

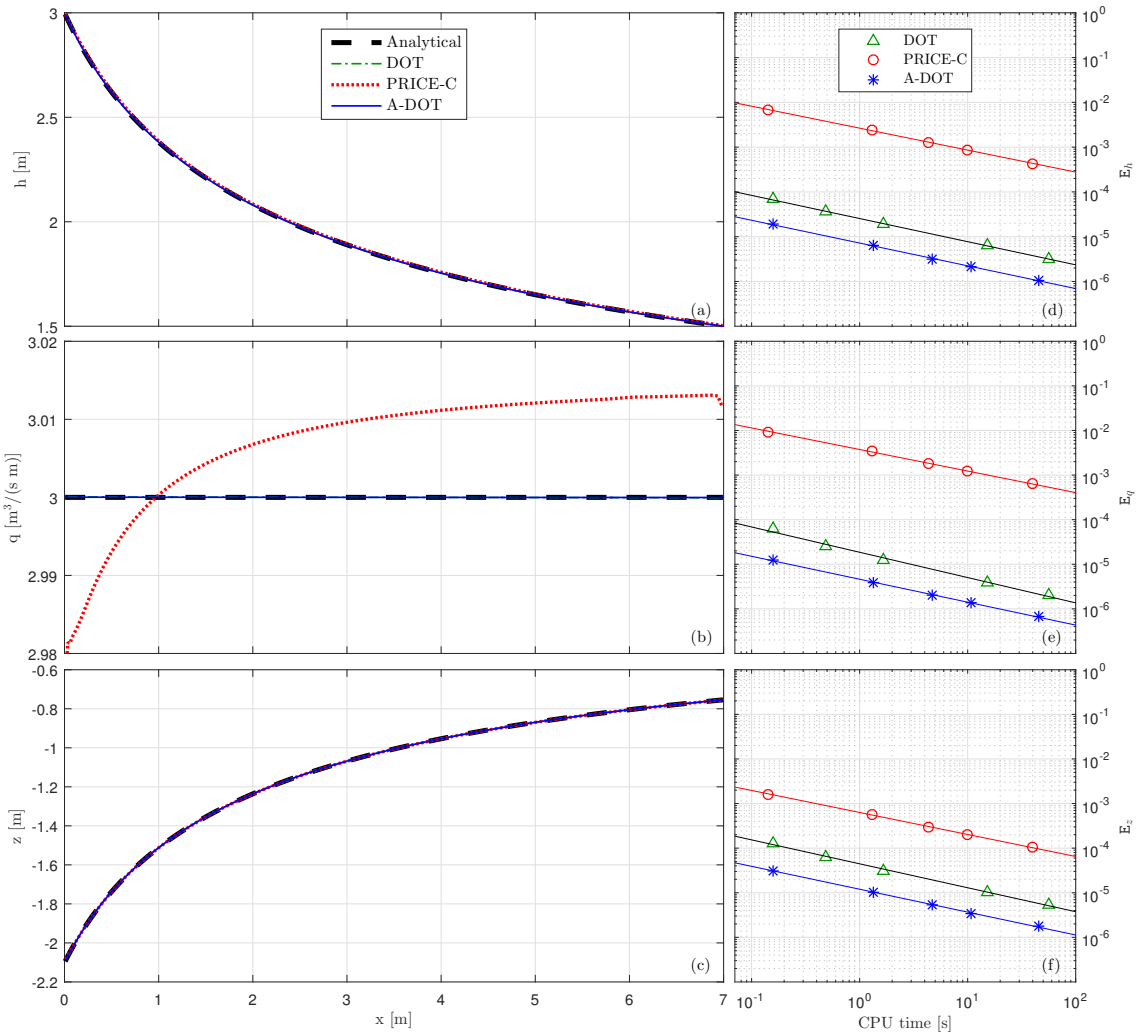

Figure 3.2: Results of Test 2. Panels *a, b* and *c*: comparison between analytical, Eq. (3.14), and numerical solutions (for h, q and z, respectively) at the end of the simulation (with grid size $\texttt{nc} = 100$ for the DOT scheme; $\texttt{nc} = 300$ for the PRICE-C and A-DOT schemes). Panels *d, e* and *f*: CPU time versus $\texttt{E}_\varphi$, Eq. (3.12), with $\varphi = h$, q and z, respectively, by using: $\texttt{nc} = [25, 50, 100, 300, 600]$ for DOT; $\texttt{nc} = [100, 300, 600, 900, 1800]$ for PRICE-C and A-DOT.

in which the constants α, β and $\mathtt{C}$ are $\alpha = \beta = A_g = 0.005$ s^2/m and $\mathtt{C} = 1$ m. The proper initial conditions are:

$$q(x,0) = q_0, \qquad h(x,0) = q_0 \left[\frac{\alpha\, x + \beta}{A_g}\right]^{-1/3}, \qquad z(x,0) = \mathtt{C} - \frac{\frac{\alpha\, x+\beta}{A_g} + 2\, g\, q_0}{2\, g\, \left(\frac{\alpha\, x+\beta}{A_g}\right)^{1/3}}, \tag{3.15}$$

while the boundary conditions, for the domain defined by $0 \leq x \leq L$, are:

$$q(0,t) = q_0, \qquad h(L,t) = q_0 \left[\frac{\alpha\, L + \beta}{A_g}\right]^{-1/3}, \qquad z(0,t) = \mathtt{C} - \frac{\frac{\beta}{A_g} + 2\, g\, q_0}{2\, g\, \left(\frac{\beta}{A_g}\right)^{1/3}} - \alpha\, t. \tag{3.16}$$

In this numerical test, the analytical solution (3.14) is applied to reproduce a 10-second evolution in a 7 m-long straight channel. As in the previous test, the domain is discretized with two different sets of grids: $\mathtt{nc} = 25$, 50, 100, 300 and 600 cells for the DOT model; $\mathtt{nc} = 100$, 300, 600, 900 and 1800 cells for the A-DOT and PRICE-C models. We used $\epsilon = 1 \times 10^{-4}$ for PRICE-C, calibrating the model in order to minimize the normalised root square error in terms of bed elevation $\mathtt{E}_z$.

Panels *a, b* and *c* in Figure 3.2 show the comparison between analytical and numerical solutions at the end of the simulation. This comparison is presented using $\mathtt{nc} = 100$ for DOT and $\mathtt{nc} = 300$ for PRICE-C and A-DOT, corresponding to a CPU time of about 1.3 seconds for all three simulations.

Figure 3.2*b* highlights a different behavior between the two versions of the DOT scheme and PRICE-C. This scheme is not able to reproduce the constant water discharge as the first two methods. Thus the whole PRICE-C solution is affected by a larger mean root square error, which also decreases the efficiency of the method in this particular test.

The difference between the PRICE-C and DOT schemes is quantified by the efficiency comparison (in the right panels of Fig. 3.2): with constant CPU time, A-DOT is almost 100 times more accurate in terms of bed elevation and 1000 times more accurate in terms of water depth and liquid discharge than PRICE-C. In spite of this marked difference, the rate of convergence of all the methods is still the same (as shown by the same slope of the fitting lines). Moreover, the mean errors measured for PRICE-C are still of the same order of magnitude as the same errors in the previous test, while DOT and A-DOT appear very much more accurate.

These results are due to the quasi-steadiness of the flow. In this condition, the bed evolution is mainly related to the intermediate wave associated with the smallest eigenvalue of the dSVE equations. Therefore, for the considerations made in section

3.2.1, it is not surprising that a complete Riemann solver like DOT, performs better than an incomplete Riemann solver like PRICE-C.

Focusing only on the comparison between the DOT and A-DOT methods, Figures 3.2*d, e* and *f* confirm that the analytical computation of $|\boldsymbol{\mathcal{A}}|$ produces a ten-time increase of the CPU performance, which remains the same for all three conservative variables. Thus, also in this test, the performance of the new implementation with respect to the original DOT increases by the same factor as in Test 1.

3.3.3 Test 3: subcritical and supercritical flow over a movable hump

The morphodynamic evolution of a bed hump is considered for the last efficiency test. A water stream with subcritical and supercritical regions flows over the hump, in a 10 m-long channel. This numerical application is inspired by the test proposed by Cordier *et al.* [18] to prove that the dSVE equations must be solved with fully coupled models to avoid non-physical instabilities of the solution.

A preliminary steady-state solution over a fixed bed ($A_g = 0.0$) is computed starting from the following initial condition:

$$\begin{cases} q(x,0) = 0.6 \text{ m}^3/\text{s m}, \\ z(x,0) = 0.1 + 0.1\, e^{-(x-5)^2} \text{ m}, \\ h(x,0) + z(x,0) = 0.4 \text{ m} \end{cases} \tag{3.17}$$

when a constant liquid discharge at the upstream boundary and transmissive conditions at the downstream boundary are imposed, the fixed bed simulation is carried out until the (frictionless) steady solution is reached. Then the bed is allowed to evolve by using $A_g = 0.0005$ s^2/m in the Grass bed-load formula (2.5).

The efficiency of the methods is evaluated in a morphodynamic evolution of 10 seconds, taking as reference the numerical solution provided by the PRICE-C method with a very refined computational grid (`nc` = 7200). The tested grids are: `nc` = 25, 50, 100, 300 cells for DOT; `nc` = 100, 300, 600 and 1200 cells for A-DOT and PRICE-C. For PRICE-C, $\epsilon = 1 \times 10^{-2}$ is used, which is higher than in the previous tests in accordance with the faster bed adaptation due to the near-critical water flow conditions.

In Figure 3.3, panels *a, b* and *c* show the comparison between reference and test solutions at the end of the simulation, corresponding to a CPU time of about 10 seconds for all three solutions, with `nc` = 300 for the DOT scheme and `nc` = 1200 for the PRICE-C and A-DOT schemes. The three methods well approximate the reference solution. Only PRICE-C presents a small difference in terms of liquid discharge where the water flow crosses the bed hump under critical conditions. Nevertheless, this can be considered a good performance for all the methods, taking into account the critical hydrodynamic conditions.

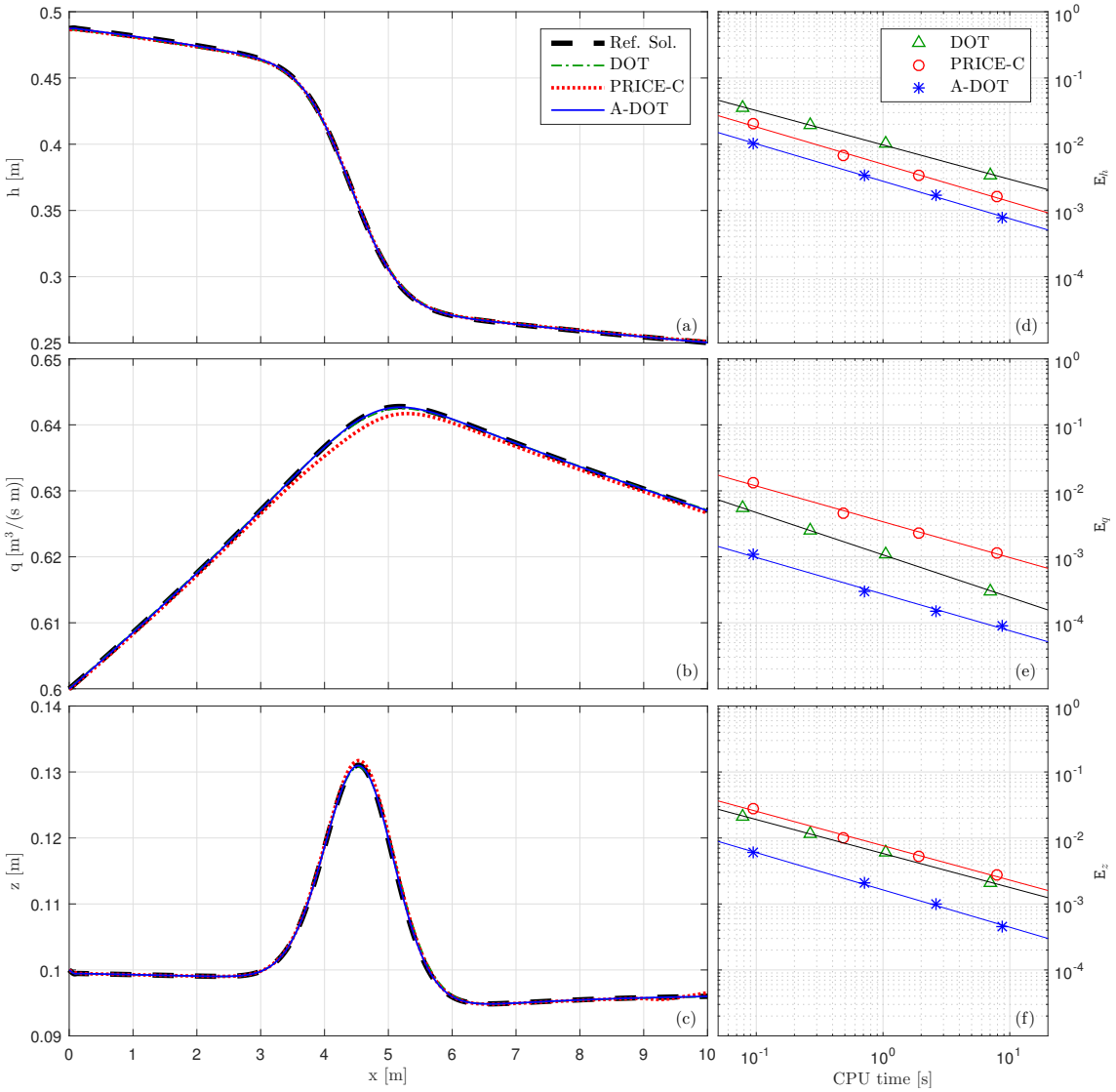

Figure 3.3: Results of Test 3. Panels *a*, *b* and *c*: comparison between reference and numerical solutions (for h, q and z, respectively) at the end of the simulation (with grid size $\texttt{nc} = 300$ for the DOT scheme; $\texttt{nc} = 1200$ for the PRICE-C and A-DOT schemes). Panels *d*, *e* and *f*: CPU time versus $\texttt{E}_\varphi$, Eq. (3.12), with $\varphi = h\ q$, and z, respectively, by using: $\texttt{nc} = [25, 50, 100, 300]$ for DOT; $\texttt{nc} = [100, 300, 600, 1200]$ for PRICE-C and A-DOT.

The efficiency study presented in panels *d, e* and *f* of Fig. 3.3 shows that, except for the liquid discharge evaluation, the numerical performance of PRICE-C is very good. Notwithstanding this, the A-DOT method still provides the best numerical efficiency in this test. Indeed, the new analytical implementation is very robust even when the water flow is characterized by critical conditions, maintaining the same performance observed in the previous two tests. In other words, A-DOT can reproduce the same solution as the original DOT, but with the advantage of being ten times faster. Moreover, the A-DOT solver is also more efficient than the PRICE-C solver in the computation of all three conservative variables.

3.4 Comparison with observed data

The proposed A-DOT numerical model, once validated on theoretical benchmarks, is here tested in a practical context. First, a case study involving a progressive channel aggradation due to sediment overfeeding [57] allows to show the advantage of the A-DOT model with respect to the PRICE-C model in terms of numerical efficiency. Then, the propagation of a sediment bore within a flume, experimentally investigated by Bellal *et al.* [3] and already used as benchmark by Canestrelli *et al.* [9], is reproduced using different transport formulae, to show the independence of the present approach from the sediment transport closure equations.

3.4.1 Aggradation due to overloading

The first test case consists of a bed aggradation in a laboratory flume due to sediment overfeeding at its upstream boundary [57]. In nature, this kind of aggradation process may be caused by a hill-side landslide into a river. The laboratory setup consisted of a 0.5 m deep and 30 m long tilting flume, equipped with a recirculatory device. The width of the flume is $B = 0.2$ m. The sediment forming the bed was sand with a median diameter of 0.32 mm and geometric standard deviation of 1.3.

Experiments started imposing a constant water discharge Q_0 at the upstream section of the channel until equilibrium sediment discharge Q_{S0}, bed slope s_0 and uniform water depth h_0 were established. This steady condition was perturbed by increasing the upstream sediment feeding from Q_{S0} to $Q_{S0} + \Delta Q_S$. As a result, the riverbed steepened leading to a progressive channel bed aggradation.

Soni *et al.* [57] performed several experimental runs changing the water discharge, the equilibrium bed slope and the sediment overfeeding amount ΔQ_S. Here, the most intense case of aggradation is considered to compare numerical results of the A-DOT and PRICE-C schemes with experimental data. In such case $\Delta Q_S = 4\, Q_{S0}$ and $Q_0 = 0.004$ m^3/s. The numerical simulations are performed considering the unit

width of the flume and therefore the initial conditions for the numerical runs are:

$$\begin{cases} h(x,0) = h_0 = 0.05 \text{ m} \\ q(x,0) = q_0 = Q_0/B = 0.02 \text{ m}^3/\text{s m} \\ z(x,0) = 1.2 - x\, s_0 \text{ m} \quad \text{with} \quad s_0 = 3.56‰ \end{cases} . \tag{3.18}$$

Constant specific liquid discharge q_0 and specific solid discharge $q_s = (Q_{S0} + \Delta Q_S)/B$ are set at the upstream boundary, while constant water depth equal to h_0 is imposed at the downstream boundary.

The solid discharge during the simulation is evaluated by a power function of velocity, similar to the Grass formula (2.5), using the original parameters experimentally derived by Soni *et al.* [57]:

$$q_s = \alpha\, u^\beta \quad \text{with} \quad \alpha = 1.45 \times 10^{-3}\,, \quad \beta = 5\,. \tag{3.19}$$

Bed porosity is assumed to be 0.4, the Strickler coefficient to be $K_s = 49.4 \text{ m}^{1/3} \text{ s}^{-1}$; the computational domain is discretized with 100 cells. Finally, the simulation time is set to $\mathtt{T_{end}} = 2400$ s.

By imposing the mass conservation of the solid phase, at the end of the simulation the aggradation of the bed at the inflow boundary results $\Delta z(0, \mathtt{T_{end}}) = 0.0675$ m.

According to Soni *et al.* [57], the final experimental bed aggradation profile, $\Delta z(x, \mathtt{T_{end}})$, is well approximated by the following empirical relationship:

$$\frac{\Delta z(x, \mathtt{T_{end}})}{\Delta z(0, \mathtt{T_{end}})} = 1 - \text{erf}\left(\frac{x}{2\sqrt{K\,t}}\right)\,, \tag{3.20}$$

where K is the aggradation coefficient which reads:

$$K = \frac{1}{\xi}\,\frac{\Delta Q_S}{\Delta z(0, \mathtt{T_{end}})}\,1.143 \times 10^{-3}\,. \tag{3.21}$$

In Fig. 3.4, the A-DOT and PRICE-C numerical results are compared with the experimental data and the empirical relationship (3.20). The numerical results obtained with the original DOT are not presented because they coincide with those obtained with the A-DOT. According to Fig. 3.4, the A-DOT numerical solution well fit experimental data, also better than the analytical function (3.20). To reproduce 2400 s of bed aggradation the A-DOT model needs 1.50 s, instead of 14.97 s of CPU time for the original DOT and 1.48 s for the PRICE-C model. For the same discretization of the computational domain and very similar CPU time, the A-DOT solution predicts the bed elevation better than the PRICE-C (empirically calibrated with $\epsilon = 0.05$).

Given the analytical approximation for the bed aggradation (3.20), imposing constant liquid discharge and the uniform depth at the downstream boundary, the

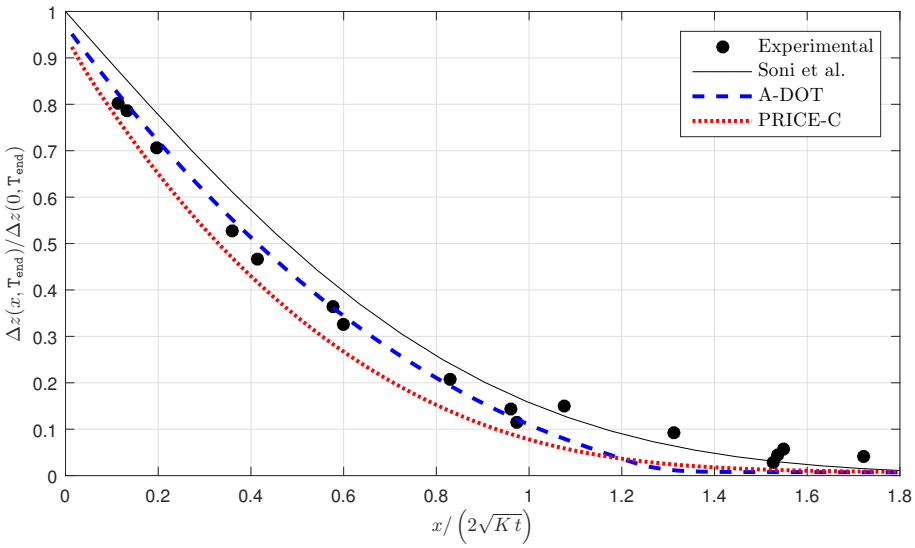

Figure 3.4: Non-dimensional bed aggradation due to sediment overfeeding of $\Delta Q_S = 4\,Q_{S0}$ at the inflow boundary, evaluated at the final time $\mathtt{T_{end}} = 2400$ s: comparison between experimental data, analytical solution (Eq. (3.20) by Soni *et al.* [57]) and numerical results of PRICE-C and A-DOT with $\mathtt{nc} = 100$. Numerical simulations start from equilibrium conditions, Eqs. (3.18) and (3.19); constant liquid discharge is imposed at the upstream boundary and uniform flow depth at the downstream section.

free surface profile at $t = \mathtt{T_{end}}$ is easily reconstructed. This reconstruction is possible assuming that the aggradation process is slow enough that the bed evolution is weakly coupled to the hydrodynamics, such that the hydrodynamic profile can be approximated with the steady water flow over an "instantaneous fixed bed". In Fig. 3.5 numerical results are compared with this reference solution. Both numerical solutions well reproduce the aggradation phenomenon, but the A-DOT is closer to the reference solution than the PRICE-C, for the same spatial resolution $\mathtt{nc} = 100$. Both methods produce very similar CPU time usage.

3.4.2 Propagation of a sediment bore

The propagation of a sediment bore is experimentally investigated by Bellal *et al.* [3]. Here, their experiments are considered to test the effect of different transport formulae on the A-DOT numerical results, similarly to what has been done in [9] for the PRICE-C scheme.

The experimental set up consists in a steep-sloped ($s_0 = 3.02\%$), 6.9 m long and 0.50 m wide, rectangular flume. The bottom is covered with a uniform coarse sand with a mean size of 1.65 mm and porosity of 0.42. Initially, the flume is fed with constant water discharge $Q = 12.0$ l/s and sediment discharge $q_s = 0.196$ l/s until the bed profile has reached a quasi-equilibrium conditions. At the time t = 0, at

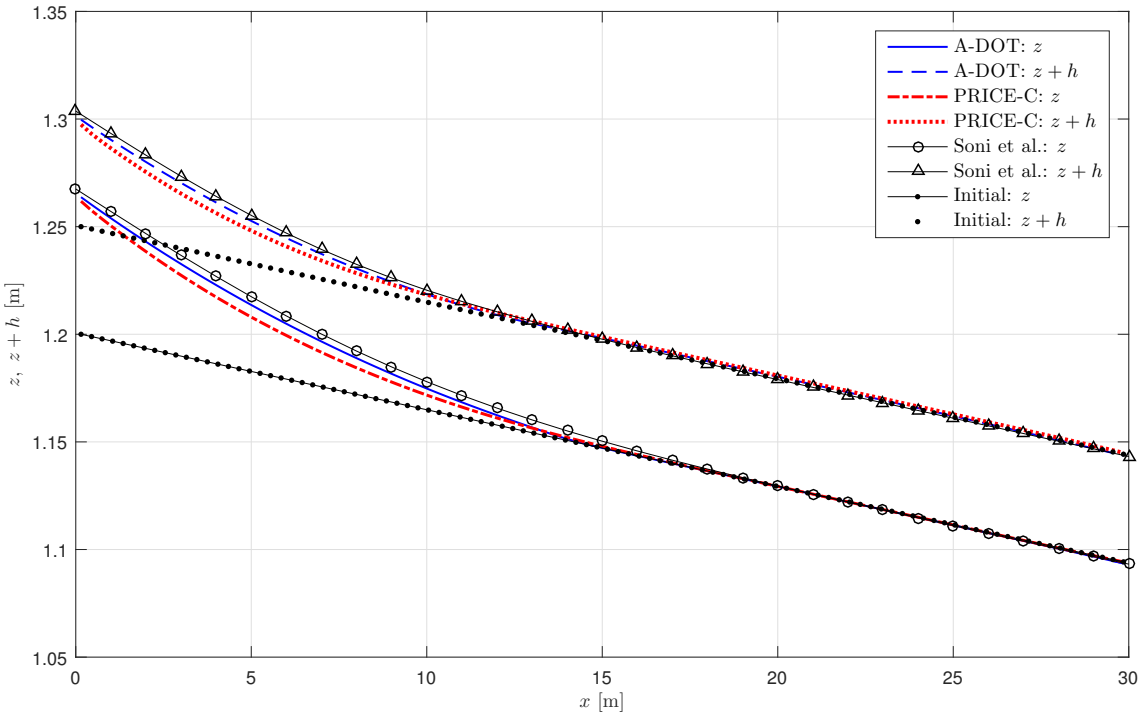

Figure 3.5: Bed and free surface profiles at the final time $\mathtt{T_{end}} = 40$ minutes: comparison between reconstructed analytical solution (Eq. (3.20) by Soni *et al.* [57]) and numerical results of PRICE-C and A-DOT with $\mathtt{nc} = 100$. Numerical simulations start from equilibrium conditions of Eqs. (3.18) and (3.19), while constant liquid discharge and sediment overfeeding of $\Delta Q_S = 4\,Q_{S0}$ are imposed at the upstream boundary and uniform flow water depth is imposed at the closure section.

the downstream end of the flume, the rapid rise of a submerged weir perturbs the equilibrium situation by imposing a subcritical condition at the closure section. The induced water level at the downstream end is $H = 20.93$ cm, while both water and sediment discharges at the upstream section are kept constant for the entire duration of the experiment. The selected Strickler coefficient is $K_s = 62$ m$^{1/3}$ s^{-1}.

The described hydraulic configuration gives rise to a moving hydraulic jump and a sediment bore which represents a demanding test case for numerical schemes. For example, they may fail in predicting the propagation celerity (i.e. the position in time) of such bore caused by the presence of transcritical flow.

Numerical simulations are performed by using the sediment transport formulae (2.7), (2.10) and the power-law (2.6). In particular, Eq. (2.6) is used with the parameters defined in [9], i.e. $A_g = 0.0024$ s^2/m and $u_{cr} = 0.3$ m/s. For all numerical simulations the same computational grid, with $\mathtt{nc} = 200$, is used.

According to Canestrelli *et al.* [9], the shock position at time t is conventionally assumed coincident with the barycentre coordinate of the first cell (starting from the

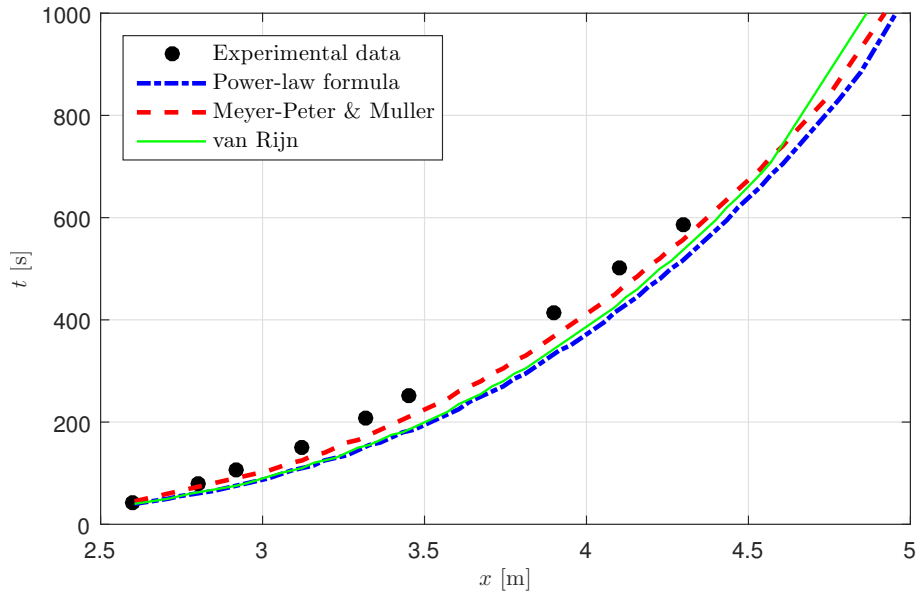

Figure 3.6: Front positions: comparison between experimental data and A-DOT scheme using three different formulae for the solid discharge.

downstream boundary) that satisfies:

$$z_i^{n+1} - z_i^n > \tau \tag{3.22}$$

where τ is a given tolerance fixed to 0.02 m in all numerical tests. In Fig. 3.6 the position of the sediment bore is plotted as a function of time for all the considered sediment discharge formulae and it is compared with the experimental data. The numerical results are close to the experimental data and are also consistent with those obtained by Canestrelli *et al.* [9]. According to Fig. 3.6, the bore celerity depends on the sediment transport formula. These results demonstrate that the proposed numerical model can be used with different transport formulae, leaving unchanged the general structure of the method.

3.5 Considerations

Within the framework of the de Saint Venant-Exner model, an analytical formulation of the flux matrix eigenstructure is used to compute the jump functions at the cell edges to improve the numerical performance of the Dumbser-Osher-Toro path-conservative scheme. A study of the numerical efficiency and a strong validation of the A-DOT scheme is presented, using as references original DOT and PRICE-C schemes and two different experimental data sets.

With the computational grid resolution fixed, the A-DOT scheme computes the solution ten times faster than DOT, keeping unchanged the accuracy of the solution

itself. Moreover, this efficiency boost does not depend on a specific test or particular morphodynamic conditions. Similarly, with a target accuracy fixed, the A-DOT scheme also presents a better performance than the efficient PRICE-C scheme.

The computational time becomes a crucial aspect when long-term morphological changes of river, estuarine and coastal environments must be studied in engineering/planning applications. The high performance of the new A-DOT scheme is also achieved by simplifying the implementation of the method. While the original DOT scheme requires the use of external numerical libraries to compute the eigenstructure of the system matrix $\boldsymbol{\mathcal{A}}$, the A-DOT jump function is merely computed as the product of three known matrices. Thus, the A-DOT scheme is both easy to implement and very portable within different coding environments and languages. Furthermore, in the framework of the de Saint Venant-Exner model, the A-DOT method is fully compatible with any kind of sediment transport formula, providing that the system of PDE remains strictly hyperbolic.

Except for the proper closure for the solid discharge and the friction factor (as typical of each movable bed problem), the method does not require any parameter calibration. Therefore, any unphysical tuning of diffusion is avoided obtaining a complete reliability and reproducibility.

The idea to increase the computational efficiency of the DOT scheme by analytically computing the eigensystem is presented only for the de Saint Venant-Exner mathematical model. Nonetheless, it can also be applied to enhance the DOT performance with other mathematical models. Moreover, for the sake of simplicity, we applied the A-DOT method to a first-order path-conservative scheme using a simple segment path, although there are no restrictions either on the order of accuracy of the method or on the path definition.

Chapter 4

Linear speedup of the bottom evolution

4.1 State of the art

Reducing the computational costs of numerical simulations of the morphological evolution in rivers, estuaries and coastal areas is a critical issue for engineers and geomorphologists [e.g. 17, 53, 55].

Even though simulation tools of physical systems have greatly benefited from the increasing computational power over the last decades thanks to progress in CPU performances and parallelization technologies, the use of morphodynamic upscaling techniques is still widely popular and becomes essential when long-term evolutions must be predicted [e.g. 17, 53, 55]. Classical approaches for morphodynamic acceleration have been developed primarily for coastal and estuarine applications [20, 33, 52]. Among them, the MORFAC (MORphological acceleration FACtor) approach [34, 52] has been introduced in the context of coastal applications, with the purpose of efficiently describing the overall morphodynamic effect of a high number of repeated tides. The MORFAC approach is now standard in state-of-the-art comercially available numerical morphological codes [51]. It is daily employed by engineers for solving practical problems in coastal and estuarine environments [17, 53] and increasingly used for the simulation of river morphodynamics [e.g. 26, 42, 46, 47].

The MORFAC approach accelerates the morphological evolution by increasing the riverbed variations in time by a given constant (> 1) factor, assuming that the morphological response to the hydrodynamic forcing is linear during one morphological time step. This is effectively obtained by multiplying the sediment flux in the Exner equation by a constant (> 1) acceleration factor updating the bed and flow within the same time step. Therefore, the key issue in the application of such an approach is to find the maximum acceleration factor (critical MORFAC in the literature) that can be applied in the numerical simulation. One of the first attempts to assess the accuracy and stability of the MORFAC approach has been carried out

by Roelvink [52], who also performed a comparison among different acceleration techniques. Even though the recent advancements [35, 51] to develop a theoretical background to detect this value are significant, the critical MORFAC is still often set by trial-and-error procedures [e.g. 26, 42, 46, 47].

In this Chapter is presented a detailed resume of the results discussed in Carraro *et al.* [14]. The main goal of this work is to develop a robust theoretical background for the development of linear morphodynamic acceleration techniques. This is obtained by performing a mathematical study to quantitatively identify the limit of application for given hydraulic and sediment-transport conditions, thereby overcoming the limits of a trial and error approach.

Taking advantage of the theoretical study performed in Chapter 2, the proposed mathematical framework to investigate linear morphodynamic accelerations is developed by considering a non-uniformly accelerated dSVE model. Each of the three governing equations (water and sediment continuity, and conservation of momentum) is accelerated by a constant acceleration factor (> 1), namely $\mathtt{M}_{\mathrm{cw}}$, $\mathtt{M}_{\mathrm{cs}}$ and $\mathtt{M}_{\mathrm{q}}$. The final goal is to identify the most convenient combination of the three accelerating factors, to be applied within each single time step, for which i) the bed still responds linearly to hydrodynamic changes; and ii) a consistent decrease of the computational time is obtained.

The analysis is carried out by applying the non-uniform acceleration to analytical and approximated eigenvalue formulations of the flux matrix derived in §2.3. The study of the non-uniformly accelerated eigenvalues allows the derivation of a new linear morphodynamic acceleration technique, which has been dubbed MASSPEED (MASs equations SPEEDup) [14]. This is obtained by setting $\mathtt{M}_{\mathrm{cw}} = \mathtt{M}_{\mathrm{cs}} > 1$, $\mathtt{M}_{\mathrm{q}} = 1$ and it is characterized by a larger validity range for linear acceleration and higher computational speed-up than that of the classical MORFAC approach, which is obtained by setting $\mathtt{M}_{\mathrm{cw}} = \mathtt{M}_{\mathrm{q}} = 1, \mathtt{M}_{\mathrm{cs}} > 1$. Finally, the new MASSPEED approach is implemented using an adaptive approach, similarly to that used for implementing the Courant–Friedrichs–Lewy numerical stability condition. It is then applied to the long-term propagation of a sediment hump with the aim of demonstrating that it is able i) to correctly predict the time evolution with and without friction terms; ii) to decrease considerably the computational costs.

4.2 A general framework for morphodynamic acceleration

As described in §2.3, small hydrodynamic and bed disturbances propagate along the characteristic curves with celerities given by the eigenvalues of the flux matrix (2.26). Therefore, linear acceleration of the propagation of small disturbances can be obtained by increasing the slope of such characteristic curves.

If the original de Saint Venant - Exner system of governing equations (2.2) is considered, neglecting friction terms ($\boldsymbol{S} = \boldsymbol{0}$), acceleration can be obtained by

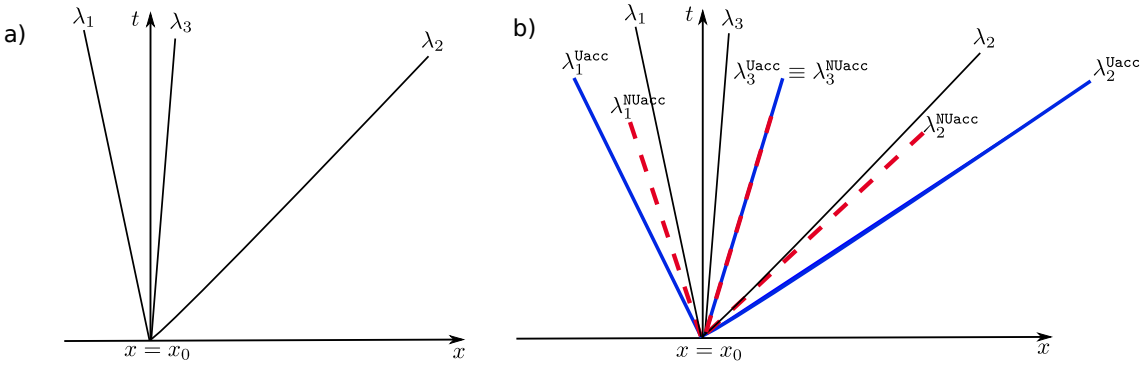

Figure 4.1: Sketch of (linearized) characteristic curves in the phase space. In panel a) the typical situation for subcritical conditions ($u > 0$) is given. In panel b) the original system (black thin lines) the uniformly accelerated system (`Uacc`) (blue thick lines) and the non-uniformly accelerated system (`NUacc`) (red dashed lines) are sketched. The definitions of uniformly and non-uniformly accelerated systems are given in the text.

multiplying from the left the *original* flux matrix by the acceleration matrix $\boldsymbol{\mathcal{M}}$, namely

$$\frac{\partial \boldsymbol{W}}{\partial t} + \boldsymbol{\mathcal{M}}\,\boldsymbol{\mathcal{A}}(\boldsymbol{W})\frac{\partial \boldsymbol{W}}{\partial x} = 0\,, \qquad \boldsymbol{\mathcal{M}} = \begin{bmatrix} \mathtt{M}_{\mathrm{cw}} & 0 & 0 \\ 0 & \mathtt{M}_{\mathrm{q}} & 0 \\ 0 & 0 & \mathtt{M}_{\mathrm{cs}} \end{bmatrix}, \tag{4.1}$$

in which three scalar acceleration coefficients are introduced, $\mathtt{M}_{\mathrm{cw}}$ for the water continuity equation, $\mathtt{M}_{\mathrm{q}}$ for the momentum equation, and $\mathtt{M}_{\mathrm{cs}}$ for the sediment continuity equation.

In this section two configurations of $\boldsymbol{\mathcal{M}}$ are discussed: a simple case of uniform acceleration (`Uacc`) of the whole system with $\mathtt{M}_{\mathrm{cw}} = \mathtt{M}_{\mathrm{q}} = \mathtt{M}_{\mathrm{cs}} = \mathtt{M} > 1$, and the case of non-uniform acceleration (`NUacc`) in which each equation is accelerated by a specific, and in general different, factor ($\mathtt{M}_{\mathrm{cw}} \geq 1$, $\mathtt{M}_{\mathrm{q}} \geq 1$, $\mathtt{M}_{\mathrm{cs}} \geq 1$). In particular, for the non-uniformly accelerated system an approximate set of eigenvalues and suitable definitions for the numerical speed-up are presented.

4.2.1 The trivial case of uniform acceleration (`Uacc`)

In this section, a *uniformly accelerated* system is analysed from a computational point of view. Setting $\mathtt{M}_{\mathrm{cw}} = \mathtt{M}_{\mathrm{q}} = \mathtt{M}_{\mathrm{cs}} = \mathtt{M} > 1$ in (4.1), the resulting system of equations reduce to:

$$\frac{\partial \boldsymbol{W}}{\partial t} + \mathtt{M}\,\boldsymbol{\mathcal{A}}(\boldsymbol{W})\frac{\partial \boldsymbol{W}}{\partial x} = 0\,. \tag{4.2}$$

Making use of the eigenvalues and eigenvectors properties, it is easy to verify that all the three eigenvalues of $\boldsymbol{\mathcal{A}}$ scale linearly with $\mathtt{M}$. In other words, the uniformly accelerated eigenvalues are $\lambda_i^{\mathtt{Uacc}} = \mathtt{M}\,\lambda_i$. In this case, hydrodynamic and morphodynamic information are accelerated linearly by the same factor; therefore,

the slopes of the three characteristic curves will be larger and all proportional to M. The corresponding situation in the phase space is depicted in Fig. 4.1b, where characteristic curves related to the uniformly accelerated system are displayed with thick-blue continuous lines.

It is interesting to analyse the consequences of this acceleration when a numerical solution of system (4.2) is sought and the adopted scheme must satisfy the Courant-Friedrichs-Lewy (CFL) condition. The CFL condition is the necessary restraint that a numerical solution (using a finite volume or finite difference method) must satisfy to be stable and to converge to the exact solution as the grid is refined [61].

If the spatial domain is discretized with a grid having a constant mesh size Δx, the numerical solution of the original system (2.2) is advanced in time by a time step Δt that must satisfy the following CFL condition:

$$\Delta t \leq \mathtt{CFL}\,\frac{\Delta x}{\max(\lambda_i)}. \tag{4.3}$$

where: CFL is the Courant–Friedrichs–Lewy number with specific values depending upon the selected time integration technique; $\max(\lambda_i)$ is the maximum eigenvalue associated to the flux matrix (2.26) which, if $u > 0$, results $\max(\lambda_i) = \lambda_2$, as in Fig. 4.1a. For the uniformly accelerated system the maximum time step that can be adopted is

$$\Delta t_{\mathtt{Uacc}} = \mathtt{CFL}\,\frac{\Delta x}{\lambda_2^{\mathtt{Uacc}}}\,. \tag{4.4}$$

Since $\lambda_2^{\mathtt{Uacc}} = \mathtt{M}\,\lambda_2$, Eqs. (4.3) and (4.4) imply

$$\Delta t_{\mathtt{Uacc}} = \mathtt{CFL}\,\frac{\Delta x}{\mathtt{M}\,\lambda_2} \quad \Rightarrow \quad \Delta t_{\mathtt{Uacc}} = \frac{\Delta t}{\mathtt{M}}\,. \tag{4.5}$$

This means that, if a uniform acceleration M is imposed, time integration of the accelerated system requires a time step which is M-times smaller to that of the original system. Moreover, to take into account the acceleration of the morphological evolution, the time must be scaled in the accelerated framework. In particular, if a given propagation time t_p related to the simulation performed by using the original system is considered, the corresponding propagation time related to the uniformly accelerated system is $t_p/\mathtt{M}$.

Therefore, the propagation time and the time step in the accelerated framework are both scaled by M, so that the numerical solution at a given output time t_p of the original and the uniformly accelerated systems requires the same number of time steps; *consequently no computational gain is obtained by using the* Uacc *procedure.*

4.2.2 The case of non-uniform acceleration (NUacc)

Given the conclusion of the previous section, if a computational gain is sought, a non-uniform acceleration must be considered. The final goal is to find an appropriate

combination of the three accelerating factors ($\mathtt{M}_{\mathrm{cw}} \geq 1, \mathtt{M}_{\mathrm{q}} \geq 1, \mathtt{M}_{\mathrm{cs}} \geq 1$) with a twofold objective, as follows:

(i) *obtaining a linear acceleration for morphodynamics.* This can be obtained when the bottom time evolution can be described by the following accelerated wave equation

$$\frac{\partial z}{\partial t} + \mathtt{M}_{\mathrm{cs}} \lambda_b \frac{\partial z}{\partial x} = 0 \,. \tag{4.6}$$

Therefore, the physical and mathematical conditions under which the accelerated system of governing equations can be written in the decoupled form (2.32) must be defined. The linear acceleration allows to precisely describe the propagation of the bed level in the accelerated phase space, providing a linear correspondence between the time scales of the non-accelerated and the accelerated morphodynamic process.

(ii) *increasing the numerical speed-up.* This means that, if the morphodynamic process is accelerated by a constant factor $\mathtt{M}_{\mathrm{cs}}$, the corresponding acceleration of the hydrodynamic process should not reduce the numerical speed-up. That is, the largest eigenvalue of the system of the governing equations (λ_2) must be accelerated by a factor smaller than the morphodynamic acceleration factor.

Graphical representation on the phase space of the two conditions i) and ii) is given in Fig. 4.1b.

4.2.3 Analytical eigenvalues for the `NUacc` system

Similarly to Eq. (2.13), the characteristic polynomial associated to system (4.1), is obtained by imposing $|\boldsymbol{\mathcal{M}}\,\boldsymbol{\mathcal{A}}(\boldsymbol{W}) - \lambda \boldsymbol{I}| = 0$; it reads

$$\frac{\lambda^3}{c^3} - 2\,\mathtt{M}_{\mathrm{q}}\,\mathtt{Fr}\,\frac{\lambda^2}{c^2} + \mathtt{M}_{\mathrm{q}} \left(\mathtt{M}_{\mathrm{cw}}\,\mathtt{Fr}^2 - \mathtt{M}_{\mathrm{q}} - \mathtt{M}_{\mathrm{cs}}\,\xi \frac{\partial q_s}{\partial q} \right) \frac{\lambda}{c} - \frac{\mathtt{M}_{\mathrm{cs}}\mathtt{M}_{\mathrm{cw}}\mathtt{M}_{\mathrm{q}}}{c}\,\xi \frac{\partial q_s}{\partial h} = 0 \,. \tag{4.7}$$

Introducing the non-uniform acceleration, the *original eigenvalues* (2.14) becomes

$$\frac{\lambda_1^{\mathtt{NUacc}}}{c} = \frac{2}{3}\mathtt{M}_{\mathrm{q}}\,\mathtt{Fr} - \frac{2}{3}\sqrt{k_{\mathtt{M}1}}\,\cos\left(\frac{\phi_{\mathtt{M}}}{3} - \frac{\pi}{3}\right), \tag{4.8a}$$

$$\frac{\lambda_2^{\mathtt{NUacc}}}{c} = \frac{2}{3}\mathtt{M}_{\mathrm{q}}\,\mathtt{Fr} + \frac{2}{3}\sqrt{k_{\mathtt{M}1}}\,\cos\left(\frac{\phi_{\mathtt{M}}}{3}\right), \tag{4.8b}$$

$$\frac{\lambda_3^{\mathtt{NUacc}}}{c} = \frac{2}{3}\mathtt{M}_{\mathrm{q}}\,\mathtt{Fr} - \frac{2}{3}\sqrt{k_{\mathtt{M}1}}\,\cos\left(\frac{\phi_{\mathtt{M}}}{3} + \frac{\pi}{3}\right), \tag{4.8c}$$

where the parameters $\phi_{\mathtt{M}}$ and $k_{\mathtt{M1}}$ are:

$$\phi_{\mathtt{M}} = \arccos\left(\frac{k_{\mathtt{M2}}}{\sqrt{4\,{k_{\mathtt{M1}}}^3}}\right), \tag{4.9}$$

$$k_{\mathtt{M1}} = 4\,\mathtt{M}_{\mathrm{q}}^2\,\mathtt{Fr}^2 + 3\,\mathtt{M}_{\mathrm{q}}\,\mathtt{M}_{\mathrm{cs}}\,\xi\frac{\partial q_s}{\partial q} + 3\,\mathtt{M}_{\mathrm{cw}}\,\mathtt{M}_{\mathrm{q}}\left(1-\mathtt{Fr}^2\right). \tag{4.10}$$

with $k_{\mathtt{M2}}$ given by:

$$k_{\mathtt{M2}} = 2\,\mathtt{M}_{\mathrm{q}}^2\,\mathtt{Fr}\left(8\,\mathtt{M}_{\mathrm{q}}\,\mathtt{Fr}^2 + 9\,\mathtt{M}_{\mathrm{cs}}\,\xi\frac{\partial q_s}{\partial q} + 9\,\mathtt{M}_{\mathrm{cw}}\left(1-\mathtt{Fr}^2\right)\right) + 27\,\mathtt{M}_{\mathrm{cw}}\,\mathtt{M}_{\mathrm{q}}\,\mathtt{M}_{\mathrm{cs}}\,\xi\frac{\partial q_s}{\partial h}, \tag{4.11}$$

Given the eigenvalue $\lambda_i^{\mathtt{NUacc}}$, the associated right eigenvector $\mathbf{r}_i^{\mathtt{NUacc}}$ can be defined by solving the linear system $\boldsymbol{\mathcal{M}}\,\boldsymbol{\mathcal{A}}\,\mathbf{r}_i^{\mathtt{NUacc}} = \lambda_i^{\mathtt{NUacc}}\,\mathbf{r}_i^{\mathtt{NUacc}}$. Therefore, similarly to Eq. (2.19), the matrix $\mathbf{R}^{\mathtt{NUacc}}$ of the right eigenvectors can be expressed as a function of the accelerated eigenvalues, the result being (neglecting the superscript `NUacc` for brevity)

$$\mathbf{R} = [\mathbf{r}_1, \mathbf{r}_2, \mathbf{r}_3], \quad \text{with:} \quad \mathbf{r}_i = \left[1,\ \frac{\lambda_i}{\mathtt{M}_{\mathrm{cw}}},\ \xi\frac{\mathtt{M}_{\mathrm{cs}}}{\mathtt{M}_{\mathrm{cw}}}\left(\frac{\mathtt{M}_{\mathrm{cw}}}{\lambda_i}\frac{\partial q_s}{\partial h} + \frac{\partial q_s}{\partial q}\right)\right]^{\mathtt{T}}. \tag{4.12}$$

while, similarly to Eqs. (2.20) and (2.21), the inverse of matrix of the accelerated eigenvectors can be written as

$$\mathbf{R}^{-1} = [\mathbf{l}_1, \mathbf{l}_2, \mathbf{l}_3]^{\mathtt{T}}, \tag{4.13}$$

with:

$$\begin{aligned}\mathbf{l}_i = \Bigg[& -\frac{\lambda_i}{\mathtt{M}_{\mathrm{cw}}}\left(\frac{\lambda_j\,\lambda_k\frac{\partial q_s}{\partial q} + \mathtt{M}_{\mathrm{cw}}\,(\lambda_j+\lambda_k)\,\frac{\partial q_s}{\partial h}}{(\lambda_i-\lambda_j)\,(\lambda_i-\lambda_k)\,\frac{\partial q_s}{\partial h}}\right), \\ & \frac{\mathtt{M}_{\mathrm{cw}}\,\lambda_i}{(\lambda_i-\lambda_j)\,(\lambda_i-\lambda_k)},\ \frac{\lambda_i\,\lambda_j\,\lambda_k}{\mathtt{M}_{\mathrm{cs}}\,(\lambda_i-\lambda_j)\,(\lambda_i-\lambda_k)\,\xi\frac{\partial q_s}{\partial h}}\Bigg]\end{aligned} \tag{4.14}$$

where $\mathbf{l}_i$ are the accelerated left eigenvectors (neglecting the superscript `NUacc` for brevity), while i, j and k are the index of a circular permutation of 1, 2, and 3, as defined in (2.22):

$$j = \begin{cases} i+1 & \text{if } i<3 \\ i-2 & \text{otherwise} \end{cases} \qquad k = \begin{cases} i+2 & \text{if } i<2 \\ i-1 & \text{otherwise} \end{cases} \qquad \text{with } \ i = 1,2,3\,.$$

4.2.4 Approximate eigenvalues for the NUacc system

To study the combination of $[\mathtt{M}_{cw}, \mathtt{M}_q, \mathtt{M}_{cs}]$ such as $\lambda_3^{\mathtt{NUacc}} = \mathtt{M}_{cs}\,\lambda_3$, a simplification of expressions (4.8) is mandatory. An approximate solution of the three eigenvalues $\lambda_i^{\mathtt{NUacc}}$ can be derived by adopting the perturbative analysis of Eq. (2.28), in §2.3. By taking advantage of the typically small magnitude of the sediment transport intensity ψ, as defined in Eq. (2.25) at p. 10, the characteristic polynomial (4.7) becomes

$$\frac{\lambda^3}{c^3} - 2\,\mathtt{M}_q\,\mathtt{Fr}\,\frac{\lambda^2}{c^2} + \mathtt{M}_q\left(\mathtt{M}_{cw}\,\mathtt{Fr}^2 - \mathtt{M}_q - \mathtt{M}_{cs}\,\psi\right)\frac{\lambda}{c} - \mathtt{M}_{cs}\mathtt{M}_{cw}\mathtt{M}_q\mathtt{Fr}\,\psi = 0 \tag{4.15}$$

compare this with (2.27).

Assuming expansion (2.28) for the solution of equation (4.15) to $O(\psi)$, the eigenvalues associated to the hydrodynamics become

$$\begin{aligned}\frac{\lambda_{1,2}^{\mathtt{NUacc}}}{c} \cong\ & \mathtt{M}_q\left[\mathtt{Fr} \mp \sqrt{\mathtt{Fr}^2 + \frac{\mathtt{M}_{cw}}{\mathtt{M}_q}\left(1-\mathtt{Fr}^2\right)}\right] + \\ & + \mathtt{M}_{cs}\left[\frac{\sqrt{\dfrac{\mathtt{M}_{cw}}{\mathtt{M}_q}\dfrac{1-\mathtt{Fr}^2}{\mathtt{Fr}^2}+1} + \left(1-\dfrac{\mathtt{M}_{cw}}{\mathtt{M}_q}\right)}{\sqrt{\dfrac{\mathtt{M}_{cw}}{\mathtt{M}_q}\dfrac{1-\mathtt{Fr}^2}{\mathtt{Fr}^2}+1} + \left(1-\dfrac{\mathtt{M}_{cw}}{\mathtt{M}_q}\right) + \frac{1}{\mathtt{Fr}^2}\dfrac{\mathtt{M}_{cw}}{\mathtt{M}_q}}\right]\frac{\psi}{2\mathtt{Fr}}\,.\end{aligned} \tag{4.16}$$

At $O(\psi^2)$, the celerity associated with the bed level changes is given by

$$\frac{\lambda_3^{\mathtt{NUacc}}}{c} \cong \mathtt{M}_{cs}\left[\left(\frac{\mathtt{Fr}}{1-\mathtt{Fr}^2}\right)\psi - \left(\frac{\mathtt{M}_{cs}}{\mathtt{M}_{cw}}\frac{\mathtt{Fr}\left(\mathtt{Fr}^2+1\right)}{\left(1-\mathtt{Fr}^2\right)^3}\right)\psi^2\right]\,. \tag{4.17}$$

It is clear that, also for the non-uniformly accelerated system, when $\mathtt{Fr} \to 1$, $\lambda_3^{\mathtt{NUacc}} \to \infty$. Therefore the assumptions on the perturbation expansion are no longer valid [38].

4.2.5 Theoretical and computational speed-up

The goal of this section is to derive a general theoretical definition for the speed-up of the non-uniform acceleration approach. This is the mean which allows quantifying the computational gain for a given morphological simulation.

According to Eq. (4.5) a uniform acceleration applied to both hydrodynamic and morphological evolutions does not result in any computational speed-up. Quite contrary, one can expect to have a speed-up when the eigenvalue corresponding to the bottom evolution, $\lambda_3^{\mathtt{NUacc}}$, is accelerated by a factor $\mathtt{M}_{cs}$ compared to the corresponding eigenvalue of the original system $\lambda_3^{\mathtt{NUacc}} = \mathtt{M}_{cs}\lambda_3$ and at the same time the maximum eigenvalue of the hydrodynamic system, $\lambda_2^{\mathtt{NUacc}}$, results to be accelerated by a factor

$< \mathtt{M}_{\mathrm{cs}}$ as compared to its homologous in the original system λ_2. For the sake of generality, the averaged theoretical speed-up over a simulation time $T_{\mathtt{S}}$ is defined as the ratio between the instantaneous morphological $\mathtt{R}_{\mathtt{M}}(\tau)$ and hydrodynamic $\mathtt{R}_{\mathtt{H}}(\tau)$ acceleration,

$$\mathtt{Sp} = \frac{1}{T_{\mathtt{S}}} \int_0^{T_{\mathtt{S}}} \frac{\mathtt{R}_{\mathtt{M}}(\tau)}{\mathtt{R}_{\mathtt{H}}(\tau)}\, d\tau \ . \tag{4.18}$$

If the condition for Eq. (4.6) is satisfied, i.e. the `NUacc` system can be written in a decoupled way, the acceleration terms $\mathtt{R}_{\mathtt{M,H}}(\tau)$ are the ratios between the accelerated and original eigenvalues,

$$\mathtt{R}_{\mathtt{M}}(\tau) = \frac{\lambda_3^{\mathtt{NUacc}}(\tau)}{\lambda_3(\tau)}\,, \quad \mathtt{R}_{\mathtt{H}}(\tau) = \frac{\lambda_2^{\mathtt{NUacc}}(\tau)}{\lambda_2(\tau)}. \tag{4.19}$$

It is worth noting that, if the acceleration factors $\mathtt{R}_{\mathtt{M,H}}$ are set constant over the whole simulation time, equation (4.18) simplifies to $\mathtt{Sp} = \mathtt{R}_{\mathtt{M}}/\mathtt{R}_{\mathtt{H}}$.

In a similar way the computational speed-up can be defined as the ratio between the computational time (CPU time) of the reference solution and the accelerated one,

$$\mathtt{Sp}^{\mathtt{CPU}} = \frac{\mathtt{CPU(Ref.Sol.)}}{\mathtt{CPU(Acc.Sol.)}}\,. \tag{4.20}$$

4.3 Linear morphodynamic acceleration techniques

In this section the classical MORFAC (`MF`) and the newly proposed MASSPEED (`MS`) acceleration techniques are considered. For both methods, the conditions under which a linear acceleration is possible are identified, and the maximum theoretical speed-up is quantified. Moreover, in §4.3.3 a simple application is introduced to explain why the expression of the exact acceleration of $\lambda_3^{\mathtt{NUacc}}$ is a necessary condition to correctly reproduce the riverbed profile with both MORFAC and MASSPEED approaches.

4.3.1 The classical MORFAC approach

The classical MORFAC approach described in Roelvink [52] is obtained when the acceleration coefficients are set to $\mathtt{M}_{\mathrm{cs}} = \mathtt{MF} > 1$, $\mathtt{M}_{\mathrm{q}} = \mathtt{M}_{\mathrm{cw}} = 1$. Substitution of these values into Eqs. (4.16) and (4.17) gives

$$\frac{\lambda_{1,2}^{\mathtt{MF}}}{c} = [\mathtt{Fr} \mp 1] + O(\mathtt{MF}\,\psi)\,, \tag{4.21}$$

$$\frac{\lambda_3^{\mathtt{MF}}}{c} = \left[\frac{\mathtt{Fr}}{1-\mathtt{Fr}^2}\right](\mathtt{MF}\,\psi) - \left[\frac{\mathtt{Fr}\,(\mathtt{Fr}^2+1)}{(1-\mathtt{Fr}^2)^3}\right](\mathtt{MF}\,\psi)^2\ . \tag{4.22}$$

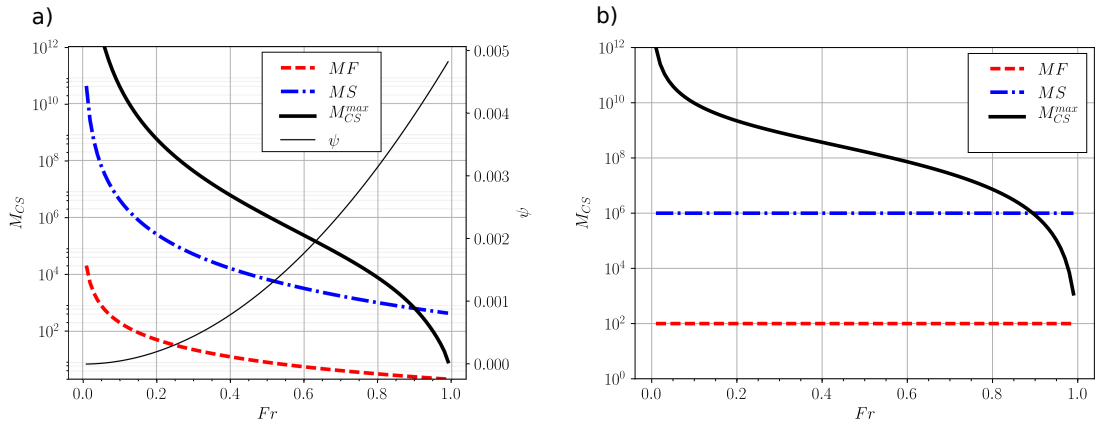

Figure 4.2: Range of validity for the linear morphodynamic acceleration for MORFAC (red dashed line) and MASSPEED (blue dash-dotted line) techniques. In panel a) the curves are obtained by setting $A_g = 0.0001$, $\epsilon = 0.01$ in relations (4.24) and (4.30) and using the definition of ψ in (2.25). In panel b) the displayed curves are obtained by setting the constant $\psi = 10^{-4}$ in relations (4.24) and (4.30).

The accelerated MORFAC system (4.1) can be written in the decoupled form (2.32) if $\lambda_3^{\mathtt{MF}} \ll \lambda_2^{\mathtt{MF}}$. This condition is satisfied provided that

$$\mathtt{MF}\left[\frac{\mathtt{Fr}}{1-\mathtt{Fr}^2}\right]\psi \ll [\mathtt{Fr}+1] \ . \tag{4.23}$$

For $\mathtt{Fr}$ numbers typical of environmental flows, i.e. far enough from unity, the term on the left of the inequality (4.23) is of $O(\mathtt{MF}\,\psi)$, while the term on the right side is of $O(1)$. Therefore, the resulting range of validity, for which the decoupled approach holds, is

$$\mathtt{MF}\,\psi = \epsilon \tag{4.24}$$

where ϵ is a small parameter ($\epsilon \ll 1$). If $\epsilon = 0.01$, by using the definition of $\psi(\mathtt{Fr})$ (2.25) with $A_g = 0.0001$ s^2/m, the plot of expression (4.24) is the red dashed line in Fig. 4.2a. This curve identifies the maximum acceleration coefficient $\mathtt{MF}$ that preserves a linear morphodynamic acceleration for a given $\mathtt{Fr}$. Therefore the area below the curve represents the whole range of validity of the decoupled approximation. It allows that for small $\mathtt{Fr}$ number the acceleration coefficient is very large but rapidly decreases with increasing $\mathtt{Fr}$.

It is also worth noting that, for this particular example with simplified eigenvalues, the acceleration factor is smaller than unity for $\mathtt{Fr} \gtrsim 0.6$: this means that the decoupled approximation holds only with a deceleration ($\mathtt{MF} < 1$) of the system. Hence, this represents the value beyond which use of the MORFAC approach becomes counterproductive.

It is important to underline that the function $\psi(\mathtt{Fr})$ (thin black line in Fig. 4.2a)

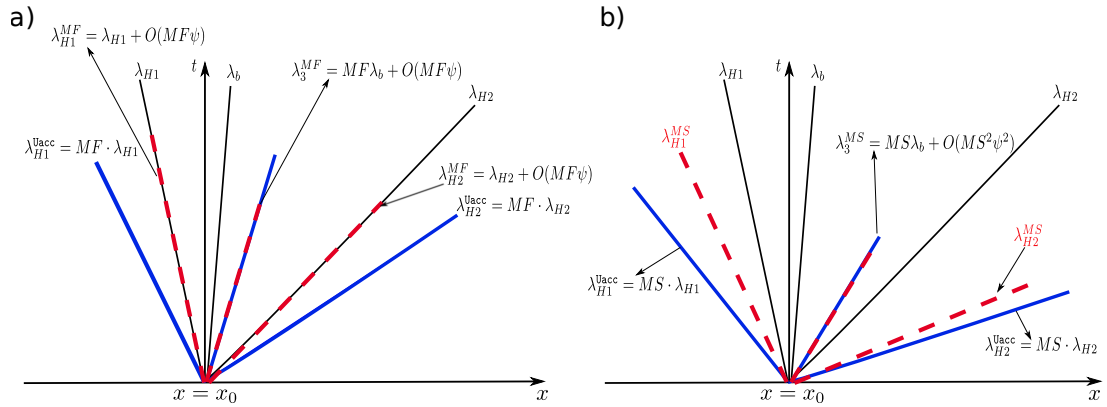

Figure 4.3: Representation of linearised characteristic curves in the phase space for: original system (black thin lines); uniformly accelerated `Uacc` system (blue thick lines); MORFAC approach (red dashed lines, panel a); MASSPEED approach (red dashed lines, panel b). According to the results given in Fig. 4.2 `MS` is always larger than `MF`.

is monotonically increasing but this strongly depends on the chosen transport closure formula (e.g. Eq. 2.25).

For the sake of generality, in Fig. 4.2b also the validity range when considering a constant value of $\psi = 10^{-4}$ is presented. Therefore all the subsequent considerations hold both for $\psi(\mathtt{Fr})$ or $\psi = const$.

If condition (4.24) holds, in agreement with Li [35], the MORFAC approach does not accelerate hydrodynamics since $\lambda_{1,2}^{\mathtt{MF}} \approx \lambda_{1,2}$ while the bed evolution is linearly accelerated by a factor `MF`, i.e. $\lambda_3^{\mathtt{MF}} = \mathtt{MF}\lambda_3 + O(\mathtt{MF}\psi)$. The corresponding situation in the phase space is depicted in Fig. 4.3a.

Substituting (4.21) and (4.22) into definition (4.18), for a given and constant `Fr`, the expected computational speed-up of the MORFAC method is

$$\mathtt{Sp}_{\mathtt{MF}} = \frac{\lambda_3^{\mathtt{MF}}}{\lambda_3} \cdot \frac{\lambda_2}{\lambda_2^{\mathtt{MF}}} \approx \mathtt{MF} \cdot 1 = \mathtt{MF} \, . \tag{4.25}$$

4.3.2 The MASSPEED approach

The MASSPEED (`MS`) approach is derived from Eq. (4.17): if $\mathtt{M}_{\mathrm{cw}} = \mathtt{M}_{\mathrm{cs}} = \mathtt{MS}$, the eigenvalue associated to the bed evolution $\lambda_3^{\mathtt{MS}}$ scales linearly, up to $O(\psi^2)$, with its analogous in the original system (2.30), and the scale factor is `MS`, thus $\lambda_3^{\mathtt{MS}} = \mathtt{MS}\lambda_3 + O(\psi^2)$.

This suggests that, if the sediment continuity equation (Exner equation) is accelerated by a factor $\mathtt{M}_{\mathrm{cs}}$, an identical acceleration must be imposed on the water continuity equation.

If $\mathtt{M}_{\mathrm{cw}} = \mathtt{M}_{\mathrm{cs}}$ in Eqs. (4.17) and (4.16), considering the higher order terms, the condition of weak interaction between bed and hydrodynamics, $\lambda_3^{\mathtt{MS}} \ll \lambda_2^{\mathtt{MS}}$, is satisfied

provided that

$$R\left[\frac{\mathtt{Fr}}{1-\mathtt{Fr}^2}\right]\psi \ll \left[\mathtt{Fr}+\sqrt{\mathtt{Fr}^2+R\,(1-\mathtt{Fr}^2)}\right] \quad \text{with} \quad R=\frac{\mathtt{M}_{\mathrm{cw}}}{\mathtt{M}_{\mathrm{q}}}=\frac{\mathtt{M}_{\mathrm{cs}}}{\mathtt{M}_{\mathrm{q}}}=\frac{\mathtt{MS}}{\mathtt{M}_{\mathrm{q}}}\,. \tag{4.26}$$

For $\mathtt{Fr}$ numbers typical of environmental flows, far enough below unity, the term on the left of the inequality (4.26) is of order $O(R\psi)$, while the term on the right side is of order $O(R^{1/2})$. Therefore, the analysis of condition (4.26) implies it to be satisfied if

$$R\psi^2=\epsilon\,, \quad \text{with} \quad \epsilon \ll 1\,. \tag{4.27}$$

This condition can be transformed on a constraint on $\mathtt{MS}$ if a given value is assigned to $\mathtt{M}_{\mathrm{q}}$. Setting $\mathtt{M}_{\mathrm{q}}=1$ for simplicity, the MASSPEED approach is introduced by the following choice for the acceleration coefficients: $\mathtt{M}_{\mathrm{cw}}=\mathtt{M}_{\mathrm{cs}}=\mathtt{MS}>1$, $\mathtt{M}_{\mathrm{q}}=1$.

Inserting these values into (4.16) and (4.17) gives

$$\frac{\lambda_{1,2}^{\mathtt{MS}}}{c}=\left[\mathtt{Fr}\mp\sqrt{\mathtt{Fr}^2+\mathtt{MS}\,(1-\mathtt{Fr}^2)}\right]+O(\mathtt{MS}\,\psi)\,, \tag{4.28}$$

$$\frac{\lambda_{3}^{\mathtt{MS}}}{c}=\mathtt{MS}\left[\left(\frac{\mathtt{Fr}}{1-\mathtt{Fr}^2}\right)\psi-\left(\frac{\mathtt{Fr}\,(\mathtt{Fr}^2+1)}{(1-\mathtt{Fr}^2)^3}\right)\psi^2\right]\,. \tag{4.29}$$

According to relation (4.27), the condition for the validity of the decoupled approach assumption is satisfied provided that

$$\mathtt{MS}\psi^2=\epsilon\ \text{, with}\ \epsilon \ll 1\,. \tag{4.30}$$

This range is larger than the analogous range (4.24), valid for the MORFAC approach. The situation is displayed in Fig. 4.2, where the blue dash-dotted line is obtained by setting $\epsilon=0.01$ in both panels. The result is that for all the range of $\mathtt{Fr}$, the MASSPEED allows for larger values of the acceleration coefficient than those given by the MORFAC approach. The areas below these lines represent the range of validity of the decoupled approximation.

Different from the MORFAC approach, the MASSPEED acceleration modifies also the characteristics of hydrodynamics, i.e. $|\lambda_{1,2}^{\mathtt{MS}}|>|\lambda_{1,2}|$ (compare Figures 4.3a and 4.3b). In particular, according to (4.18), $\mathtt{R}_{\mathtt{H}}=\lambda_2^{\mathtt{MS}}/\lambda_2>1$ hence the theoretical speed-up is bounded as follows:

$$1<\mathtt{Sp}_{\mathtt{MS}}=\frac{\mathtt{R}_{\mathtt{M}}}{\mathtt{R}_{\mathtt{H}}}\approx\frac{\mathtt{MS}}{\mathtt{R}_{\mathtt{H}}}<\mathtt{MS}. \tag{4.31}$$

This may wrongly suggest that the MORFAC gives a larger speed-up than MASSPEED, while it is true that the MASSPEED approach allows for much larger

values of $\mathtt{M}_{cs}$ which compensates by far the reduction of the integration time-step due to the acceleration of the hydrodynamic characteristic $\lambda_2^{\mathtt{MS}}$.

Since $\lambda_3^{\mathtt{MS}}$ is increased by the rate of $\mathtt{R_M}$ and $\lambda_2^{\mathtt{MS}}$ by the rate $\mathtt{R_H} < \mathtt{R_M}$, there is the risk that small morphodynamic disturbances may be accelerated so as to travel faster than the fastest hydrodynamic small disturbances, i.e. $\lambda_3^{\mathtt{MS}} \geq \lambda_2^{\mathtt{MS}}$. Therefore it sounds reasonable to impose a physical limit for the validity of the MASSPEED approach. The physical limit of such an acceleration is given by the fact that the bed wave perturbation associated to $\lambda_3^{\mathtt{MS}}$ should travel at a slower pace than the perturbation of the water surface associated to $\lambda_2^{\mathtt{MS}}$. Now, considering the approximation of $\lambda_2^{\mathtt{MS}}$, Eq. (4.28), at the leading order $O(\psi^0)$ and $\lambda_3^{\mathtt{MS}}$, Eq. (4.29), at $O(\psi)$, and imposing $\lambda_2^{\mathtt{MS}} = \lambda_3^{\mathtt{MS}}$, the following limit relation is obtained:

$$\mathtt{MS}^{\max} = -\frac{(\mathtt{Fr}^6 + 2\mathtt{Fr}^4\psi - 3\mathtt{Fr}^4 - 2\mathtt{Fr}^2\psi + 3\mathtt{Fr}^2 - 1)}{\mathtt{Fr}^2\psi^2}, \tag{4.32}$$

which gives the maximum factor $\mathtt{MS}^{\max}$ that can be used to avoid this unphysical behaviour. Accelerating the system by a factor $\mathtt{MS} < \mathtt{MS}^{\max}$ avoids the loss of the strict hyperbolicity, which occurs when two eigenvalues coalesce [18, 61]. This particular mathematical condition must be avoided because may give rise to resonance and loss of solution uniqueness. Theoretical issues regarding resonance are found in the classical papers [30, 37] and references therein.

In Fig. 4.2 the condition of the physical validity of (4.32) is plotted as a function of the Froude number. It is seen that for $\epsilon = 0.01$ the range of validity for the decoupled solution is contained within the limit of physical validity for all $\mathtt{Fr}$ values.

Finally, substitution of Eq. (4.32) in the definition of the maximum speed-up gives

$$\mathtt{Sp}_{\mathtt{MS}}^{\max} = \mathtt{MS}^{\max}\frac{1 + \dfrac{1}{\mathtt{Fr}}}{1 + \sqrt{1 + \mathtt{MS}^{\max}\left(\dfrac{1}{\mathtt{Fr}^2} - 1\right)}}. \tag{4.33}$$

Relation (4.33) is plotted in Fig. 4.4 with the black solid curve, by setting $A_g = 0.0001$ into the definition of ψ (2.25). Moreover, the dashed line is obtained by setting the constant $\psi = 10^{-4}$ in (4.33). It is observed that the speed-up is of order 10^2 for small Froude numbers and decreases rapidly to unity as $\mathtt{Fr} \to 1$.

4.3.3 Why linear acceleration is necessary to predict bed shapes

Latter sections are focused on the study of the linear scaling of the third eigenvalue of the accelerate dSVE mathematical model. As seen in §2.3, if morphodynamics and hydrodynamics are weakly coupled the third eigenvalue is strictly relate to the time scale of bed shape evolution. However, a correct time representation of the phenomenon is not enough if the correct shape of the riverbed is not preserved.

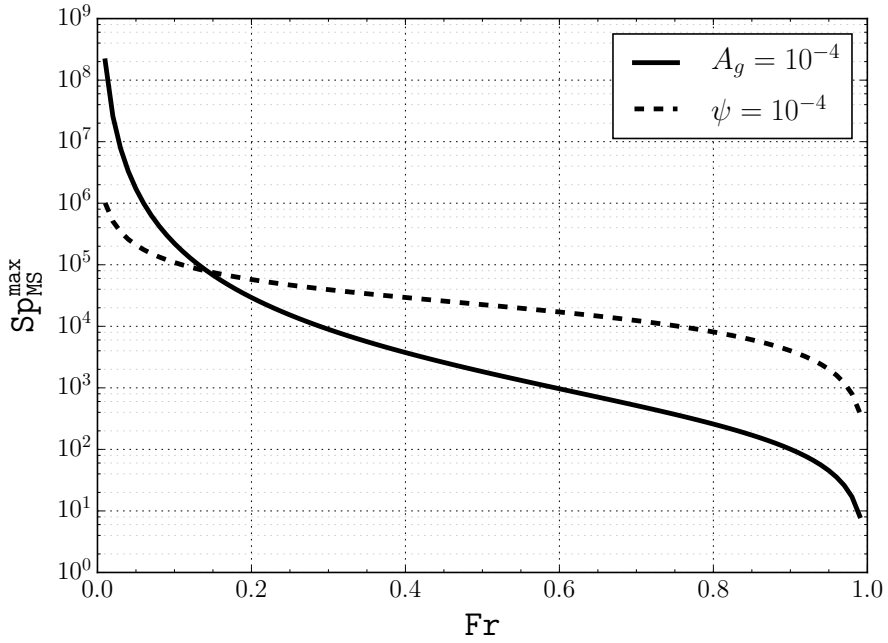

Figure 4.4: MASSSPEED approach: maximum theoretical speed-up $\mathtt{Sp}_{\mathtt{MS}}^{\mathtt{max}}$ (Eq. 4.33) obtained from the approximate solution of the eigenvalues. The full line is obtained by using the definition of ψ as in Eq. (2.25) and setting $A_g = 0.0001$ in the sediment transport closure (2.5). The dotted line is obtained by setting $\psi = 10^{-4}$.

To study the effect of accelerations techniques on the bed topography prediction a near-equilibrium linearized example, similar to that illustrated in §2.3.1, is now considered.

The resulting *accelerated-linearized* system is

$$\frac{\partial \boldsymbol{W}}{\partial t} + \boldsymbol{\mathcal{M}}\,\boldsymbol{\mathcal{A}}_{\mathtt{L}} \frac{\partial \boldsymbol{W}}{\partial x} = 0\,, \tag{4.34}$$

with

$$\boldsymbol{\mathcal{A}}_{\mathtt{L}} = \begin{bmatrix} 0 & 1 & 0 \\ c_{\mathtt{L}}^2 - u_{\mathtt{L}}^2 & 2u_{\mathtt{L}} & c_{\mathtt{L}}^2 \\ -u_{\mathtt{L}}\,\psi_{\mathtt{L}} & \psi_{\mathtt{L}} & 0 \end{bmatrix} \qquad \boldsymbol{\mathcal{M}} = \begin{bmatrix} \mathtt{M}_{\mathtt{cw}} & 0 & 0 \\ 0 & \mathtt{M}_{\mathtt{q}} & 0 \\ 0 & 0 & \mathtt{M}_{\mathtt{cs}} \end{bmatrix}. \tag{4.35}$$

The *linearized* system (2.34) is obtained when $\mathtt{M}_{\mathtt{cw}} = \mathtt{M}_{\mathtt{q}} = \mathtt{M}_{\mathtt{cs}} = 1$; while the MORFAC and the MASSPEED systems ere obtained with $\mathtt{M}_{\mathtt{cw}} = \mathtt{M}_{\mathtt{q}} = 1$, $\mathtt{M}_{\mathtt{cs}} = \mathtt{MF}$ and $\mathtt{M}_{\mathtt{cw}} = \mathtt{M}_{\mathtt{cs}} = \mathtt{MS}$, $\mathtt{M}_{\mathtt{q}} = 1$, respectively.

In Eq. (4.35), subscript $\mathtt{L}$ refers to the reference state: $u_{\mathtt{L}} = q_{\mathtt{L}}/h_{\mathtt{L}}$ is the reference flow velocity; $c_{\mathtt{L}} = \sqrt{g\,h_{\mathtt{L}}}$ is the celerity of gravitational waves; $\psi_{\mathtt{L}} = \psi|_{\boldsymbol{W}_{\mathtt{L}}} = 3\,g\,\xi\,A_g\,\mathtt{Fr}_{\mathtt{L}}^2$ is the reference sediment transport parameter; $\mathtt{Fr}_{\mathtt{L}} = u_{\mathtt{L}}/c_{\mathtt{L}}$ is the reference Froude number.

Applying the characteristic method as described in §2.3.1 (here reproduced for the *accelerated-linearized* dSVE problem), system (4.34) can be analytically solved, both in MORFAC and MASSPEED configurations. Thus, the conservative accelerated variables $\boldsymbol{W}^{\mathtt{NUacc}}(x)$ can be projected on the *accelerated characteristic space* multiplying them by the inverse of the matrix of the right eigenvectors of $[\boldsymbol{\mathcal{MA}}_{\mathtt{L}}]$,

$$\boldsymbol{U}(x) = \boldsymbol{L}_{\mathtt{L}}^{\mathtt{NUacc}}\, \boldsymbol{W}^{\mathtt{NUacc}}(x)\,, \tag{4.36}$$

with $\boldsymbol{U}(x)$ the vector of the characteristic variables and $\boldsymbol{L}_{\mathtt{L}}^{\mathtt{NUacc}}$ the inverse of the matrix of the right eigenvectors (4.13) computed for the unperturbed state.

Each characteristic variable $\boldsymbol{U}^{(j)}$ satisfies an *accelerated linear advection equation* with a celerity given by the corresponding constant *accelerated eigenvalue*, $\lambda_j^{\mathtt{NUacc}}$ (4.8), i.e.,

$$\frac{\partial \boldsymbol{U}^{(j)}}{\partial t^{\mathtt{NUacc}}} + \lambda_j^{\mathtt{NUacc}} \frac{\partial \boldsymbol{U}^{(j)}}{\partial x} = 0 \quad \text{for} \quad j = 1,\, 2,\, 3\,. \tag{4.37}$$

in which $t^{\mathtt{NUacc}}$ is the *scaled propagation time*.

As shortly described in §4.2.1 for the case of uniform acceleration, the introduction of this scaled time is mandatory to build a link between different time scales. In fact, the acceleration of the bottom evolution corresponds to a modification of the time scale in the *accelerated characteristic space*. In particular, the time needed into this accelerated space to produce the desired evolution is smaller, proportionally to the acceleration imposed. If the acceleration of the bed evolution is supposed to be proportional to $\mathtt{M}_{\mathrm{cs}}$ (the acceleration coefficient of the Exner equation), in the accelerated space the *local time* $t^{\mathtt{NUacc}}$ would be $\mathtt{M}_{\mathrm{cs}}$ times faster, and the definition of $t^{\mathtt{NUacc}}$ becomes:

$$t = \mathtt{M}_{\mathrm{cs}}\, t^{\mathtt{NUacc}} \qquad \Rightarrow \qquad t^{\mathtt{NUacc}} = \frac{t}{\mathtt{M}_{\mathrm{cs}}} \tag{4.38}$$

Thus, the corresponding solution in terms of $\boldsymbol{U}$, for a given propagation time $t_p = \mathtt{M}_{\mathrm{cs}}\, t_p^{\mathtt{NUacc}}$ is

$$\boldsymbol{U}^{(j)}(x, t_p^{\mathtt{NUacc}}) = \boldsymbol{U}_0^{(j)}(x - \lambda_j^{\mathtt{NUacc}}\, t_p^{\mathtt{NUacc}}) \quad \text{for} \quad j = 1,\, 2,\, 3\,. \tag{4.39}$$

The evolved conservative accelerated variables $\boldsymbol{W}^{\mathtt{NUacc}}(x, t_p^{\mathtt{NUacc}})$ can be found by multiplying $\boldsymbol{U}(x, t_p^{\mathtt{NUacc}})$ by the matrix of the *accelerated right eigenvectors* $\mathbf{R}_{\mathtt{L}}^{\mathtt{NUacc}}$ (4.12),

$$\boldsymbol{W}^{\mathtt{NUacc}}(x, t_p^{\mathtt{NUacc}}) = \mathbf{R}_{\mathtt{L}}^{\mathtt{NUacc}}\, \boldsymbol{U}(x, t_p^{\mathtt{NUacc}}). \tag{4.40}$$

Focusing the attention on the *accelerated bottom evolution*, indicating with $\mathbf{r}_j^{\mathtt{NUacc}(3)}$ the third component of the j-th *accelerated eigenvector* of $[\boldsymbol{\mathcal{MA}}_{\mathtt{L}}]$, the third equation of the system (2.39) can be written as

$$z^{\mathtt{NUacc}}(x, t_p^{\mathtt{NUacc}}) = \sum_{j=1}^{3} \mathbf{r}_j^{\mathtt{NUacc}(3)}\, \boldsymbol{U}^{(j)}(x, t_p^{\mathtt{NUacc}}) = \sum_{j=1}^{3} \zeta_j^{\mathtt{NUacc}}(x, t_p^{\mathtt{NUacc}})\,, \tag{4.41}$$

where $\zeta_j^{\texttt{NUacc}}(x, t_p^{\texttt{NUacc}}) = \mathbf{r}_j^{\texttt{NUacc}(3)}\, \boldsymbol{U}^{(j)}(x, t_p^{\texttt{NUacc}})$ represents the contribution of each component of the characteristic variables to the bottom evolution.

Assuming valid the hypothesis of weak coupling between hydrodynamic and morphodynamic, Eqs. (4.39) and (4.41) give two restraints that must be satisfied to have a bed evolution properly accelerated:

i) Eqs. (4.38) and (4.39) require

$$\lambda_3^{\texttt{NUacc}}\, t_p^{\texttt{NUacc}} = \lambda_3\, t_p \quad \Rightarrow \quad \frac{\lambda_3^{\texttt{NUacc}}}{\texttt{M}_{\text{cs}}} = \lambda_3\,; \tag{4.42}$$

ii) Eq. (4.41), which reduces to $z^{\texttt{NUacc}}(x, t_p^{\texttt{NUacc}}) = \zeta_3^{\texttt{NUacc}}(x, t_p^{\texttt{NUacc}})$, impose that

$$z^{\texttt{NUacc}}(x, t_p^{\texttt{NUacc}}) = \zeta_3^{\texttt{NUacc}}(x, t_p^{\texttt{NUacc}}) = \zeta_3(x, t_p) = z; (x, t_p) \tag{4.43}$$

If MORFAC and MASSPEED accelerations are applied, the first restraint returns the already discussed hypothesis of linear morphological response to hydrodynamic forcing. Thus, by substituting the scaled propagation times $t_p^{\texttt{MF}} = t_p/\texttt{MF}$ and $t_p^{\texttt{MS}} = t_p/\texttt{MS}$ in Eq. (4.42), it becomes:

$$\lambda_3^{\texttt{MF}}\, \frac{t_p}{\texttt{MF}} = \lambda_3^{\texttt{MS}}\, \frac{t_p}{\texttt{MS}} = \lambda_3\, t_p \quad \Rightarrow \quad \frac{\lambda_3^{\texttt{MF}}}{\texttt{MF}} = \frac{\lambda_3^{\texttt{MS}}}{\texttt{MS}} = \lambda_3\,. \tag{4.44}$$

To answer to the research question of this section the second restraint must be considered. Applying MORFAC and MASSPEED, Eq. (4.43) imposes that

$$\zeta_3^{\texttt{MF}}(x, t_p^{\texttt{MF}}) = \zeta_3^{\texttt{MS}}(x, t_p^{\texttt{MS}}) = \zeta_3(x, t_p) = z(x, t_p), \tag{4.45}$$

Indeed, according to Eq. (4.36) and (4.41), $z(x, t_p)$ is related to both $\mathbf{r}_3^{(3)}$ and $\mathbf{l}_3^{(3)}$, so to preserve the evolved bed shape any acceleration strategy must not alter these two quantities.

Given the complexities in the analytical formulation of $\mathbf{l}_i$ (4.14), only $\mathbf{r}_3^{(3)}$ is here analytically studied, then a graphical example is used to facilitate the comprehension.

Introducing the parameter ψ (2.25) into the formulation of analytical accelerated eigenvectors (4.12), the component $\mathbf{r}_3^{\texttt{NUacc}(3)}$ can be written as

$$\mathbf{r}_3^{\texttt{NUacc}(3)} = \psi\, \frac{\texttt{M}_{\text{cs}}}{\texttt{M}_{\text{cw}}} \left(1 - \frac{u\, \texttt{M}_{\text{cw}}}{\lambda_3}\right), \tag{4.46}$$

which, neglecting the superscript `NUacc` to simplify the notation, becomes

$$\mathbf{r}_3^{(3)}\,|_{\texttt{OS}} = \psi \left(1 - \frac{u}{\lambda_3}\right), \qquad \text{for the } \textit{original system}, \tag{4.47}$$

$$\mathbf{r}_3^{(3)}\,|_{\texttt{MF}} = \psi\, \texttt{MF} \left(1 - \frac{u}{\lambda_3^{\texttt{MF}}}\right), \qquad \text{for the MORFAC system}, \tag{4.48}$$

$$\mathbf{r}_3^{(3)}\,|_{\texttt{MS}} = \psi \left(1 - \frac{u\, \texttt{MS}}{\lambda_3^{\texttt{MS}}}\right), \qquad \text{for the MASSPEED system}. \tag{4.49}$$

For the MASSPEED approach, looking at Eqs. (4.47) and (4.49), it is trivial to see that, if condition (4.44) is verified, then $\mathbf{r}_3^{(3)}|_{\mathtt{MS}} \approx \mathbf{r}_3^{(3)}|_{\mathtt{OS}}$.

Conversely, for the MORFAC approach, looking at Eqs. (4.47) and (4.48), condition (4.44) is no more sufficient to have $\mathbf{r}_3^{(3)}|_{\mathtt{MF}} \approx \mathbf{r}_3^{(3)}|_{\mathtt{OS}}$. Due to the lack of acceleration of the hydrodynamic continuity equation, MORFAC approximates $\mathbf{r}_3^{(3)}$ well only if $\mathtt{MF} \approx 1$.

To better quantify the differences between MASSPEED and MORFAC the acceleration $\mathtt{MF} = \mathtt{MS} = 5$ is now considered as an example. If $\psi = 0.01$ is fixed, accelerated eigenvalues (4.8) and eigenvectors components (4.12) & (4.14) result in functions only of $\mathtt{Fr}$ and they can be easily plotted.

Fig. 4.5 shows, for $0 < \mathtt{Fr} < 0.95$, the comparison between the third eigenvalues scaled as in Eq. (4.44) and the corresponding component of $\mathbf{R}$ and $\boldsymbol{L}$. According to Fig. 4.5a, assuming as reference the original system, the MASSPEED gives a better approximation of the third eigenvalue, specially for $\mathtt{Fr} > 0.6$. As expected from Eqs. (4.48) and (4.49), respect to the MORFAC approach, the MASSPEED leads also to a much better approximation of $\mathbf{r}_3^{(3)}$ (Fig. 4.5b) and $\mathbf{l}_3^{(3)}$ (Fig. 4.5c) . Thus, the improvement obtained by using the MASSPEED approach is clear and the respect of the linear morphodynamic response hypothesis is crucial to preserve the correct shape of the evolving riverbed.

4.4 Non-linear numerical strategies to compute the maximum acceleration factors

In the previous section the maximum accelerations allowed with MORFAC and MASSPEED approaches have been introduced thanks to a linear approximation of the system eigenvalues (see §4.2.4). The goal of this section is to define a more general criterion for the determination of the maximum acceleration factors by considering the fully nonlinear expression of the three eigenvalues as described in §4.2.3. Thus, a new strategy to dynamically recompute the maximum acceleration factors during a numerical simulation is proposed. If not differently specified, an acceleration factor $\mathtt{M}_{\mathrm{cs}} = 10$ is considered, while the solid transport discharge is computed according to Grass (2.5) with $A_g = 0.005$.

4.4.1 Non-linear estimation of the maximum acceleration factors

First the MORFAC approach is considered. The roots associated with the flux matrix $\boldsymbol{\mathcal{M}}\boldsymbol{\mathcal{A}}$ in Eq. (4.1) can be computed by solving the cubic characteristic polynomial (4.7) after setting the acceleration factors equal to $\mathtt{M}_{\mathrm{cw}} = \mathtt{M}_{\mathrm{q}} = 1$ and $\mathtt{M}_{\mathrm{cs}} = \mathtt{MF} = 10$, in this example. The MORFAC approach successfully establishes a well defined correspondence between the original and the accelerated model only if morphodynamics evolves linearly in time. More precisely, under the hypothesis

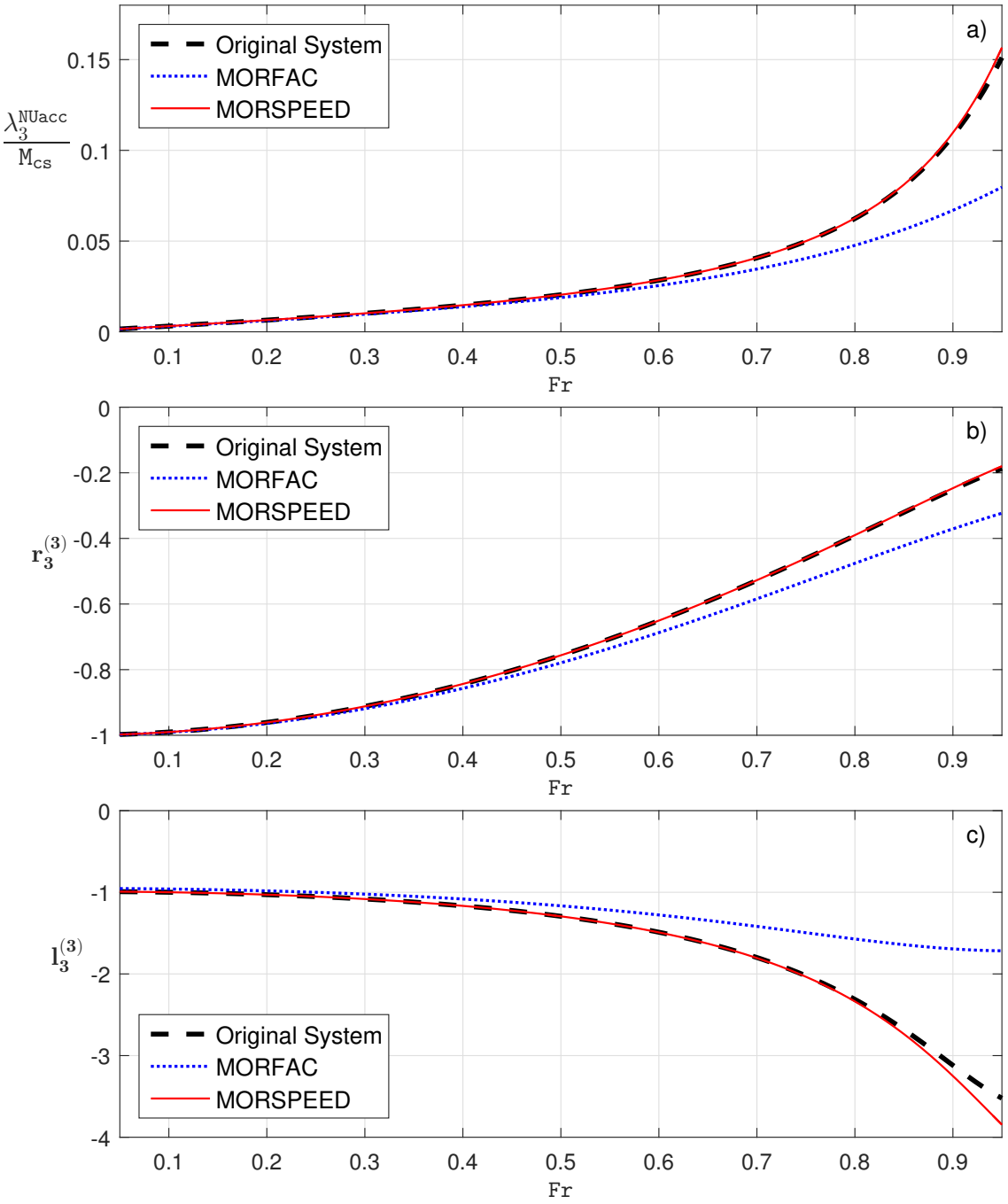

Figure 4.5: Comparison between eigenstructure components for $0 < \mathtt{Fr} < 0.95$, $\psi = 0.01$ and $\mathtt{MF} = \mathtt{MS} = 5$: a) acceleration of the third eigenvalue according to Eq. (4.42); b) $\mathbf{r}_3^{(3)}$ according to the original system, the MORFAC system and the MASSPEED system, Eqs. (4.47 - 4.49); c) $\mathbf{l}_3^{(3)}$ according to the original system, the MORFAC system and the MASSPEED system.

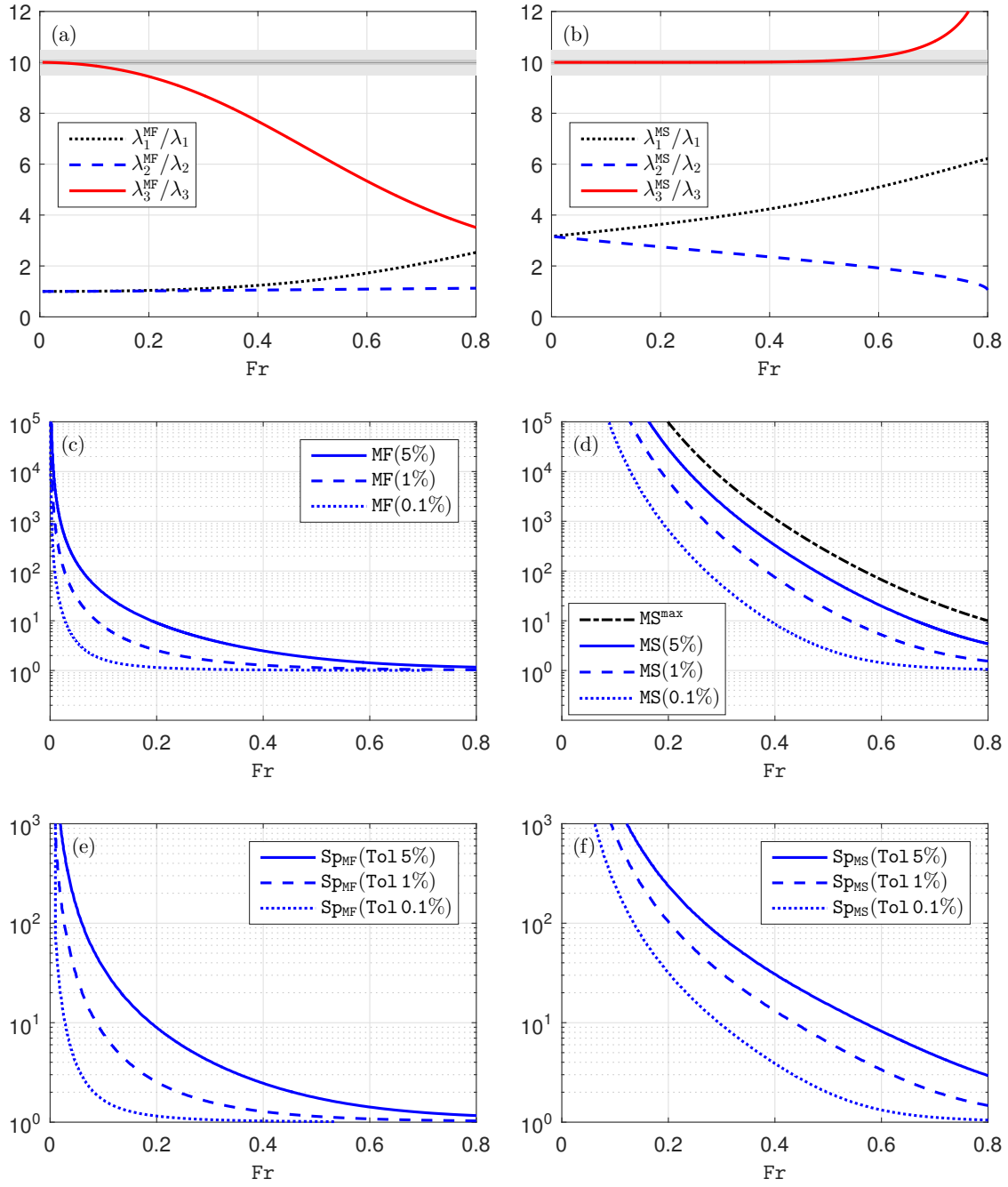

Figure 4.6: Panel a and b: Ratios of nonlinear eigenvalues $\frac{\lambda_{MFi}(Fr,MF,\psi)}{\lambda_i(Fr,\psi)}$. The grey-shaded areas represents the tolerance band Tol in Eq. (4.51). Panels c and d: maximum acceleration factor for given values of tolerance. Panels e and f: maximum expected speed-up. In the left and right panels the results for the MORFAC and MASSPEED approaches are collected.

of weak interaction between hydrodynamics and morphodynamics, the following relation must hold:

$$\mathtt{R_M} = \frac{\lambda_3^{\mathtt{MF}}(\mathtt{Fr}, \mathtt{MF}, \psi)}{\lambda_3(\mathtt{Fr}, \psi)} \approx \mathtt{MF}, \tag{4.50}$$

where $\lambda_3^{\mathtt{MF}}$ and λ_3 are computed according to Eq. (4.8c), and λ_3 is the smallest eigenvalue of the original system ($\mathtt{M_{cw}} = \mathtt{M_q} = \mathtt{M_{cs}} = 1$). Hence, the more $\mathtt{R_M}$ deviates from the assigned MF, the weaker the assumption of linear acceleration is. The maximum acceptable deviation is quantified introducing a tolerance band ($\pm$Tol), therefore condition (4.50) can be rewritten as

$$\mathtt{R_M} = \frac{\lambda_3^{\mathtt{MF}}(\mathtt{Fr}, \mathtt{MF}, \psi)}{\lambda_3(\mathtt{Fr}, \psi)} = \mathtt{MF}\,(1 \pm \mathtt{Tol})\,. \tag{4.51}$$

Relation (4.51) is an implicit expression of MF that depends on the water flow (Fr) and sediment transport (ψ). Hence, for a user-given tolerance (Tol), the maximum value of MF, which assures that the bed evolves linearly, is numerically computed from Eq. (4.51). In Figure 4.6a, the ratios $\frac{\lambda_i^{\mathtt{MF}}(\mathtt{Fr},\mathtt{MF},\psi)}{\lambda_i(\mathtt{Fr},\psi)}$ are displayed by using different style-lines. The ratio $\lambda_3^{\mathtt{MF}}/\lambda_3$ (red solid line), tends asymptotically to the assigned MF as $\mathtt{Fr} \to 0$. On the other hand, for increasing values of Fr the ratio rapidly decays below $\mathtt{MF} = 10$. The linear assumption holds as long as the red curve lays inside the grey-shaded areas, corresponding to the right-hand-side of (4.51): the thinner and the darker the gray stripe is the smaller is the tolerance, $\mathtt{Tol} = 5\%, 1\%, 0.1\%$ in this case.

In Fig. 4.6c the maximum acceleration factor MF, computed with (4.51), is plotted against Fr. The three different lines are obtained by considering three different small tolerance values, namely $\mathtt{Tol} = 5\%, 1\%, 0.1\%$. The acceleration coefficient MF shows an inverse exponential dependency on Fr. This is in agreement with the empirical results obtained by Ranasinghe *et al.* [51] and Li [35]. It is also seen that the magnitude of the maximum acceleration factor crucially depends on the user-given tolerance.

Finally, for each value MF, the expected numerical speed-up $\mathtt{Sp_{MF}}$ (4.18) is plotted against Fr in Fig. 4.6e. As expected, the speed-up is decreasing rapidly for increasing values of Fr. For example, if $\mathtt{Fr} = 0.1$ and the tolerance is set to 1%, the maximum achievable speed-up is about 10; while if the tolerance is increased up to 5% the corresponding speed-up increases up to about 100.

The very same analysis can be extended to the MASSPEED approach, providing $\mathtt{M_q} = 1$ and $\mathtt{M_{cw}} = \mathtt{M_{cs}} = \mathtt{MS}$ in the governing system (4.1). The maximum MASSPEED factor MS for given Fr, ψ and tolerance Tol is analogous to (4.51) and reads

$$\mathtt{R_M} = \frac{\lambda_3^{\mathtt{MS}}(\mathtt{Fr}, \mathtt{MS}, \psi)}{\lambda_3(\mathtt{Fr}, \psi)} = \mathtt{MS}\,(1 \pm \mathtt{Tol})\,. \tag{4.52}$$

It is interesting to note that, consistently with the results obtained with approximated solutions in §4.3, the range of $\mathtt{Fr}$ numbers for which the ratio $\lambda_3^{\mathtt{MS}}/\lambda_3 \simeq \mathtt{MS}$ (range of linearity), is broader for the MASSPEED when compared with the MORFAC approach. Comparing Fig. 4.6a and Fig. 4.6b, the linear range extends up to $\mathtt{Fr} \approx 0.6$ (panel b) for the MORSPEED, while it reduces to $\mathtt{Fr} \approx 0.15$ for the MORFAC (panel a). Within the linear range, the MASSPEED approach shows also higher values of the maximum acceleration (Fig. 4.6c versus 4.6d) and larger speed-up (Fig. 4.6e versus 4.6f). For example, given a tolerance of 1% and $\mathtt{Fr} = 0.4$, the maximum $\mathtt{MS}$ corresponds to 75 (Fig. 4.6d) resulting in a speed-up of about 13 (Fig. 4.6e) while application of the MORFAC approach does not result in any acceleration.

Finally, concerning the loss of hyperbolicity mentioned in §4.3.2, as in Eq. (4.32) the value $\mathtt{MS}^{\max}$ is now numerically computed by imposing that $\lambda_2^{\mathtt{MS}} = \lambda_3^{\mathtt{MS}}$, but making use of the exact expression of the eigenvalues, (4.8b) and (4.8c). $\mathtt{MS}^{\max}$ is plotted against the $\mathtt{Fr}$ number in Fig. 4.6d (black dashed line). It is worth noting that the loss of hyperbolicity occurs outside the domain of linear acceleration, i.e. $\mathtt{MS}^{\max} > \mathtt{MS}(5\%)$.

4.4.2 Numerical evaluation of the highest acceleration factor: fixed and adaptive appraoch

A numerical strategy similar to the well-known Courant-Friedrichs-Lewy stability condition can be introduced to maximize the computational speed-up. Note that that the very same procedure can be implemented for the MORFAC approach, but here it is only described for the MASSPEED approach for the sake of brevity.

If a physical domain of length L discretized with a finite set of points or volumes is considered, at a given time, within a single numerical time step Δt, local flow ($\mathtt{Fr}_i$) and sediment transport (ψ_i) conditions are assigned. Therefore the calculation for each cell i of the eigenvalues $\lambda_{j,i}^{\mathtt{MS}}$ and $\lambda_{j,i}$ (with $j = 1, 2, 3$) is possible by using Eqs. (4.8). Then, for a given tolerance value $\mathtt{Tol}$ (prescribed by the user), application of relation (4.52) gives the value of the maximum accelerator factor $\mathtt{MS}_i$ for each cell i at a given time. Now, two possible approaches are introduced here: fixed and adaptive. In the fixed approach, the maximum acceleration factor $\mathtt{MS}$ is computed at the beginning of the simulation as $\mathtt{MS} = \min_i [\mathtt{MS}_i]$ and kept constant for all time steps of the simulation, until the final time is reached. In the adaptive approach the maximum acceleration factor is a function of time, i.e. $\mathtt{MS}_i(\tau)$, and is computed for each time step according to the local flow and sediment transport conditions. Then, for the generic time τ, the adaptive $\mathtt{MS}(\tau) = \min_i [\mathtt{MS}_i(\tau)]$ is computed solving the following equation for each cell i:

$$\frac{\lambda_{3,i}^{\mathtt{MS}}\Big(\mathtt{Fr}_i(\tau), \psi_i(\tau), \mathtt{MS}_i(\tau)\Big)}{\lambda_{3,i}\Big(\mathtt{Fr}_i(\tau), \psi_i(\tau)\Big)} = (1 \pm \mathtt{Tol}) \cdot \mathtt{MS}_i(\tau)\,. \tag{4.53}$$

Eq. (4.53) is valid for any closure for the solid transport and can be solved via a numeric iterative method (e.g. standard regula falsi (RF) method [62]). Alternatively, to reduce the computational cost due to the iterative procedure, one can obtain $\mathtt{MS}_i(\tau)$ from the curves in Fig. 4.3.

4.5 Evolution of a sediment hump

The propagation of a sediment hump is considered in this section to assess and compare the accuracy and efficiency of MORFAC and MASSPEED. In all cases, the obtained solutions are compared with that obtained with the original model.

First, the linearized problem examined in §2.3.1 and §4.3.3 is solved with both MORFAC and MASSPEED, for the same given tolerance on the time upscaling. This problem must be considered as a *proof of concepts* of the developed theoretical backgound.

Second, the long-term evolution of a finite sediment hump is numerically solved by implementing the discussed acceleration techniques into the finite volume model described in Chapter 3.

The final goal is to assess the advantages of the new MASSPEED approach.

4.5.1 Linearized morphodynamic problem: accelerated evolution of a small sediment hump

The evolution of a small (infinitesimal) erodible hump due to a nearly uniform water flow in a straight channel is considered. Under these conditions, the problem can be studied within a linear framework, and an analytical solution can be derived [e.g. 39]. The nonlinear system (4.1) (the friction term is neglected) can be linearized respect to the uniform reference state $\boldsymbol{W}_{\mathtt{L}} = [h_{\mathtt{L}},\, q_{\mathtt{L}},\, z_{\mathtt{L}}]^T$, by *freezing* the entries of flux matrix (4.35).

The resulting *linearized system* (4.34) is here reported for readability, in which now $\mathtt{M}_{\mathtt{q}} = 1$ by default:

$$\frac{\partial \boldsymbol{W}}{\partial t} + \boldsymbol{\mathcal{M}}\,\boldsymbol{\mathcal{A}}_{\mathtt{L}}\frac{\partial \boldsymbol{W}}{\partial x} = 0\,, \tag{4.54}$$

with

$$\boldsymbol{\mathcal{A}}_{\mathtt{L}} = \begin{bmatrix} 0 & 1 & 0 \\ c_{\mathtt{L}}^2 - u_{\mathtt{L}}^2 & 2u_{\mathtt{L}} & c_{\mathtt{L}}^2 \\ -u_{\mathtt{L}}\,\psi_{\mathtt{L}} & \psi_{\mathtt{L}} & 0 \end{bmatrix} \qquad \boldsymbol{\mathcal{M}} = \begin{bmatrix} \mathtt{M}_{\mathtt{cw}} & 0 & 0 \\ 0 & 1 & 0 \\ 0 & 0 & \mathtt{M}_{\mathtt{cs}} \end{bmatrix}\,. \tag{4.55}$$

The original system is obtained when $\mathtt{M}_{\mathtt{cw}} = \mathtt{M}_{\mathtt{cs}} = 1$, the MORFAC system for $\mathtt{M}_{\mathtt{cw}} = 1$, $\mathtt{M}_{\mathtt{cs}} = \mathtt{MF}$ and the MASSPEED for $\mathtt{M}_{\mathtt{cw}} = \mathtt{M}_{\mathtt{cs}} = \mathtt{MS}$. As defined in §4.3.3, subscript $\mathtt{L}$ refers to the reference state and $u_{\mathtt{L}} = q_{\mathtt{L}}/h_{\mathtt{L}}$ and $c_{\mathtt{L}} = \sqrt{g\,h_{\mathtt{L}}}$ are the reference flow velocity and celerity, respectively. $\psi_{\mathtt{L}}$ is the reference sediment transport parameter, $\mathtt{Fr}_{\mathtt{L}} = u_{\mathtt{L}}/c_{\mathtt{L}}$ is the reference Froude number and $q_0 = q_{\mathtt{L}} = \sqrt{h_{\mathtt{L}}^3\, g\, \mathtt{Fr}_{\mathtt{L}}^2}$.

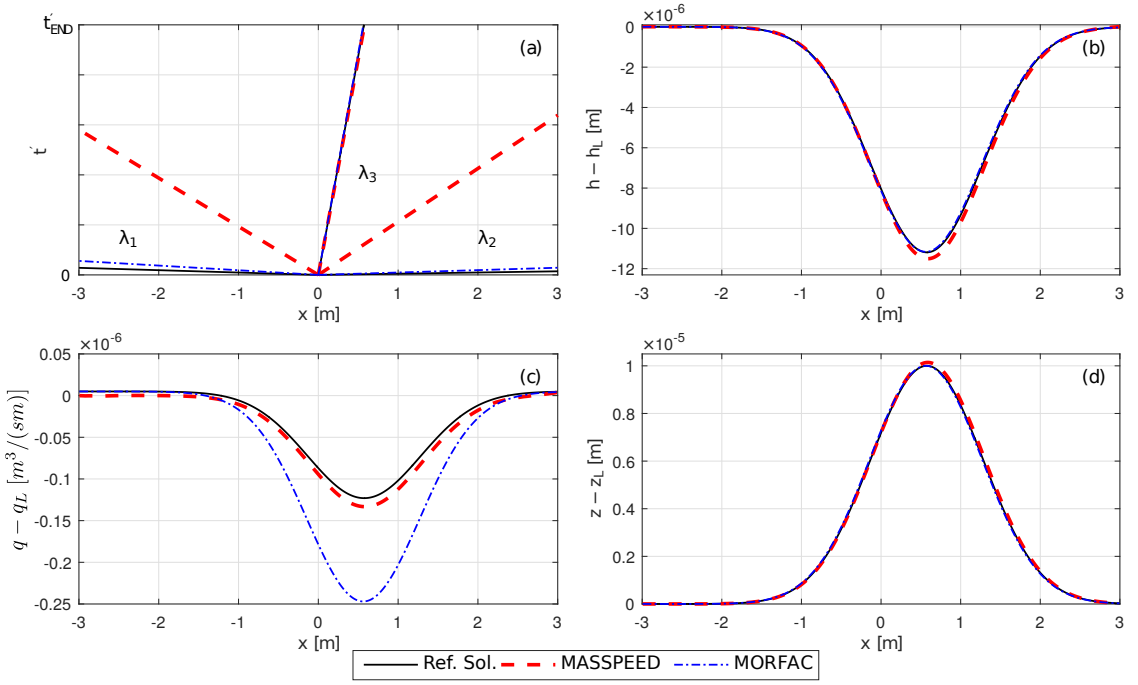

Figure 4.7: Linearized solution of the propagation of a sediment hump [39] using the linearized MORFAC and MASSPEED approaches: a) comparison between the characteristic lines (the time is properly scaled for the MORFAC and MASSPEED approaches); b) difference between the water depth and the unperturbed water depth; c) difference between the flow discharge and the unperturbed flow discharge; d) bottom elevation. The analytical solution of the linear original system is used as reference.

The initial conditions of the problem are given by $\boldsymbol{W}_0 = [h_0, q_0, z_0]^T$ with $z_0(x) = z_{\max}\exp(-x^2)$, $z_{\max} = 1.0^{-5}$ m and $h_0(x) = h_{\mathtt{L}} - z_0(x)$, given $h_{\mathtt{L}} = 1$ m. While the imposed sediment transport is $\psi_{\mathtt{L}} = 0.01$ which correspond $\mathtt{Fr}_{\mathtt{L}} = 0.33$.

The solution of system (4.54) can be obtained analytically as described in §4.3.3. The final time for which the solution is sought is $t_{\mathtt{END}} = 50$ s for the original system. Hence, according to Eq. (4.38), the corresponding final propagation time for the MORFAC and MASSPEED approaches are $t^{\mathtt{MF}}_{\mathtt{END}} = t_{\mathtt{END}}/\mathtt{MF}$ and $t^{\mathtt{MS}}_{\mathtt{END}} = t_{\mathtt{END}}/\mathtt{MS}$, respectively.

Setting a tolerance $\mathtt{Tol} = 1.36\%$, the resulting (rounded) maximum acceleration factors, calculated from Eqs. (4.51) and (4.52), are $\mathtt{MF} = 2$ and $\mathtt{MS} = 900$.

The analytical solutions are displayed in Fig. 4.7. In Fig. 4.7a the characteristic lines in the phase space $x - t'$ are given, where t' stands for t the time in the original system, $t/\mathtt{MF}$ and $t/\mathtt{MS}$, the times in the MORFAC and MASSPEED systems. Deviations of the water depth, discharge and bed elevation, to their unperturbed initial values h_L, q_L and z_L are given in Fig. 4.7b, Fig. 4.7c and Fig. 4.7d, respectively.

It is seen in the phase space plots, the three eigenvalues with the propagation of

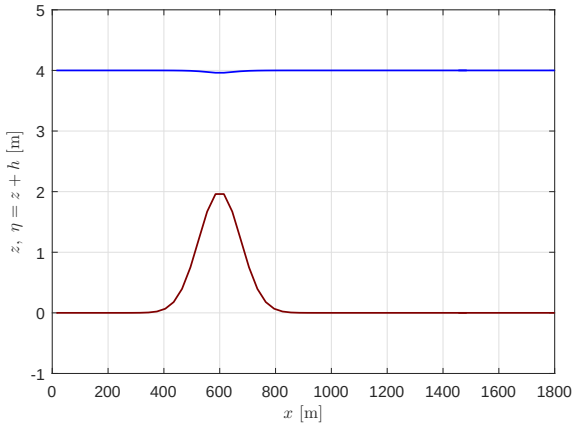

Figure 4.8: Long term evolution of a bottom hump: initial water surface elevation (blue) and bed elevation (red) profiles.

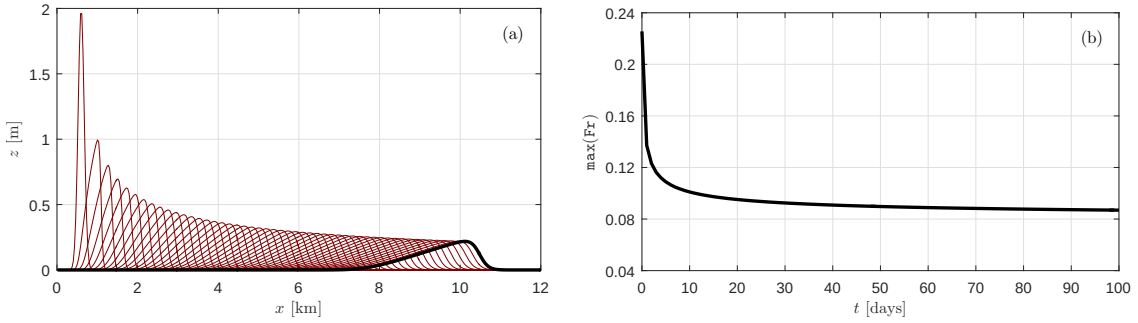

Figure 4.9: Reference solution for the long term evolution of a bottom hump: a) bottom profiles every two days, in thick line day number 100; b) time evolution of the maximum `Fr` measured within the numerical domain.

bed information, $\lambda_3 \equiv \lambda_3^{\texttt{MF}} \equiv \lambda_3^{\texttt{MS}}$, overlap each other (Fig. 4.7a). As a consequence the celerity of the infinitesimal bed form is well predicted by both the MORFAC and MASSPEED approaches (see also Fig. 4.5 in §4.3.3). It is also seen that the amplitude of water depth (Fig. 4.7b) and bed elevation (Fig. 4.7c) are also accurately predicted. A marked difference is found for the water discharge (Fig. 4.7c) for which the MORFAC approach introduces a larger deviation to that of MASSPEED.

4.5.2 Long term evolution of a bottom hump: frictionless case

This test case consists of the simulation of the long term evolution of an erodible bottom hump immersed into a quasi-steady, frictionless flow; it is similar to the test proposed by Ranasinghe *et al.* [51]. The initial bed profile is given by

$$z(x,0) = z_{\max}\ \exp\left[-\frac{(x-\mu)^2}{\sigma^2}\right], \tag{4.56}$$

where $z_{\max} = 2$ m, $\mu = 600$ m and $\sigma = 150$ m. The initial uniform water discharge is $q(x,0) = q_0 = 2$ m^3/(s m) while the initial water depth corresponds to the steady state water profile for the given discharge and initial bed topography, see Fig. 4.8. A constant discharge q_0 is imposed at the upstream boundary while a constant water depth $h_0 = 4$ m is imposed at the downstream boundary. Transmissive downstream boundary conditions are imposed for the bed and A_g is set to 0.005 s^2/m in the Grass sediment transport formula (2.5). The numerical domain ($x \in [0; 12000]$ m) is discretized with 400 cells of constant width (30 m). Finally, the morphodynamic output time is set equal to 100 days.

Fig. 4.9a shows the bottom evolution in time, with a temporal breakdown of 2 days, obtained with the original, non-accelerated model. In the first simulated days, the amplitude of the hump decreases rapidly and after about 20 days the bottom assumes a flatter and stable profile. The decrease of the hump amplitude is associated to a corresponding decrease of the maximum Froude number on the computational domain (Fig. 4.9b).

For this test, 10 different runs are summarized in Tab. 4.1. The approach used is specified in column 2, while the acceleration factors and the tolerance used to compute them is specified in column 3. Runs 1 to 3 implement the MORFAC approach ($\mathtt{M}_{\mathrm{cw}} = \mathtt{M}_{\mathrm{q}} = 1$, and $\mathtt{M}_{\mathrm{cs}} = \mathtt{MF}$), with tolerance `Tol` equal to 5%, 1% and 0.1% respectively. Runs 4 to 6 implement the MASSPEED approach ($\mathtt{M}_{\mathrm{q}} = 1$, and $\mathtt{M}_{\mathrm{cw}} = \mathtt{M}_{\mathrm{cs}} = \mathtt{MS}$), with the same tolerances as the previous set. The constant factors `MF` and `MS` are computed by using (4.51) and (4.52), respectively and considering the highest Froude number of the simulation. In this test the maximum Froude number corresponds to the initial maximum value $\mathtt{Fr} \approx 0.23$, as shown in Fig. 4.9b. Finally, runs 7 to 10 implement the adaptive version A-MASSPEED, tested with tolerances $\mathtt{Tol} = 5; 1; 0.1; 0.01$ [%].

The accuracy of the accelerated solutions with respect to the reference solution is evaluated qualitatively in terms of the final position of the hump crest and, quantitatively, via the normalized root square error $\mathtt{E}_{\mathtt{z}}$, defined as

$$\mathtt{E}_{\mathtt{z}} = \frac{\sqrt{\sum \left(z - z_{\mathtt{ref}}\right)^2}}{\sqrt{\sum z_{\mathtt{ref}}^2}}\,, \tag{4.57}$$

where z and $z_{\mathtt{ref}}$ are the bottom profiles at the end of the simulation for the given accelerated model (MORFAC or MASSPEED) and the original system. The computational costs and accuracy of the 10 runs are also specified in Tab. 4.1, while some examples of final bottom profiles are depicted in Fig. 4.11.

As a first robustness assessment, it is worth noting that the accuracy ($\mathtt{E}_{\mathtt{z}}$ and crest position) increases when reducing the tolerance `Tol` for all the acceleration strategies. Table 4.1 highlights also the significant differences of computational speed-up between the tested approaches: i.e. MORFAC and A-MASSPEED have speed-up differences of roughly one order or magnitude. Moreover, it is important

Table 4.1: Long term evolution of the bottom hump: acceleration parameters (MF, MS and Tol), number of computational time steps, CPU time, numerical (4.20) and theoretical (4.18) speed-up, normalized error E_z and final position of the hump crest.

#	Method	Acc. Factors	Time steps	CPU [s]	Sp^{CPU}	Sp	E_z	x(crest) [m]
0	Ref. Sol.		2 050 300	6803	-	-	-	10125
1	MORFAC	$MF_{5.0\%} = 7.1$	291 600	926	7.3	7.1	1.53e-1	10005
2		$MF_{1.0\%} = 2.2$	940 400	3014	2.3	2.2	2.98e-2	10095
3		$MF_{0.1\%} = 1.1$	1 848 700	6013	1.1	1.1	2.81e-3	10125
4	MASSPEED	$MS_{5.0\%} = 13\,049$	16 801	57	119	103	1.19e-2	10125
5		$MS_{1.0\%} = 2\,985$	34 802	114	60	50	4.17e-3	10125
6		$MS_{0.1\%} = 304$	109 101	353	19	16	1.06e-3	10125
7	A-MASSPEED	$MS_{5.0\%}$	2 236	9	782	836	3.81e-1	10485
8		$MS_{1.0\%}$	4 700	16	413	404	9.36e-2	10215
9		$MS_{0.1\%}$	14 234	48	141	132	1.19e-2	10125
10		$MS_{0.01\%}$	44 443	150	45	42	1.61e-3	10125

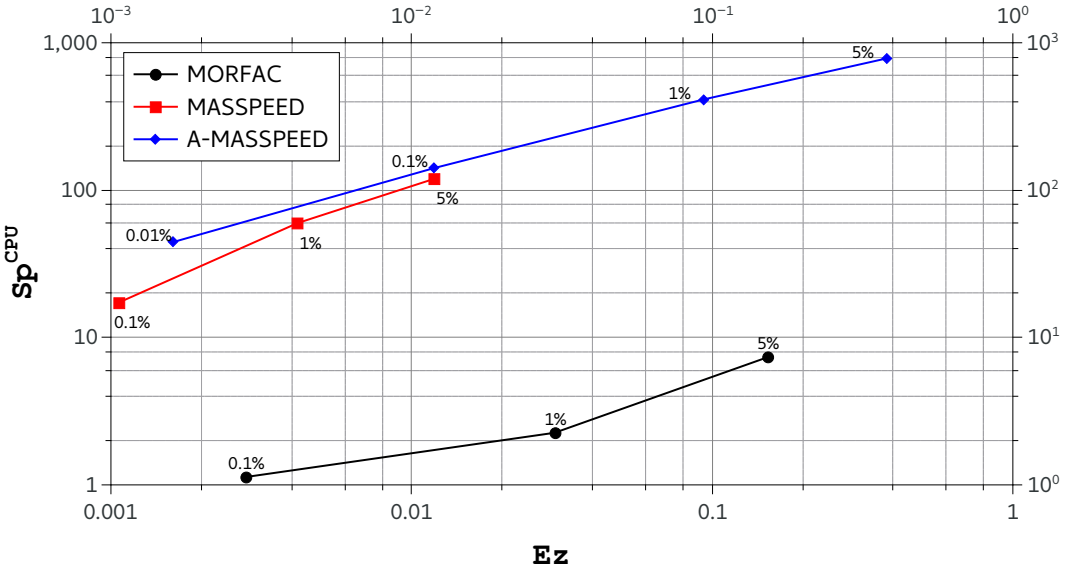

Figure 4.10: Numerical speed-up $\mathtt{Sp}^{\mathtt{CPU}}$ against normalized errors $\mathtt{E_z}$ for the 10 accelerated runs. Marker labels highlight the user-defined tolerances resumed in Table 4.1.

to underline that the theoretical speed-up `Sp` is always fairly close to the measured $\mathtt{Sp}^{\mathtt{CPU}}$ (see §4.2.5). Hence the theoretical formulation can be adopted as a good *a priori* estimation of the effective simulation speed-up.

To better focus on the differences between the investigated strategies, in Fig. 4.10 the numerical speed-up $\mathtt{Sp}^{\mathtt{CPU}}$ of the 10 accelerated runs are plotted against the normalized errors $\mathtt{E_z}$. It is worth noting that the plot is in log-log scale. Beside the evident increase of the computational speed-up offered by the new proposed approaches with respect to MORFAC, Fig. 4.10 sheds the light on the accuracy differences of the three methods for a given `Tol`. In particular, it appears that for the same given `Tol`, i) MASSPEED is more accurate than MORFAC and ii) the adaptive A-MASSPEED is less accurate than both fixed methods. To justify issue i), please note that for the MORFAC and MASSPEED methods, the acceleration factors `MF` and `MS` are fixed (values in Tab. 4.1) for the entire run based on the maximum expected Froude number and the given tolerance. If the Froude number decreases during the simulation, as in the given test, the error on the linearity assumption (4.51) also decreses, being a function of `Fr` (Fig. 4.6a and b). Nevertheless, the error reduction is faster for the MASSPEED approach, i.e. the ratio of the bottom eigenvalue (red solid line) in Fig. 4.6b tends to the constant factor `MS` faster than the corresponding ratio in Fig. 4.6a. Given this difference in the error reduction rate, the accumulated final error of the MASSPEED method is reduced with respect to MORFAC.

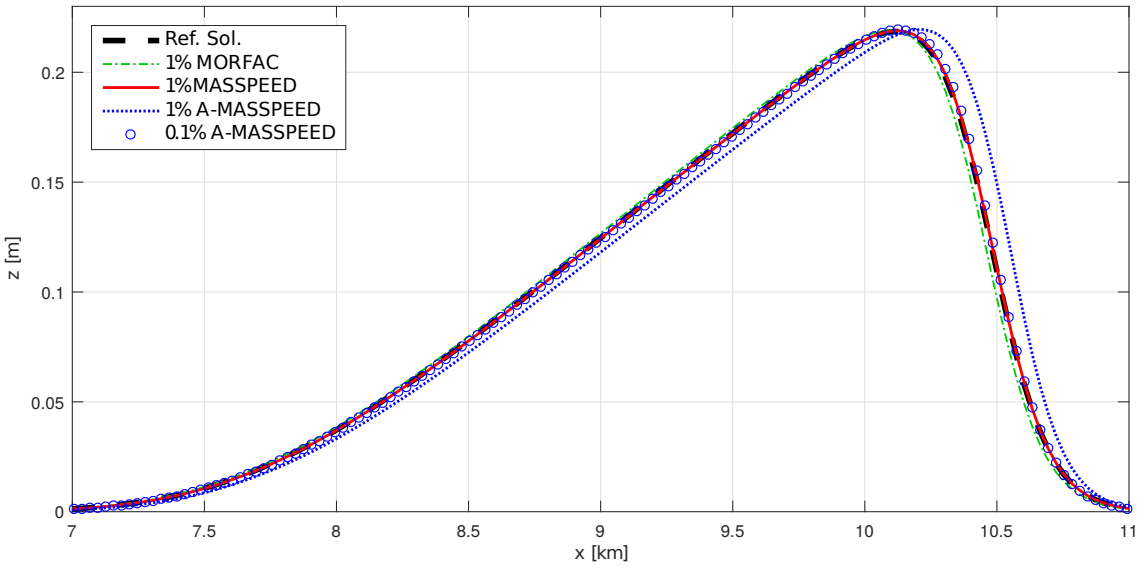

Figure 4.11: Bottom hump profiles after a 100 days evolution: comparison between reference solution (thick black), MORFAC (run 2), MASSPEED (run 5) and A-MASSPEED (runs 8,9) models.

Issue ii) well underlines the main difference between the *fixed* approach (MORFAC and MASSPEED) and the *adaptive* one (A-MASSPEED). This accuracy gap is evident also in Fig. 4.11, where final bottom profiles are plotted for some selected runs. For given $\texttt{Tol} = 1\%$, MORFAC and MASSPEED profiles are very close to the reference solution, while the A-MASSPEED solution shows an offset of the crest position. As previously discussed, the effective error on the linearity Eq. (4.51) decreases during the simulation time when using the *fixed* approaches. On the other hand, with A-MASSPEED, the *adaptive* acceleration factor $\texttt{MS}$ is not bonded by $\texttt{Fr}^{\max}$, but instead recomputed at each time step. This means that the error on the linearity assumption (4.51) is dynamically forced to be constant and equal to the user-defined $\texttt{Tol}$. Such different behavior of the error, decreasing with the fixed strategy but constant with the adaptive one, results in the final greater error of the latter.

Even if, for a given user-defined $\texttt{Tol}$, the *adaptive* strategy is less accurate, it is important to highlight that it globally outperforms both the *fixed* methods: as a matter of fact, for any accuracy (error $\texttt{E}_\texttt{z}$), A-MASSPEED provides the highest numerical speed-up (Fig. 4.10). Moreover, this method has a further benefit related to the robustness. In fact with the *fixed* approach, the maximum Froude number occurring during the simulation must be known *a priori*. For very simple applications, as in the test presented here, this prediction is straightforward but in case of more complex hydro-morphological configurations this might not be possible. A "wrong" initial setting of the constant acceleration factors may lead to a final numerical solution

that did not satisfy the linearity conditions, hence to a non-linear acceleration of the morphological evolution. In the worst case, a wrong constant factor leads to the loss of hyperbolicity of the accelerated system, hence to a completely failing numerical solution. On the contrary, such troubles are inherently handled by the *adaptive* strategy, where the acceleration factors are dynamically recomputed to keep the acceleration within the linearity threshold.

4.5.3 Long term evolution of a bottom hump: bottom friction case

The main goal of this last test is to verify that the friction term does not alter the main features of the accelerated models. To account also for the bottom friction term into the accelerated framework, system (4.1) can be rewritten as

$$\frac{\partial \boldsymbol{W}}{\partial t} + \boldsymbol{\mathcal{M}}\,\boldsymbol{\mathcal{A}}(\boldsymbol{W})\frac{\partial \boldsymbol{W}}{\partial x} = \boldsymbol{\mathcal{M}}\boldsymbol{S}(\boldsymbol{W}), \tag{4.58}$$

where $\boldsymbol{S}(\boldsymbol{W})$ is the vector of the source terms defined in (2.3) and $\boldsymbol{\mathcal{M}}$ is the acceleration matrix. It is important to note that $\boldsymbol{\mathcal{M}}\boldsymbol{S}(\boldsymbol{W}) = [0, -\mathtt{M_q}\, c^2 s_f, 0]^{\mathrm{T}}$ and $\mathtt{M_q} = 1$ in both MORFAC and MASSPEED approaches. Therefore, the accelerations of the models do not influence the expression of the friction source term.

From a numerical point of view, in the implemented numerical model the source term is treated by using a very simple procedure (see. §3.2). Without loss of generality, only the results for the adaptive A-MASSPEED approach are presented, assuming $\mathtt{Tol} = 0.001$.

The test is a modification of that given in the previous section (same boundary conditions), where a constant slope $s_0 = 0.1‰$ is added to the initial bed profile, thus,

$$z(x,0) = -s_0 x + z_{\max}\,\exp\left[-\frac{(x-\mu)^2}{\sigma^2}\right]. \tag{4.59}$$

Assuming a water discharge $q_0 = 2$ m^3/(s m) and constant Strickler roughness $K_s = 19.8$ m$^{1/3}$s^{-1}, the resulting normal flow depth is $h_0 = 4$ m. Fig. 4.12a shows the initial water surface and bottom elevation profiles. The simulated time is 50 days.

Fig. 4.12b shows the comparison between the bottom profile at the end of the simulation, obtained using the A-MASSPEED approach, and the corresponding reference solution. It is seen that the solutions are in good agreement. Moreover, the error $\mathtt{E_z}$ computed by using relation (4.57), is equal to 1.3e-2, i.e., of the same order of magnitude of the errors obtained by neglecting the friction term (see Tab. 4.1). Analogous results, here omitted for the sake of brevity, can be obtained by using the MORFAC approach.

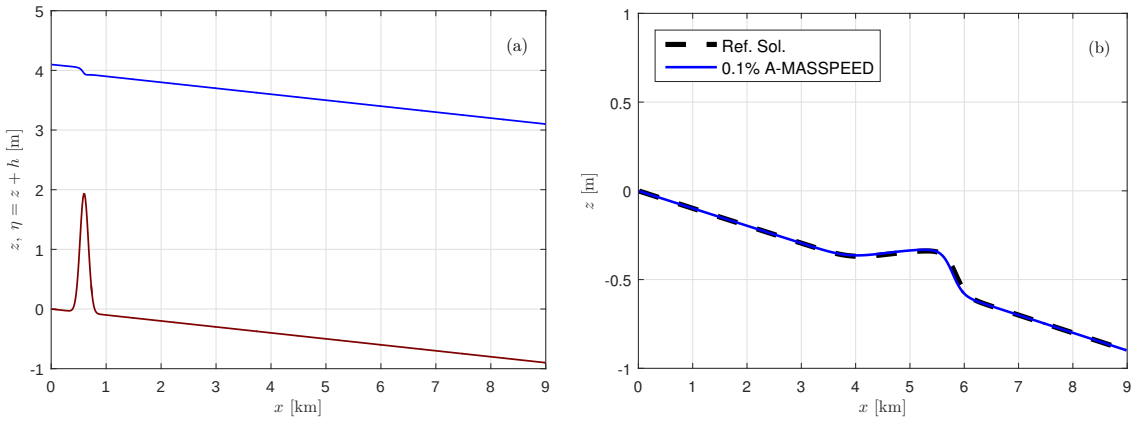

Figure 4.12: Treatment of the friction source term: (a) initial condition of the Hump test with not negligible friction; (b) results of a 50 days long morphodynamic simulation of the hump evolution.

4.6 Considerations

In this chapter a general mathematical framework is developed to study the conditions under which bed evolution, governed by the one-dimensional dSVE equations, can be linearly accelerated. This is achieved by introducing the concept of non-uniform acceleration, by multiplying the spatial derivatives of each of the three governing equations by an individual acceleration factor. In this environment, the classical MORFAC acceleration results from the acceleration of the mere sediment continuity equation. Furthermore, a new linear morphodynamic acceleration technique, MASSPEED, is obtained by equally accelerating both mass continuity equations for water and sediment.

Assuming valid the hypothesis of weak coupling between hydrodynamics and morphodynamics, from the analytical study of the linearized new mathematical framework results that the linear acceleration of the third eigenvalue (which is the one relate to the morphodynamic evolution) is a necessary condition for an appropriate morphodynamic acceleration.

Building on the knowledge obtained from the linear analysis, a practical and implementable criterion for the determination of the maximum acceleration factor for both techniques is derived. The accuracy of the numerical solution can be determined by the user through the choice of a small tolerance value. This quantifies the extension of the range of validity under which the bed level can be linearly accelerated. The new criterion is implemented following an adaptive concept and tested within the numerical model discussed in Chapter 3. Thanks to the adaptive procedure, the maximum accelerating factor is chosen at each time step according to the actual flow and sediment transport conditions. The numerical solution of the long term evolution of a sediment hump demonstrates that the application of the

MASSPEED approach results in larger speed-up and considerable reduction of the computational time.

It is also worth remarking the most important limitations of the proposed approach, strictly related to the hypothesis of decoupled morphodynamic evolution. In particular, the drawbacks relate to the decoupling looks enforced by the acceleration of bed evolution. The greater the acceleration is, the more the morphodynamic is decoupled from the hydrodynamic. The results presented in this research are based on a few, strategic model simulations of the simple case of the one-dimensional propagation of a sediment hump under almost constant flow conditions. Therefore, acceleration techniques must be cautiously used when non-uniform morphology and time varying forcing (which may include tides, flood waves, etc.) comes to modelling. It is likely that, in these cases, the maximum acceleration factor must be considerably decreased (for both MORFAC and MASSPEED approaches). The higher the `Fr` is, the smaller will be the acceleration; furthermore, it is likely that the more unsteady the flow is, the smaller will be the possible acceleration. Any further study to extend the application of these acceleration techniques must consider the effects that any kind of acceleration have on unsteady hydrodynamic conditions.

Bearing in mind these limitations, the theoretical background presented in this research provides a robust basis for further exploring new morphological accelerators and extending the limit of applicability of the MASSPEED approach. Moreover, following a similar approach, the MASSPEED application can be extended to future trends, including: unsteady flow conditions, 2D (planar) morphological models, suspended transport and the de Saint Venant-Exner-Hirano model for non-uniform sediment deposition.

Chapter 5

Conclusion

In this doctoral dissertation the one-dimensional de Saint Venant-Exner mathematical model is introduced to study how to improve the numerical efficiency of morphological models. Through the analytical study of the dSVE flux matrix eigenstructure, the interactions between hydrodynamic and morphodynamic equations are investigated by the solution of a linearized prototype problem. This simplified analysis shows quantitatively that the lower the Froude number and the intensity of the sediment transport are, the weaker is the interaction between water flow and bed response and the more the bed evolution is described by a decoupled nonlinear wave equation. Furthermore, according to the linearized approach, this decoupled wave equation corresponds to the wave propagation of the characteristic variable associated to the slower eigenvalue of the dSVE flux matrix, here defined as third eigenvalue (λ_3) and third characteristic variable (ζ_3). For growing `Fr` (and, in general, the hydrodynamic unsteadiness), the transition from this case of weak interaction to that of full coupling between equations is usually smooth, while its smoothness depends on the sediment properties and then to the intensity of the solid transport. However, the strict relation between ζ_3 and the bed evolution highlights the importance of a proper representation of the central wave of the Riemann problem associated to the dSVE system, also when a fully coupled numerical scheme is adopted.

A corroboration of this important feature of the morphodynamic evolution come from the implementation of the A-DOT scheme: an analytical implementation of the Dumbser-Osher-Toro Riemann solver for the dSVE model. In particular, the analytical eigenstructure of the dSVE system, formulated in Chapter 2, is used to compute the jump functions at cell edges to improve the numerical performance of the DOT path-conservative scheme. The resulting upwind numerical scheme is based on a complete Riemann solver, in which an individual (and generally different) numerical viscosity is attributed to each characteristic field, and particularly to the intermediate fields related to the third characteristic variable ζ_3.

In Chapter 3 a study of the numerical efficiency and a strong validation of the A-DOT scheme is presented, using as references original DOT and PRICE-C schemes and two different experimental data sets. With the computational grid resolution fixed, the A-DOT scheme computes the solution ten times faster than DOT, keeping unchanged the accuracy of the solution itself. This efficiency boost does not depend on a specific test or particular morphodynamic conditions. Similarly, with a target accuracy fixed, the A-DOT scheme presents a better performance than the efficient PRICE-C scheme.

The performance of the A-DOT scheme is also achieved by simplifying the implementation of the DOT method. While the original DOT scheme requires the use of numerical libraries, the A-DOT jump function is merely computed as the product of three known matrices. Thus, the A-DOT scheme is both easy to implement and very portable within different coding environments and languages. Finally, the A-DOT method do not make use of any kind of tuning coefficient and not specific limitations are imposed in term of sediment transport formulae.

The strong relation between ζ_3 and the morphodynamic evolution allows also other strategies to increase the numerical efficiency of morphodynamic models. In Chapter 4 a theoretical analysis introduces a new mathematical framework to study morphological upscaling techniques. This is achieved by multiplying the spatial derivatives of each of the three governing equations by an individual acceleration factor. In this non-uniformly accelerated environment, the classical MORFAC technique results from the acceleration of the mere sediment continuity equation, while a new linear morphodynamic acceleration technique, MASSPEED, is obtained by equally accelerating both mass continuity equations for water and sediment.

From the study of characteristic variables components results that an appropriate morphodynamic acceleration is possible if and only if: i) the hypothesis of weak coupling between hydrodynamic and morphodynamic is valid; ii) the third eigenvalue is *linearly accelerated* (i.e. the accelerated model must have λ_3 exactly proportional to the acceleration coefficient times the original third eigenvalue).

Building on this latter condition, a practical and implementable criterion for the determination of the maximum acceleration factor for both MORFAC and MASSPEED is derived. The accuracy of the numerical solution can be determined by the user through the choice of a small tolerance value, which defines the extension of the range of acceleration's linearity. This criterion is implemented and tested within the ADOT numerical model for MORFAC, MASSPEED and following an adaptive concept A-MASSPEED. Thanks to the adaptive procedure, the maximum accelerating factor is chosen at each time step according to the actual flow and sediment transport conditions. The solution of the long term evolution of a sediment hump demonstrates that, compared to the MORFAC, the application of the MASSPEED approach results in larger speed-up and considerable reduction of the computational time.

The developed mathematical background for general morphological acceleration techniques could be seen also as a step forward to mathematically define the limitation of these approaches. In particular, the drawbacks relate to the decoupling looks enforced by the acceleration of bed evolution. The greater the acceleration is, the more the morphodynamic is decoupled from the hydrodynamic. Moreover, the introduction of two different time scales for hydrodynamic and morphodynamic gives rise to distortions of unsteady hydrodynamic waves. Any further study to extend the application of these acceleration techniques must consider this effects that any kind of acceleration have on unsteady hydrodynamic conditions. E.g., if the user is mainly interested in the morphological evolution, an equivalent hydrodynamic wave may have to be recomputed for the morphological time scale (properly using the accelerated characteristic variables). Then the long term bed evolution can be predict, while the correspondent hydrodynamic evolution should be afterwards reconstructed, if needed. However, the theoretical background presented in this research provides a robust basis for further exploration, including: unsteady flow conditions, 2D (planar) morphological models, suspended transport and the de Saint Venant-Exner-Hirano model for non-uniform sediment deposition.

Bibliography

1. Abgrall, R. & Karni, S. A comment on the computation of non-conservative products. *Journal of Computational Physics* **229,** 2759–2763 (2010).
2. Armanini, A. & Di Silvio, G. A one-dimensional model for the transport of a sediment mixture in non-equilibrium conditions. *Journal of Hydraulic Research* **26,** 275–292 (1988).
3. Bellal, M., Spinewine, B., Savary, C. & Zech, Y. *Morphological Evolution of Steep-Sloped River Beds in the Presence of a Hydraulic Jump: Experimental Study* in *XXX IAHR Congress* (2003), 133–140.
4. Berthon, C., Cordier, S., Delestre, O. & Le, M. H. An analytical solution of the shallow water system coupled to the Exner equation. *Comptes Rendus Mathematique* **350,** 183–186 (2012).
5. Brunner, G. W. *HEC-RAS River Analysis System - Hydraulic Reference Manual, Version 5.0* 547 (US ARMY CORPS OF ENGINEERS HYDROLOGIC ENGINEERING CENTER (HEC), 2016).
6. Caleffi, V., Valiani, A. & Bernini, A. High-order balanced CWENO scheme for movable bed shallow water equations. *Advances in Water Resources* **30,** 730–741 (2007).
7. Caleffi, V. & Valiani, A. Well balancing of the SWE schemes for moving-water steady flows. *Journal of Computational Physics* **342,** 85–116 (Aug. 2017).
8. Caleffi, V., Valiani, A. & Li, G. A comparison between bottom-discontinuity numerical treatments in the DG framework. *Applied Mathematical Modelling* **40,** 7516–7531 (Sept. 2016).
9. Canestrelli, A., Siviglia, A., Dumbser, M. & Toro, E. F. Well-balanced high-order centred schemes for non-conservative hyperbolic systems. Applications to shallow water equations with fixed and mobile bed. *Advances in Water Resources* **32,** 834–844 (2009).
10. Canestrelli, A. & Toro, E. F. Restoration of the contact surface in FORCE-type centred schemes II: Non-conservative one- and two-layer two-dimensional shallow water equations. *Advances in Water Resources* **47,** 76–87 (2012).

11. Cardano, G. *Artis magnae sive de regulis algebraicis liber unus* (Petreius, Nürnberg, Germany, 1545).

12. Carraro, F., Caleffi, V. & Valiani, A. *Comparison between different methods to compute the numerical fluctuations in path-conservative schemes for SWE-Exner model* in *Sustainable Hydraulics in the Era of Global Change: Proceedings of the 4th IAHR Europe Congress* (eds Erpicum, S., Dewals, B., Archambeau, P. & Pirotton, M.) (Taylor & Francis Group, Liege Belgium, 2016), 699–706.

13. Carraro, F., Valiani, A. & Caleffi, V. Efficient analytical implementation of the DOT Riemann solver for the de Saint Venant-Exner morphodynamic model. *Advances in Water Resources* (Jan. 2018).

14. Carraro, F., Vanzo, D., Caleffi, V., Valiani, A. & Siviglia, A. Mathematical study of linear morphodynamic acceleration and derivation of the MASSPEED approach. *submitted* (2017).

15. Castro, M. J., Pardo Milanes, A. & Parés, C. Well-Balanced numerical schemes based on a generalized hydrostatic reconstruction technique. *Mathematical Models and Methods in Applied Sciences* **17,** 2055–2113 (2007).

16. Castro, M., Gallardo, J. M. & Parés, C. High order finite volume schemes based on reconstruction of states for solving hyperbolic system with nonconservative products. Application to shallow-water systems. *Mathematics of Computation* **75,** 1103–1134 (2006).

17. Coco, G., Zhou, Z., van Maanen, B., Olabarrieta, M., Tinoco, R. & Townend, I. Morphodynamics of tidal networks: Advances and challenges. *Marine Geology* **346,** 1–16 (2013).

18. Cordier, S., Le, M. H. & Morales de Luna, T. Bedload transport in shallow water models: Why splitting (may) fail, how hyperbolicity (can) help. *Advances in Water Resources* **34,** 980–989 (2011).

19. Dal Maso, G., LeFloch, P. G. & Murat, F. Definition and weak stability of nonconservative products. *Journal de mathématiques pures et appliquées* **74,** 483–548 (1995).

20. De Vriend, H., Capobianco, M., Chesher, T., De Swart, H. d., Latteux, B. & Stive, M. Approaches to long-term modelling of coastal morphology: a review. *Coastal Engineering* **21,** 225–269 (1993).

21. (ed De Vries, M.) *Considerations about non-steady bed-load transport in open channels Int. Assn. Hydraulic Research* 3.8.1-3.8.8. Leningrad (1965).

22. Defina, A. Numerical experiments on bar growth. *Water Resources Research* **39,** 1–12 (2003).

23. Dumbser, M., Castro, M., Parés, C. & Toro, E. F. ADER schemes on unstructured meshes for nonconservative hyperbolic systems: Applications to geophysical flows. *Computers and Fluids* **38,** 1731–1748 (2009).

24. Dumbser, M., Enaux, C. & Toro, E. F. Finite volume schemes of very high order of accuracy for stiff hyperbolic balance laws. *Journal of Computational Physics* **227,** 3971–4001 (2008).

25. Dumbser, M. & Toro, E. F. A Simple Extension of the Osher Riemann Solver to Non-conservative Hyperbolic Systems. *Journal of Scientific Computing* **48,** 70–88 (2011).

26. Duró, G., Crosato, A. & Tassi, P. Numerical study on river bar response to spatial variations of channel width. *Advances in Water Resources* **93,** 21–38 (2016).

27. Exner, F. M. *Über die Wechselwirkung zwischen Wasser und Geschiebe in Flüssen* (Akademie der Wissenschaften, Sitzungsberichte 134, Wien, Austria, 1925).

28. Fjordholm, U. S., Mishra, S. & Tadmor, E. Well-balanced and energy stable schemes for the shallow water equations with discontinuous topography. *Journal of Computational Physics* **230,** 5587–5609 (June 2011).

29. Grass, A. J. *Sediment transport by waves and currents* (University College, London, Dept. of Civil Engineering, 1981).

30. Isaacson, E. & Temple, B. Nonlinear resonance in systems of conservation laws. *SIAM Journal on Applied Mathematics* **52,** 1260–1278 (1992).

31. Kelly, D. & Dodd, N. Beach-face evolution in the swash zone. *Journal of Fluid Mechanics* **661,** 316–340 (2010).

32. Lanzoni, S., Siviglia, A. & Seminara, G. Long waves in erodible channels and morphodynamic influence. *Water Resources Research* **42** (2006).

33. Latteux, B. Techniques for long-term morphological simulation under tidal action. *Marine Geology* **126,** 129–141 (1995).

34. Lesser, G. R., Roelvink, J. A., van Kester, J. A. T. M. & Stelling, G. S. Development and validation of a three-dimensional morphological model. *Coastal Engineering* **51,** 883–915 (2004).

35. Li, L. *A fundamental study of the Morphological Acceleration Factor* PhD thesis (Delft University of Technology, 2010).

36. Li, Z.-J., Cao, Z.-X., Pender, G. & Hu, P. Numerical analysis of adaptation-to-capacity length for fluvial sediment transport. *Journal of Mountain Science* **11,** 1491–1498 (2014).

37. Liu, T.-P. Nonlinear resonance for quasilinear hyperbolic equation. *Journal of mathematical physics* **28,** 2593–2602 (1987).

38. Lyn, D. Unsteady sediment transport modeling. *Journal of Hydraulic Engineering* **113,** 1–15 (1987).

39. Lyn, D. a. & Altinakar, M. St. Venant–Exner Equations for Near-Critical and Transcritical Flows. *Journal of Hydraulic Engineering* **128,** 579–587 (2002).

40. Martini, P., Carniello, L. & Avanzi, C. Two dimensional modelling of flood flows and suspended sedimenttransport: the case of the Brenta River, Veneto (Italy). *Natural Hazards and Earth System Science* **4,** 165–181 (2004).

41. Meyer-Peter, E. & Müller, R. Formulas for Bed-Load Transport. *Proceedings of the 2nd Meeting of the International Association of Hydraulic Research,* 39–64 (1948).

42. Mosselman, E. & Le, T. B. Five common mistakes in fluvial morphodynamic modeling. *Advances in Water Resources* **93,** 15–20 (2016).

43. Müller, L. O. & Toro, E. F. A global multiscale mathematical model for the human circulation with emphasis on the venous system. *International Journal for Numerical Methods in Biomedical Engineering* **30,** 681–725 (July 2014).

44. Murillo, J. & García-Navarro, P. An Exner-based coupled model for two-dimensional transient flow over erodible bed. *Journal of Computational Physics* **229,** 8704–8732 (2010).

45. Murillo, J. & García-Navarro, P. Energy balance numerical schemes for shallow water equations with discontinuous topography. *Journal of Computational Physics* **236,** 119–142 (2013).

46. Nicholas, A. P. Modelling the continuum of river channel patterns. *Earth Surface Processes and Landforms* **38,** 1187–1196 (2013).

47. Oorschot, M. v., Kleinhans, M., Geerling, G. & Middelkoop, H. Distinct patterns of interaction between vegetation and morphodynamics. *Earth Surface Processes and Landforms* (2015).

48. Parés, C. Numerical methods for nonconservative hyperbolic systems: a teoretical framework. *SIAM Journal on Numerical Analysis* **44,** 300–321 (2006).

49. Postacchini, M., Othman, I., Brocchini, M. & Baldock, T. Sediment transport and morphodynamics generated by a dam-break swash uprush: Coupled vs uncoupled modeling. *Coastal Engineering* **89,** 99–105 (2014).

50. Pu, J., Hussain, K., Shao, S.-D. & Huang, Y.-F. Shallow sediment transport flow computation using time-varying sediment adaptation length. *International Journal of Sediment Research* **29,** 171–183 (2014).

51. Ranasinghe, R., Swinkels, C., Luijendijk, A., Roelvink, D., Bosboom, J., Stive, M. & Walstra, D. Morphodynamic upscaling with the MORFAC approach: Dependencies and sensitivities. *Coastal Engineering* **58,** 806–811 (2011).

52. Roelvink, J. Coastal morphodynamic evolution techniques. *Coastal Engineering* **53,** 277–287 (2006).

53. Roelvink, J. D., Walstra, D.-J. R., van der Wegen, M. & Ranasinghe, R. *Modeling of Coastal Morphological Processes* in *Springer Handbook of Ocean Engineering* (eds Dhanak, M. R. & Xiros, N. I.) (Springer International Publishing, Cham, 2016), 611–634.

54. Shekari, Y. & Hajidavalloo, E. Application of Osher and PRICE-C schemes to solve compressible isothermal two-fluid models of two-phase flow. *Computers & Fluids* **86,** 363–379 (2013).

55. Siviglia, A. & Crosato, A. Numerical modelling of river morphodynamics: Latest developments and remaining challenges. *Advances in Water Resources* **93,** 1–3 (2016).

56. Siviglia, A., Stecca, G., Vanzo, D., Zolezzi, G., Toro, E. F. & Tubino, M. Numerical modelling of two-dimensional morphodynamics with applications to river bars and bifurcations. *Advances in Water Resources* **52,** 243–260 (2013).

57. Soni, J., Garde, R. & Raju, K. Aggradation in streams due to overloading. *Journal of the Hydraulics Division, ASCE* **106,** 117–132 (1980).

58. Stecca, G., Siviglia, A. & Blom, A. An accurate numerical solution to the Saint-Venant-Hirano model for mixed-sediment morphodynamics in rivers. *Advances in Water Resources* **93,** 39–61 (2016).

59. Toro, E. F., Millington, R. C. & Nejad, L. A. M. in *Godunov Methods* (ed Toro, E. F.) 907–940 (Springer US, Boston, MA, 2001).

60. Toro, E. F. & Siviglia, A. PRICE: Primitive centred schemes for hyperbolic systems. *International Journal for Numerical Methods in Fluids* **42,** 1263–1291 (2003).

61. Toro, E. *Riemann Solvers and Numerical Methods for Fluid Dynamics* Third, 738 (Springer US, 2009).

62. Traub, J. *Iterative Methods for the Solution of Equations* (Chelsea, 1982).

63. Valiani, A. & Caleffi, V. Momentum balance in the shallow water equations on bottom discontinuities. *Advances in Water Resources* **100,** 1–13 (2017).

64. Valiani, A. & Caleffi, V. Depth-energy and depth-force relationships in open channel flows: Analytical findings. *Advances in Water Resources* **31,** 447–454 (2008).

65. Van Rijn, L. C. Sediment Transport, Part II: Suspended Load Transport. *Journal of Hydraulic Engineering* **110,** 1613–1641 (1984).

66. Vetsch, D., Siviglia, A., Ehrbar, D., Facchini, M., Kammerer, S., Koch, A., Peter, S., Vonwiller, L., Gerber, M., Volz, C., Farshi, D., Mueller, R., Rousselot, P., Veprek, R. & Faeh, R. *System Manuals of BASAMENT, Version 2.7* (Laboratory of Hydraulics, Glaciology and Hydrology (VAW). ETH Zurich., 2017).